Microphysical properties of aerosol particles in the trade wind regime and their influence on the number concentration of activated particles in trade wind cumulus clouds

Von der Fakultät für Physik und Geowissenschaften
der Universität Leipzig
genehmigte

DISSERTATION

zur Erlangung des akademischen Grades
Doctor rerum naturalium
(Dr. rer. nat.)
vorgelegt

von Diplom-Meteorologe Florian Ditas
geboren am 30. Juni 1983 in Beckendorf-Neindorf

Gutachter: Prof. Dr. A. Wiedensohler
Prof. Dr. A. Schwarzenböck

Tag der Verleihung: 21. Juli 2014

Bibliographische Beschreibung

Ditas, Florian

Microphysical properties of aerosol particles in the trade wind regime and their influence on the number concentration of activated particles in trade wind cumulus clouds

Universität Leipzig, Dissertation

130 S.[1], 83 Lit.[2], 40 Abb., 8 Tab., Anlagen

Abstract:
Im Rahmen dieser Dissertation wurden die mikrophysikalischen Eigenschaften von Aerosolpartikeln im Passatklima und deren Einfluss auf Passatwolken untersucht. Die Arbeit basiert auf Messungen mit der hubschrauber-getragenen Messplattform ACTOS. Es wurden zwei Intensivmesskampagnen im November 2010 und April 2011 durchgeführt, welche 31 Forschungsflüge in der Nähe der östlichsten Karibik-Insel Barbados umfassen.
Die gemessenen Partikel-Anzahl-Größenverteilungen weisen meist eine bimodale Verteilung auf, welche typisch für marines Aerosol ist. Im Vergleich zu kontinentalen Verhältnissen ist die Totalanzahlkonzentration der Aerosolpartikel von 100–1000 cm^{-3} gering. Eine statistische Analyse einzelner Wolken lässt auf typische Anzahlkonzentrationen von aktivierten Partikeln bis zu 400 cm^{-3} und minimale Aktivierungsdurchmesser in der Größenordnung von 40 nm bis 180 nm mit entsprechenden maximalen kritischen Übersättigungen zwischen 0.1 und 0.9% schließen. Zusätzlich wurden wesentliche Einflussfaktoren auf die Anzahlkonzentration aktivierter Partikel identifiziert: 1) Vertikalwind an der Wolkenunterkante und 2) Anzahlkonzentration der verfügbaren Aerosolpartikel, die als Wolkenkondensationskeime dienen können.
Mit Hilfe von Beobachtungsdaten und einer umfassenden Sensitivitätsstudie unter Verwendung eines Luftpaketmodells mit spektraler Wolkenmikrophysik wurde die Sensitivität der Wolkentropfenkonzentration gegenüber Änderungen in den physikalischen Eigenschaften und der Hygroskopizität von Aerosolpartikeln untersucht. Die beobachteten Ergebnisse in Form von sogenannten "aerosol-cloud interaction metrics" (ACI, Maß für den Einfluss von Änderungen einer bestimmten Aerosoleigenschaft auf eine bestimmte Wolkeneigenschaft) zeigen eine sehr hohe Sensitivität der Tropfenanzahlkonzentration gegenüber Änderungen in der Partikelanzahlkonzentration (in der Nähe des physikalisch sinnvollen Maximums von eins). Diese abgeleiteten ACI-Metriken eignen sich als Basis für Abschätzungen des indirekten Strahlungsantriebes auf der Grundlage von Beobachtungen.
Zusätzliche Modellrechnungen umfassen die gemessenen Partikeleigenschaften während der gesamten Kampagnen. Die Ergebnisse unterstreichen besonders die Bedeutung der physikalischen Partikeleigenschaften. Die Suszeptibilität der Tropfenanzahlkonzentration gegenüber Änderungen in der Partikelanzahlkonzentration (Wertebereich: 0–1) ist am größten (> 0.9) für den Fall eines stark ausgeprägten Akkumulations-Mode und nimmt ab, je stärker der Aitken-Mode ausgeprägt ist (> 0.6). Im Gegensatz dazu ist die Sensitivität der Tropfenanzahlkonzentration gegenüber Änderungen in der Hygroskopizität der Partikel generell geringer (< 0.4). Die hier präsentierten Ergebnisse stellen eine umfangreiche Charakterisierung der Aerosol- und Wolkeneigenschaften im Passatklima dar und können helfen, die vorhergesagte Sensitivität der Wolkeneigenschaften in Klimamodellen gegenüber Änderungen der Aerosoleigenschaften zu evaluieren und deren Unsicherheiten zu reduzieren.

[1] S. (Seitenzahl insgesamt)
[2] Lit. (Anzahl der im Literaturverzeichnis ausgewiesenen Literaturangaben)

Bibliographic Description

Ditas, Florian

Microphysical properties of aerosol particles in the trade wind regime and their influence on the number concentration of activated particles in trade wind cumulus clouds

University of Leipzig, Dissertation

130 pp.[1], 83 Ref.[2], 40 Fig., 8 Tab., Appendix

Abstract:
Within the scope of this dissertation, microphysical properties of aerosol particles in the trade wind regime and their influence on microphysical properties of trade wind cumulus clouds have been investigated. The study is based on measurements performed with the helicopter-borne measurement platform ACTOS. Two intensive measurement periods were carried out in November 2010 and April 2011, including 31 research flights close to the easternmost Caribbean island — Barbados.
Aerosol particle number size distributions show a bimodal structure, which is typical for marine aerosol particles. The total particle concentrations of approximately 100–1000 cm^{-3} are compared to continental conditions relatively low. A statistical analysis of individual clouds reveals typical number concentrations of activated particles up to 400 cm^{-3} and minimum activation diameters between 40 and 180 nm with corresponding critical supersaturations between 0.1 and 1%. Additionally, major factors affecting the number concentration of activated particles are identified: 1) vertical wind velocity at cloud base and, 2) number concentration of available aerosol particles as potential cloud condensation nuclei.
With the help of observational data and a comprehensive sensitivity study using a spectral cloud microphysical parcel model, the sensitivity of the cloud droplet number concentration towards changes in the microphysical aerosol particle properties and their hygroscopicity has been investigated. Observational results in terms of so-called aerosol-cloud interactions metrics (describes a measure of the influence of changes in one specific aerosol property on one specific cloud property) show a very high sensitivity (close to the physical meaningful maximum of unity) of the number concentration of activated particles towards changes in the particle number concentration. These aerosol-cloud interaction metrics can be used as basis for observationally-based radiative forcing estimates.
Additional model calculations cover the entire range of the observed aerosol properties during both campaigns. The results underline particularly the importance of the physical aerosol properties. The calculated susceptibility (valuation: 0–1) of the droplet number concentration towards changes in the particle number concentration is highest (> 0.9) for accumulation mode dominated particle number size distributions and decreases for Aitken mode dominated size distributions (> 0.6). In contrast, for the modeled parameter space, the sensitivity towards changes in the particle hygroscopicity is generally below 0.4.
The findings presented in this study represent a comprehensive characterization of aerosol and cloud microphysical properties in the trade wind regime. These findings may help to evaluate the predicted sensitivity of cloud microphysical properties by climate models towards changes in particle microphysical properties and reduce the uncertainties in climate sensitivity estimates.

[1] pp. (Number of pages)
[2] Ref. (Number of references)

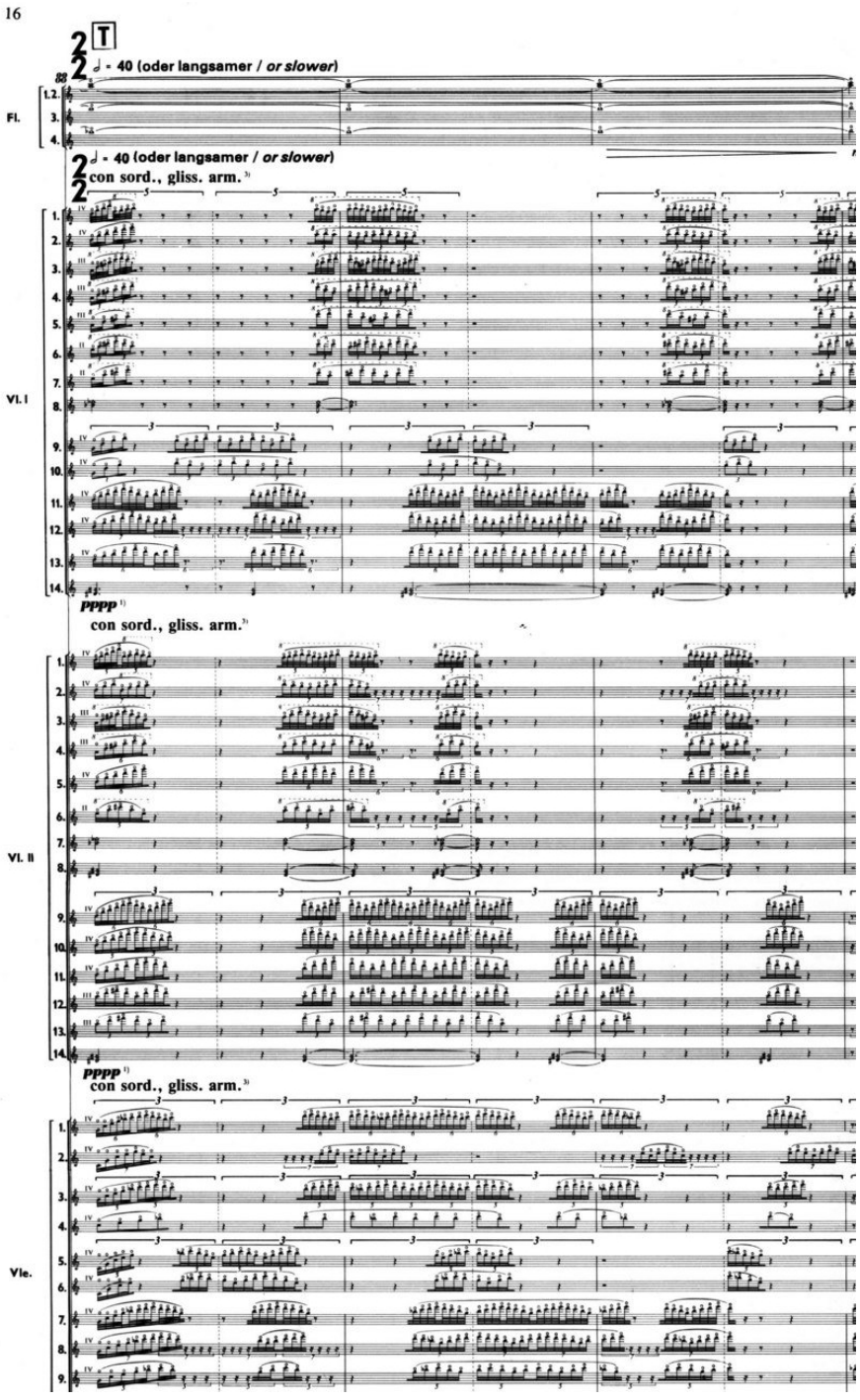

From "Atmospheres" by György Ligeti (May 28, 1923 – June 12, 2006). "Atmospheres" contains plenty of analogies to the Earth's atmosphere in ways which go far beyond rendering extra-musical topics. Ligeti composed 87 individual systems, where no two instruments play the same note. It is hardly possible to follow single instruments. Everything merges into fascinating clusters, noises and sounds which remind the listener to wind, ice or waves. Beyond these hearable analogies, the multitude of individual players faces the diversity of individual but not independent processes in the Earth's atmosphere. Even the form of the score looks like swirling particles or dancing ice crystals.

Table of Contents

Chapter 1

Introduction

The vast diversity of cloud types and their different forms of appearance result mainly from the dynamics and thermodynamics underlying the cloud formation and transformation. Nevertheless, in addition to the dynamic and thermodynamic processes, the microphysical properties of clouds are assumed to be substantially influenced by the atmospheric aerosol.
Aerosol particles are defined as solid and/or liquid particles suspended in air. Atmospheric aerosol particles are generated by disaggregation of solids and dispersion of liquids (primary particle production), gas to particle conversion (secondary particle production) or by direct emission from combustion. Those particles span size ranges from a few nanometers to several tens of micrometers and exhibit concentrations of a few tens to more than one million per cubic centimeter in remote or heavily polluted areas, respectively (e.g., *Seinfeld and Pandis*, 2006, chapter 8).
Atmospheric aerosol particles interact with the ambient humidity. Hydrophilic particles take up water molecules and grow in size with increasing relative humidity (hygroscopic growth). If the ambient relative humidity exceeds a certain threshold above 100%, aerosol particles may get activated to cloud droplets. Those particles, which can potentially form cloud droplets, are called cloud condensation nuclei (CCN). The formation of cloud droplets by condensation of water vapor onto aerosol particles is also called heterogeneous nucleation. Under atmospheric conditions, the necessary supersaturation (critical supersaturation) to activate an aerosol particle is typically less than 2% and depends mainly on the particles' size and chemical composition. A second pathway to form water droplets is the so-called homogeneous nucleation. Thereby, pure water droplets form directly from the condensation of water vapor without any influence of further components (as for instance aerosol particles). For such a case, the environmental air has to be both particle-free and supersaturated with respect to water by several hundred percent. Since aerosol particles are present everywhere in the troposphere, the formation of water droplets by heterogeneous nucleation is the prevailing

cloud droplet formation process. Hence, the formation of any cloud droplet depends on the physical and chemical properties of the aerosol particles, in particular the particle number size distribution, as well as the ambient supersaturation with respect to water vapor (e.g., *Pruppacher and Klett*, 1997; *Seinfeld and Pandis*, 2006).

The so developed clouds are omnipresent all over the atmosphere from the Earth's surface (fog) up to the mesosphere (noctilucent clouds). Clouds play a major role in the Earth's radiation budget. They reflect shortwave radiation back to space and, therefore, influence the planetary albedo. Furthermore, clouds absorb and re-emit long-wave radiation which was emitted by the Earth's surface, thus they contribute to the natural green-house effect (e.g., *Pruppacher and Klett*, 1997).

The hydrological cycle is also strongly influenced by clouds, since they are responsible for the redistribution of liquid water and water vapor. Furthermore, atmospheric gases and particles are scavenged by cloud droplets, so clouds act as micro-reactors for aqueous phase chemistry (e.g., *Seinfeld and Pandis*, 2006), and are important for the wet deposition. Therefore, the microphysical properties of aerosol particles can be influenced by clouds and vice versa.

During the last decades, aerosol-cloud interactions have been brought into focus due to the increasing interest in their role in the anthropogenic climate change (e.g., *Denman et al.*, 2007, and citations in there). Already in the late 1960s, *Warner and Twomey* (1967) recognized that smoke from sugar cane fires increases significantly the number of cloud condensation nuclei. *Twomey* (1977) investigated the influence of pollution particles on the shortwave albedo of clouds. These publications provide first evidence of aerosol particles altering cloud microphysics and epitomize nowadays the so-called Twomey-effect (first indirect aerosol effect). The Twomey-effect denotes the increase of cloud droplet number concentration following an increase in the CCN concentration. For a constant liquid water content, an elevated cloud droplet number concentration leads to smaller droplets. As a consequence, the surface area concentration increases and thus the cloud albedo. Since these first findings, a range of subtle aerosol-cloud interactions have been established, but quantifying remains a challenge (e.g., *Albrecht*, 1989; *Stevens and Feingold*, 2009). In the fourth assessment report of the Intergovernmental Panel on Climate Change (IPCC), aerosol-cloud interactions are identified as the largest source of uncertainty in climate sensitivity estimates (*Solomon et al.*, 2007).

A lot of effort was put into the investigation of the influence of aerosol particles on different cloud types and different locations. Airborne measurements close to Nova Scotia found that polluted conditions are correlated with higher cloud droplet number concentration (*Garrett et al.*, 2002; *Peng*, 2002). Based on quasi-collocated airborne measurements, evidence of the Twomey-effect was also found in marine stratocumulus clouds near the Ca-

nary Islands during the second Aerosol Characterization Experiment (*Brenguier et al.*, 2000; *Snider and Brenguier*, 2000; *Guibert et al.*, 2003). Based on airborne measurements of cumulus clouds near Florida, *VanReken* (2003) predicted the CCN from particle number size distribution measurements and Köhler theory and achieved closure for CCNs at 0.2% supersaturation. For higher supersaturations the modeled CCN concentrations over-predicted the observations. During the same experiment, *Conant* (2004) made a further step forward and obtained closure between predicted and observed cloud droplet number concentration with a bias within the experimental uncertainty of 20%.

In order to quantify the sensitivity of a certain cloud microphysical property (e.g., cloud droplet number concentration, cloud albedo) towards changes in the aerosol particle properties, *Feingold and Remer* (2001) introduced the so-called aerosol-cloud interaction metric (ACI). Airborne investigations of *Painemal and Zuidema* (2013) during the VOCALS-REx study (*Wood et al.*, 2011) proved that stratocumulus clouds in the South-East Pacific are very sensitive towards changes in the particle concentration. Aerosol-cloud interaction metrics can be used as basis for observationally-based radiative forcing estimates (e.g., *McComiskey and Feingold*, 2012). Furthermore, the quantification of the cloud microphysical properties towards changes in the aerosol microphysics at different locations, for different cloud types and for different meteorological regimes may help to evaluate the corresponding predicted sensitivity by climate models and reduce the uncertainties of predicted aerosol-cloud feedbacks.

Stevens and Feingold (2009) pointed out, that aerosol-cloud interactions are most-certainly regime-dependent. They further suggested to intensify research efforts for instance in the trade wind regime. The trade wind regime develops due to large scale subsidence north and south of the Intertropical Convergence Zone (ITCZ) and is characterized by shallow cumulus convection. The prevailing moist convection, embodied by the so-called trade wind cumuli, plays an important role in the transport of moisture, momentum and heat from the well-mixed layer into higher altitudes (*Tiedtke*, 1989). Trade wind cumuli are ubiquitous over large areas over the ocean and are supposed to be very sensitive to variations in the aerosol particle properties (e.g., *Wang and McFarquhar*, 2008). So far, experimental evidence by airborne in-situ ACI metrics is missing. Furthermore, those clouds are in the center of the so-called lifetime hypothesis (e.g., *Stevens and Feingold*, 2009).

A recent experiment in the trade region was the Rain In Cumulus over the Ocean (RICO) campaign (*Rauber et al.*, 2007). Based on measurements during RICO, *Colón-Robles et al.* (2006) emphasize the importance of the low level wind speed. They argue that the formation of large drops and large droplet number concentration are both primarily depending on low level horizontal wind speed. In contrast, *Hudson and Mishra* (2007) show conflicting findings and underlines the importance of the CCN concentration as major factor controlling the cloud

droplet number concentration.
Some of the above mentioned studies are limited by the spatial resolution of the aerosol measurements (e.g., *VanReken*, 2003) or suffer from quasi-collocated measurements on different platforms (e.g., ACE-2). According to *McComiskey and Feingold* (2012), the accurate quantification of aerosol-cloud interactions requires: (1) direct, independent, and collocated measurements and, (2) measurements at the same scale as the analyzed process.
The findings of this dissertation are based on measurements performed with the helicopter-borne platform ACTOS (Airborne Cloud Turbulence Observation System, *Siebert et al.*, 2006a). Due to its low true air speed (TAS) of $20\,\mathrm{m\,s^{-1}}$, which is about 5 times lower than the typical TAS of research aircraft, this platform allows measurements at a spatial resolution on the decimeter scale for selected meteorological parameters (see Chapter 2.1).
This dissertation presents measurements of the CARRIBA[1] experiment, which was conducted in the trade wind regime over Barbados in 2010 and 2011. Barbados is the easternmost Caribbean island and characterized by steady trade winds blowing from the East. Therefore, beside ship tracks or aircraft pollution, there are no additional sources of anthropogenic pollution about 5000 km upstream the island. Occasionally, Barbados is influenced by long-range transport of Saharan dust (*Prospero and Carlson*, 1972; *Smirnov et al.*, 2000; *Reid*, 2002) or biomass-burning particles providing the opportunity to investigate aerosol-cloud interactions under laboratory-like conditions as well as for natural and anthropogenic perturbations.
Finally, the application of collocated measurements at high spatial resolution further offers unique possibilities to analyze aerosol-cloud interactions at a resolution much closer to their process scale than it had been possible for any above mentioned airborne measurements (ACE-2, RICO, VOCALS-REx).

[1]CARRIBA — Clouds, Aerosols, Radiation and tuRbulence in the trade wind regime over BArbados

Aims of this dissertation

In the framework of this dissertation, the following tasks are addressed.

- Characterization of microphysical properties of atmospheric aerosol particles in the trade wind regime.
- Identification and quantification of major factors affecting the cloud droplet number concentration in trade wind cumulus clouds.
- Quantification of the sensitivity of the cloud droplet number concentration towards changes in microphysical properties of aerosol particles including natural and anthropogenic perturbations.

The following chapter introduces shortly the helicopter-borne measurement platform and the applied instruments. Afterwards, the CARRIBA campaigns will be introduced including a characterization of thermodynamics and aerosol particle properties during both intensive observation periods. Chapter 4 contains one case study and a comprehensive statistical analysis of hundreds of individual clouds concerning their sensitivity (in terms of cloud droplet number concentration) towards changes in the aerosol particle properties. This experimental approach is completed by a sensitivity study using a cloud microphysical parcel model. Finally, in chapter 5, two case studies are introduced, which represent scenarios with substantially increased particle number concentrations. This dissertation is summarized in chapter 6.

Chapter 2

Experimental

This chapter presents a short overview of the measurement platform ACTOS (Airborne Cloud Turbulence Observation System) and the instruments and measurement devices important for the determination of aerosol particle and cloud microphysical properties which are used in this work. Furthermore, a cloud microphysical parcel model is introduced.

2.1 Airborne Cloud Turbulence Observation System

The Airborne Cloud Turbulence Observation System (ACTOS) is an autonomous helicopter-borne measurement platform (*Siebert et al.*, 2006a,b).

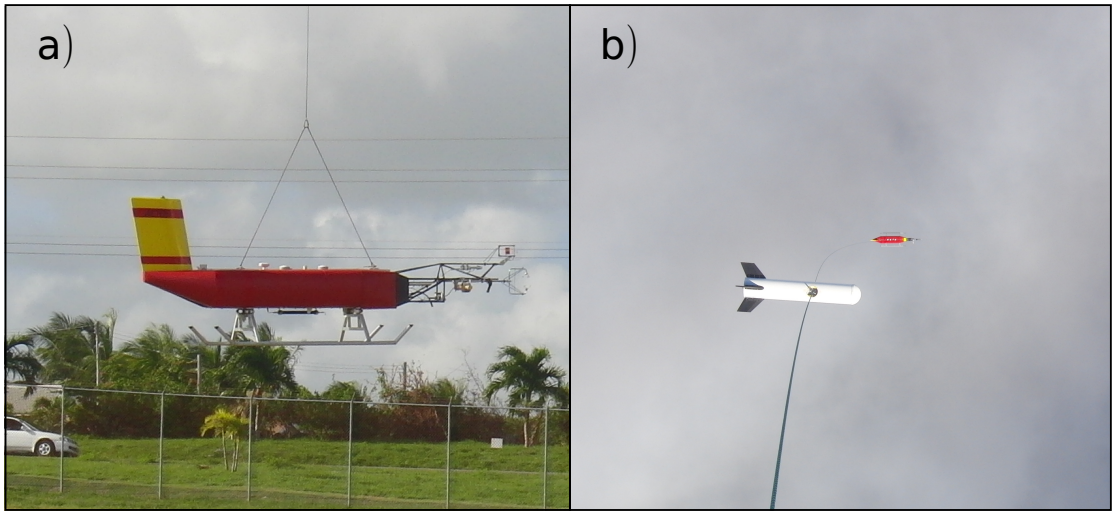

Figure 2.1: Picture of ACTOS during the start (a) and ACTOS and SMART-HELIOS (Spectral Modular Airborne Radiation measurement system for HELIcopter-borne ObservationS) during one research flight from the perspective of the helicopter (b).

ACTOS serves as platform for a multitude of instruments for measuring aerosol particle and cloud microphysical properties as well as standard meteorological and turbulence parameters. The platform itself consists of three major parts. The frontal outrigger carries instruments to measure 3d wind vector, temperature, humidity, and cloud microphysical properties. In the middle part of ACTOS five 19" standard racks are built in, hosting further instruments such as the aerosol instrumentation as well as power supply and data acquisition system. The tail in the back keeps ACTOS in the mean flow direction. During the research flights, a wireless uplink to the helicopter supports the scientist with most important data.
The measurement platform is carried by means of a 140 m-long kevlar cable beneath a helicopter. The typical true air speed (TAS) of about $20\,\mathrm{m\,s^{-1}}$ avoids any measurable influence of the rotor downwash at the measurement altitude. In total ACTOS is about 5 m long, its weight is limited to 200 kg.
The intention behind developing ACTOS was to increase the spatial resolution of airborne measurements. For a fixed temporal resolution of the instruments the only way to increase the spatial resolution is to reduce the speed of the measurement platform. The operational speed of research aircraft typically lies between 80 and $150\,\mathrm{m\,s^{-1}}$, for e.g., the Piper Aztec, the ATR 42, and the Falcon 20 used by SAFIRE, the French office of aircraft instrumented for environmental research (www.safire.fr).
The typical TAS of ACTOS of $20\,\mathrm{m\,s^{-1}}$ increases the spatial distribution already by a factor of four compared to the above mentioned speed of the Piper Aztec. Additionally, sensors with high temporal resolution are applied leading to high spatial resolutions e.g., on the decimeter scale for meteorological measurements. Additionally, a TAS of $20\,\mathrm{m\,s^{-1}}$ is close to wind velocities observed in the planetary boundary layer (PBL). This allows the application of measurement devices originally intended for ground measurements (e.g., sonic anemometer). Furthermore, it avoids thermal heating of sensors and housing.
The Spectral Modular Airborne Radiation measurement sysTem for HELIcopter-borne ObservationS (SMART-HELIOS) completes the measurement setup by providing collocated measurements of the optical properties of the cloud droplets measured by ACTOS. SMART-HELIOS is hanging between ACTOS and the helicopter at a distance of about 20 m beneath the helicopter. Further information about SMART-HELIOS can be found in *Werner et al.* (2013).
The instruments and measured parameters on ACTOS, which are most important for this study are summarized in Tab. 2.1. A description of the instruments for standard meteorological parameters and navigational instruments can be found in *Siebert et al.* (2006a,b).

Instrument	Measured Parameter	Manufacturer
Ultra sonic anemometer	3d wind vector (u, v, w),	Gill Instruments, Lymington, UK
Dewpoint hygrometer, type TP3-ST	dewpoint temperature (T_d), temperature (T)	Meteolabor AG, Switzerland
LICOR 7500	absolute humidity (a)	LI-COR corperation, Lincoln, Nebraska, USA
BAROCAP barometer, type PTB220	static pressure (p)	Vaisala, Helsinki, Finland
Particle volume monitor, type PVM-100A	liquid water content (q_l)	Gerber Scientific, Inc., USA
Phase Doppler Interferometer	droplet concentration (N_d)	Artium Technologies Inc., Sunnyvale, CA, USA
Condensation Particle Counter, model 3762	particle number concentration (N)	TSI Inc., St. Paul, MN, USA
Miniature Cloud Condensation Nucleus Counter	cloud condensation nucleus concentration at different supersaturations (N_CCN)	built by Greg Roberts at Scripps, San Diego, USA and Meteo France, Toulouse, France.
Mobility Particle Size Spectrometer	aerosol particle number size distribution	TROPOS
Optical particle Counter, model 1.129, "SKY-OPC"	aerosol particle number size distribution	Grimm Aerosol Technik GmbH, Ainring, Germany

Table 2.1: Most important instruments and the measured parameters on ACTOS.

2.2 Instruments for aerosol properties

This section introduces the most important instruments to determine the microphysical aerosol particle properties as well the ability of particles to form cloud droplets. The here introduced instruments are attached to a joint inlet designed to sample interstitial aerosol particles with a 50% efficiency cutoff size of $3\,\mu$m. This is realized by a horizontally oriented tube, which is curved 90° downwards. Cutoff characteristics are calculated taking into account aspiration efficiency and losses at the 90° bend (*Baron and Willeke*, 2001). Before entering the instruments the aerosol particles were dried with a diffusion dryer to a relative humidity below 40%.

2.2.1 Condensational Particle Counter

Condensational Particle Counters (CPCs) are widely used to measure aerosol particle number concentrations. These instruments use condensable vapors of a working fluid to grow submicrometer particles to optically detectable sizes (e.g., 10 μm in diameter). Basically, there are three different types of CPCs: (a) expansion-type, (b) continuous-flow-type and (c) mixing-type CPCs (*Baron and Willeke*, 2001).
Here, we use data of two continuous-flow-type CPCs installed on ACTOS (model 3762, TSI Inc., St. Paul, MN, USA). These CPCs consist of three major components: (1) saturator, (2) condenser, (3) optics. First, the aerosol is led through a heated saturator block containing a reservoir of the working fluid (n-butyl alcohol), where the aerosol becomes saturated with respect to the working fluid. Afterwards, it is passed over to a cooled condenser tube. The aerosol cools and the particles grow by condensation of the working fluid onto their surfaces to optically detectable droplets. Droplets are detected by the optics, their signal is post processed by further electronics and converted to a particle number concentration knowing the sample flow rate. Lower detection limits of CPCs in general are on the order of a few nanometers (e.g. *Hermann et al.*, 2007). The above mentioned instruments used on ACTOS are operated with a temperature difference between saturator and condenser of $\Delta T = 25\,\mathrm{K}$ resulting in a 50% detection diameter of $D_{\mathrm{p50}} = 6\,\mathrm{nm}$. The temporal resolution of the applied CPCs is limited to 1 s, their relative measurement uncertainty is on the order of 10%.

2.2.2 Mobility Particle Size Spectrometers

On ACTOS a custom-built mobility particle size spectrometer is applied. In addition, ground-based measurements were performed with a second mobility particle size spectrometer. With both instrument types the electrical mobility distribution of aerosol particles is investigated. Both systems combine a CPC measuring the particle number concentration

with a Differential Mobility Analyser (DMA) to obtain a particle number size distribution. Here, the physical principles of mobility particle size spectrometers are briefly outlined, more information can be found in e.g., *Wiedensohler et al.* (2012). The section starts with a short description of a DMA.

Differential Mobility Analyser

A DMA classifies charged particles with respect to their electrical particle mobility (Z_p) by use of an electrical field. The application of an electrical field to a charged particle results in a drift velocity which depends on the electrical mobility of the particle. Following *Willeke and Baron* (1993, Chapter 18), the electrical particle mobility is denoted as the proportionality constant between the drift velocity of a particle (V_elec) and the applied electrical field of the intensity (E):

$$Z_\mathrm{p} = \frac{V_\mathrm{elec}}{E} = \frac{n \cdot e \cdot C_\mathrm{c}}{3\pi \cdot \eta_\mathrm{air} \cdot D_\mathrm{p}}\,, \tag{2.1}$$

whereby n denotes the number of charges, e is the elementary unit of charge, C_c is the slip correction factor, η_air is the viscosity of air and D_p stands for the particle diameter. The right side of Eq. 2.1 is derived for equilibrium of drag force and electrical force for particle motion in the Stokes regime, see *Willeke and Baron* (1993, Chapter 18).
Naturally, aerosol particles are either uncharged or charged both positively as well as negatively. To establish a charge equilibrium with a well-defined bipolar charge distribution, bipolar diffusion chargers are applied in front of the DMA. In the bipolar diffusion charger, ions are produced from the aerosol carrier gas through interaction with radioactive radiation. These ions then attach to the particles in the aerosol due to Brownian motion and electrostatic forces. This statistical process results in a charge distribution which depends strongly on the particle diameter (e.g., *Fuchs*, 1963; *Gunn*, 1956).
As mentioned above, the DMA classifies particles after their electrical mobility. From Eq. 2.1 it is obvious that the electrical particle mobility is mainly a function of the number of charges (n) and the particle diameter (D_p). For a given n, it is therefore possible to derive the particle size. The application of different electrical field intensities in the DMA (realized by changing the voltage inside the DMA) allows to select particles of different electrical mobilities.

Mobility Particle Size Spectrometers

In general, mobility particle size spectrometers consist of three major instruments: a bipolar diffusion charger, a DMA and a CPC. The basic principle is to select particles of a certain electrical mobility from a polydisperse aerosol with the DMA which are afterwards counted

by a CPC. Therefore, the voltage inside the DMA is changed from low to high values (or vice versa) either step-wise or continuously, while the CPC records the respective particle number concentration.
The resulting electrical particle mobility distribution can be converted into a particle number size distribution (NSD) by an inversion routine taking into account the charge distribution and DMA specifics (e.g. *Hagen and Alofs*, 1983; *Pfeifer et al.*, 2014).
On ACTOS, we use a TROPOS-type scanning mobility particle spectrometer (hereafter called SMPS). It consists of a Hauke-type DMA and a bipolar diffusion charger (Kr-85, model 3077A, TSI Inc., St. Paul, MN, USA). The temporal resolution of this instrument is limited to 2 minutes covering a size range of $6\,\mathrm{nm} \leq D_\mathrm{p} \leq 230\,\mathrm{nm}$. Typically, the measurement uncertainty for particle sizing and number concentration is smaller than 3% and, 10%, respectively.

2.2.3 Optical Particle Size Spectrometer

Optical particle size spectrometers are commonly used to measure particle number size distributions in the size range above few hundreds of nanometers. These instruments use the size dependent scattering of particles for sizing as well as counting. The intensity of the scattered light depends on the particle size, its refractive index and its shape (e.g., *Baron and Willeke*, 2001, Chapter 15). On ACTOS we use the so-called "SKY-OPC" (model 1.129, Grimm Aerosol Technik GmbH, Ainring, Germany). The SKY-OPC uses a laser wavelength of 655 nm and detects the scattered light at a scattering angle of 90° with an opening angle of 60°. The manufacturer calibrated the SKY-OPC with spherical latex particles with refractive index of $m = 1.586 + \mathrm{i}0.0$. The reproducibility of the instrument is ± 3% (given by the manufacturer). During ACTOS research flights we used a measurement frequency of $f = 1\,\mathrm{Hz}$. The SKY-OPC covers a diameter range of $0.3\,\mu\mathrm{m} \leq D_\mathrm{p} \leq 2.6\,\mu\mathrm{m}$.
The particle number size distributions measured by the SKY-OPC are corrected for a different refractive index which is representative for ammonium sulfate particles. For the calculation of complete particle number size distributions in the size range of $6\,\mathrm{nm} \leq D_\mathrm{p} \leq 2.6\,\mu\mathrm{m}$ measurements of mobility and optical particle size spectrometers are combined. Thereby, an inversion routine for multiply charged particles using different instruments is applied, introduced by *Pfeifer et al.* (2014).

2.2.4 Cloud Condensation Nucleus Counter

Cloud Condensation Nucleus Counters (CCNc) were developed throughout the second half of the last century to measure the number concentration of available Cloud Condensation Nuclei (CCN). First instruments to measure CCN concentration (N_CCN) such as the static

diffusion chamber introduced by *Twomey* (1963) used two wet parallel plates where a known supersaturation profile develops allowing measurements at one specific supersaturation (S). Since then, the development of such instruments focused on the fast and accurate measurement of CCN at different supersaturations to obtain information on the CCN spectrum $N_{\mathrm{CCN}}(S)$.

On ACTOS we use a miniature CCNc. This instrument is an advancement of the intrument first intoduced in *Roberts and Nenes* (2005). The miniature CCNc combines two major components: (1) a wettable cylindrical continuous-flow thermal-gradient diffusion chamber and (2) an OPC. In the diffusion chamber, a quasi-uniform centerline supersaturation is developed by establishing a constant temperature gradient. The aerosol flows through the instrument along this centerline. Those particles which serve as CCN at the adjusted supersaturation get activated and grow by condensation. The resulting droplets are counted by an internal optical particle size spectrometer.

The measurement range covers supersaturations between 0.1 and 0.7%. The miniature CCNc can be operated in scanning mode (the supersaturation is scanned throughout the measurement range) or at a fixed supersaturation. The temporal resolution for measurements at a fixed supersaturation is $f = 1\,\mathrm{Hz}$. A complete scan of the entire measurement range lasts 5 minutes.

The measurement uncertainty for counting CCNs is estimated to 10%, the relative uncertainty of the supersaturation is on the order of 10% for supersaturation levels larger than 0.2%. For lower supersaturation levels the relative uncertainty increases.

2.3 Instruments for cloud microphysical properties

The most important instruments to characterize cloud microphysical properties in this study are the Phase Doppler interferometer (PDI) and the particle volume monitor (PVM).

2.3.1 Phase Doppler Interferometer for Cloud Turbulence

The Phase Doppler Interferometer for Cloud Turbulence (PICT) uses phase Doppler interferometry to measure size and velocity of spherical water droplets. Basic principles of phase Doppler interferometry can be found in *Chuang et al.* (2008). The PICT is a commercial flight-PDI (phase Doppler interferometer) manufactured by Artium Technologies, Inc, Sunnyvale, CA, USA.

The measurement principle is based on light scattering interferometry (see details in *Chuang et al.*, 2008). The measurement volume of the PDI is defined by two focused light beams intersecting at a known angle. The cross-section of the

intensity in the measurement volume is characterized by the Gaussian profiles of the two identical laser beams and a high-frequency interference field resulting from constructive and destructive interference. Droplets passing through the measurement volume scatter light which is detected by 3 detectors. The measured Doppler frequency and the phase shift of the signal detected at two different detectors is related to the droplet velocity and diameter (D_d).
The flight-PDI measures single droplets sizing between $1\,\mu m \leq D_\mathrm{d} \leq 100\,\mu$m instantaneously. The determined droplet number concentration has an accuracy of about 10%.

2.3.2 Particle Volume Monitor

The liquid water content (q_l), integrated particle surface area (PSA) and the effective droplet radius (r_e) of cloud droplets are measured with the particle volume monitor (PVM-100A, *Gerber*, 1991). The PVM detects the scattered light of a laser with a wavelength of 780 nm. Source and detectors are located face to face, the droplets pass the sampling volume perpendicularly. PVM measurements are supposed to have an accuracy of 10%.

2.4 Ground Measurements

Two ground-based measurement stations located at the easternmost tip of Barbados allow to compare long time measurements with data obtained during two intensive field campaigns described in Chapter 3.

2.4.1 Ragged Point

The Ragged Point station is operated by the University of Miami and is famous for the continuous measurements of mineral dust for more than 40 years (*Prospero and Lamb*, 2003). The station is equipped to measure standard meteorology. Aerosol particles were sampled with an inlet system at the top of a 17 m high mast. During the two CARRIBA campaigns (introduced in Chapter 3), one mobility particle size spectrometer (herafter called DMPS) covering a size range of $25\,\mathrm{nm} < D_\mathrm{p} < 500\,\mathrm{nm}$ was operated. In parallel, a CCNc (Droplet Measurement Technologies, Boulder, CO, USA; model CCN-100) was installed to measure the size-segregated activation of particles to cloud droplets, allowing to calculate the hygroscopicity parameter κ following the approach of *Petters and Kreidenweis* (2007) (see Eq. A.7).
A miniature CCNc similar to the one on ACTOS was operated, scanning the total number concentration of cloud condensation nuclei for supersaturations between 0.1–0.7%. For the

DMPS, CCNc and miniature CCNc measurements the aerosol was dried to a relative humidity below 25%. All three instruments were operated downstream of a cyclone with an upper size cut of 500 nm. Furthermore, daily filter samples were taken by the University of Miami which were analyzed for the bulk chemical composition of the aerosol.
The ground-based instruments are supposed to measure with the same accuracy as the above introduced airborne instruments.

2.4.2 Deebles Point

The Barbados Cloud Observatory (BCO) is a remote sensing facility located at the east coast of Barbados at Deebles Point. It is operated by the Max Planck Institute for Meteorology (MPI-M) in Hamburg and was built up in 2010. The BCO is equipped with weather sensors, a Raman LIDAR, a water vapor DIAL, a scanning cloud radar, a micro rain radar, a ceilometer and an allsky-imager. Further information can be found in e.g., *Nuijens et al.* (2013).

2.5 Cloud microphysical parcel model

In the context of this work, the cloud parcel model of *Simmel and Wurzler* (2006) is used. The model contains detailed cloud microphysics and uses one common high-resolution grid for aerosols and cloud droplets (264 bins). Here the model is run with a moving size-bin approach to avoid numerical diffusion along the mass axis.
The input parameters for the model are:

- dry particle number size distribution
- bulk hygroscopicity (κ)
- initial relative humidity (rH)
- initial static pressure (p)
- initial temperature (T).

In the first model step, the wet aerosol particle number size distribution is calculated for ambient relative humidity. Afterwards, the model is run with a prescribed vertical wind velocity. The model calculates the adiabatic expansion and the following changes to the thermodynamic variables. Since the focus of this work is on CCN activation and initial droplet growth, collision/coalescence and entrainment processes are not considered.
The governing equation for droplet growth is defined by (from *Pruppacher and Klett* (1997), *Simmel and Wurzler* (2006)):

$$\frac{\mathrm{d}m}{\mathrm{d}t} = \frac{4\pi r(s_\infty - s_{\mathrm{eq}})}{(\frac{L_\mathrm{v}}{R_\mathrm{v}T} - 1)\frac{L_\mathrm{v}}{K^* T} + \frac{R_\mathrm{v}T}{e_{\mathrm{s,\,w}}(T)D^*}}\,, \tag{2.2}$$

where m denotes the droplet mass, t the time, r the particle radius, s_∞ the saturation ratio of the surrounding air, s_{eq} the equilibrium supersaturation ratio at the particle/air interface, L_{v} is the latent heat of condensation[1], R_{v} the gas constant of water vapor[2], T the air temperature, K^* the modified thermal conductivity of air[3], $e_{\mathrm{s,\,w}}(T)$ the saturation water vapor pressure and D^* the modified diffusion coefficient for water vapor in air[4]. For further information about K^* and D^* see Appendix B.

In this work, several model runs with different objectives are performed. The used input parameters are based on the measurements by ACTOS and documented at the respective positions in the text.

[1] $L_{\mathrm{v}} = 2.5 \cdot 10^6\,\mathrm{J\,kg^{-1}}$
[2] $R_{\mathrm{v}} = 461.5\,\mathrm{J\,kg^{-1}\,K^{-1}}$
[3] K^* given in $\mathrm{W\,m^{-1}\,K^{-1}}$
[4] D^* given in $\mathrm{m^2\,s^{-1}}$

Chapter 3

Clouds, Aerosols, Radiation and Turbulence in the Trade Wind Regime over Barbados — CARRIBA

The CARRIBA (Clouds, Aerosols, Radiation and tuRbulence in the trade wInd regime over BArbados) experiment covers two intensive measurement periods in the trade wind regime over Barbados. The first campaign was performed in the climatic wet season in November 2010 ($\text{CARRIBA}_{\text{wet}}$) and the second campaign in the climatic dry season in April 2011 ($\text{CARRIBA}_{\text{dry}}$).

The trade wind regime develops due to large scale subsidence north and south of the Intertropical Convergence Zone (ITCZ). This subsidence follows as a consequence of the Hadley circulation. The Hadley circulation itself is a near-meridional circulation, which results from strong heating at the Earth's surface close to the equator. The heating is followed by the development of deep convection.

Considering the northern hemisphere, the deep convection results at high altitudes in air motion towards the North. The compensating air flow at the surface is directed to the South but bent to West, due to the Coriolis force[1] (North-East trade winds).

As a result of large scale subsidence, the so-called trade inversion is developed (usually at an altitude above 2 km, decreasing to the North). The stratification in the trade wind regime over the ocean is defined by three layers: (1) the well-mixed marine boundary layer close to the surface, (2) a conditionally unstable stratified cloud layer, which is topped by the trade inversion and, (3) the free troposphere above the trade inversion.

In the cloud layer, shallow cumulus convection is one of the most prevalent cloud formation

[1] The Coriolis force is a fictitious force. It is exerted on a body which moves in a rotating reference frame.

mechanisms. Moist convection, embodied by the so-called trade wind cumuli, plays an important role in the transport of moisture, momentum and heat from the well-mixed layer into higher altitudes (*Tiedtke*, 1989). Thus trade wind cumuli significantly influence the dynamics of the entire planetary boundary layer of the whole trade wind regime.

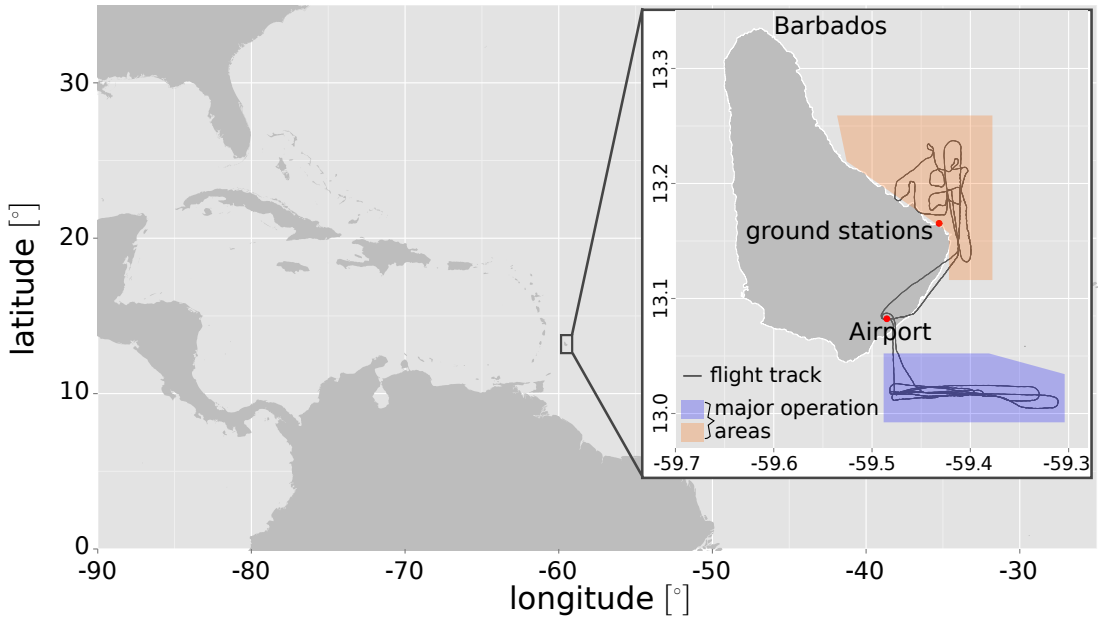

Figure 3.1: Map of Latin America and the Caribbean Sea. The Inlay shows an enlarged map of Barbados. Red dots denote the location of the airport and the ground stations at the East coast. Blue and orange boxes display the major operation areas off the east and south coast. Grey lines indicate examples of two typical flight patterns.

Core platforms and instruments involved in this campaign are ACTOS and SMART-HELIOS, which are introduced in Chapter 2. Furthermore, two ground stations were operated at Deebles Point and Ragged Point (both located at the East coast of Barbados). The Ragged Point station is operated by the University of Miami. It is famous for its long-term dust record back to the 1960's (*Prospero and Lamb*, 2003). Both CARRIBA campaigns are embedded into a long-term initiative of the Max Planck Institute for Meteorology (MPI-M) in Hamburg, Germany. The MPI-M operates the Barbados Cloud Observatory (BCO) at Deebles Point since April 2010. The BCO is equipped with several remote sensing instruments (e.g., Raman lidar, cloud and rain radar). Additionally, the campaigns were supported by the local Caribbean Institute for Meteorology and Hydrology (CIMH).

Figure 3.1 shows a map of Latin America and Barbados including information on the location of the airport, ground stations and major operation areas. The CARRIBA campaigns are introduced in detail in *Siebert et al.* (2013). Therefore, the location and the scientific

questions of the campaign are only briefly discussed here, followed by a general overview about the meteorological conditions and aerosol microphysical properties with the help of airborne and ground-based measurements.

3.1 Leading research interests of CARRIBA

Barbados is the easternmost Caribbean island (13°10' N, 59°33' W), climatologically located in the trade wind regime. The trade wind regime is characterized by prevailing wind coming from East to North-East and stationary meteorological conditions. Hence, beside ship or aircraft emissions there are no sources of anthropogenic pollution about 5000 km upstream, offering laboratory-like conditions to study aerosol particles and clouds in the trade wind regime. Certain seasons are characterized by the influence of lofted aerosol layers advected by large scale transport. Past studies reported the presence of Saharan dust (e.g. *Prospero and Carlson* (1972), *Smirnov et al.* (2000), *Reid* (2002)) and biomass burning aerosol (*Haywood et al.*, 2008) over Barbados.
The scope and scientific questions of the CARRIBA campaign is widely discussed in *Siebert et al.* (2013). A brief summary of the four leading research interests is given here (adapted from *Siebert et al.*, 2013):

- **Clouds:** Investigation of cloud microphysical properties in different cloud regions and for different evolution stages.
- **Aerosol particles:** Characterization of aerosol microphysical properties in the cloud and sub-cloud layer. Influence of aerosol particles on the microphysical properties of clouds as well as the influence of clouds on aerosol particles.
- **Radiation:** The susceptibility of trade wind cumuli towards changes in the physical properties of aerosol particles is investigated with remote sensing techniques. Retrieved microphysical properties are compared to collocated in-situ measurements.
- **Turbulence:** The turbulent dynamics and thermodynamics of the sub-cloud layer, cloud environment, and cloud edges including the entrainment process are investigated. Furthermore, the turbulent in-cloud mixing and its influence on the cloud microphysical properties will be quantified.

The focus of this work is the characterization of the microphysical properties of aerosol particles. Additionally, the susceptibility of the cloud droplet number concentration towards changes in the aerosol particle properties is investigated.

3.2 Overview

During both intensive measurement campaigns, 31 research flights were performed. Typically, one research flight lasted about 1.5 to 2 h, covering a vertical profile in the beginning, followed by cloud chasing at different altitudes. Major operation areas are displayed in Fig. 3.1. The majority of research flights were performed in the area east of the ground stations. During two research flights ACTOS measured at the west coast of Barbados. A table of all research flights performed during $\text{CARRIBA}_{\text{wet}}$ and $\text{CARRIBA}_{\text{dry}}$ is given in Appendix C.

Figure 3.2 shows median values of selected quantities calculated for the sub-cloud layer (SCL, $z_{\text{baro}} < 400\,\text{m}$) and the cloud layer (CL, $700 < z_{\text{baro}} < 2000\,\text{m}$) of each research flight. The calculated median values for the CL are free of any direct cloud influence. Cloud passages are filtered out with the help of liquid water content measurements.

During $\text{CARRIBA}_{\text{wet}}$, the median potential temperature θ in the SCL varies in a small range of 299.9 K to 301.1 K with an overall median of $\theta = 300.6\,\text{K}$. The range of observed median θ in the SCL during $\text{CARRIBA}_{\text{dry}}$ is slightly larger covering values between 298 and 299.7 K. The overall median is $\theta = 299.1\,\text{K}$.

The specific humidity q features larger variability. The overall median calculated for the SCL is $17.3\,\text{g}\,\text{kg}^{-1}$ ($15.3\,\text{g}\,\text{kg}^{-1}$) for $\text{CARRIBA}_{\text{wet}}$ ($\text{CARRIBA}_{\text{dry}}$). In total the median values calculated for each flight vary between 14.3 and $18.6\,\text{g}\,\text{kg}^{-1}$.

Both campaigns featured a similar range of observed horizontal wind speed UU ranging between 3.1 and $11.2\,\text{m}\,\text{s}^{-1}$ for the SCL. Wind direction dd is generally NE to E during both campaigns with some exceptions during $\text{CARRIBA}_{\text{dry}}$. During two episodes (doy 104–107 and doy 112–114) the median wind direction turned towards ESE.

The median total particle number concentration N in the SCL varies during both campaigns between 130 and $610\,\text{cm}^{-3}$, while the median concentration of cloud condensation nuclei at 0.26% supersaturation $N_{\text{CCN, 0.26\%}}$ is between 30 and $400\,\text{cm}^{-3}$.

In general, all quantities in the SCL feature a very low interquartile spread (black error bars) pointing towards well-mixed conditions during each research flight.

The CL is characterized by a higher θ, which is due to the conditionally unstable stratified (and not well-mixed) atmosphere. The higher range in θ results from the larger averaging height (700–2000 m). Specific humidity q behaves opposite with generally lower values in the CL, but also featuring an increased interquartile spread, resulting from the conditionally unstable stratification, which hinders the vertical moisture transport.

The horizontal wind speed is mostly similar in the SCL and CL. Larger differences are obvious during an episode in November (doy 324–327), in which a decrease in UU with increasing altitude was observed. The same holds true for dd. In this case, larger differences

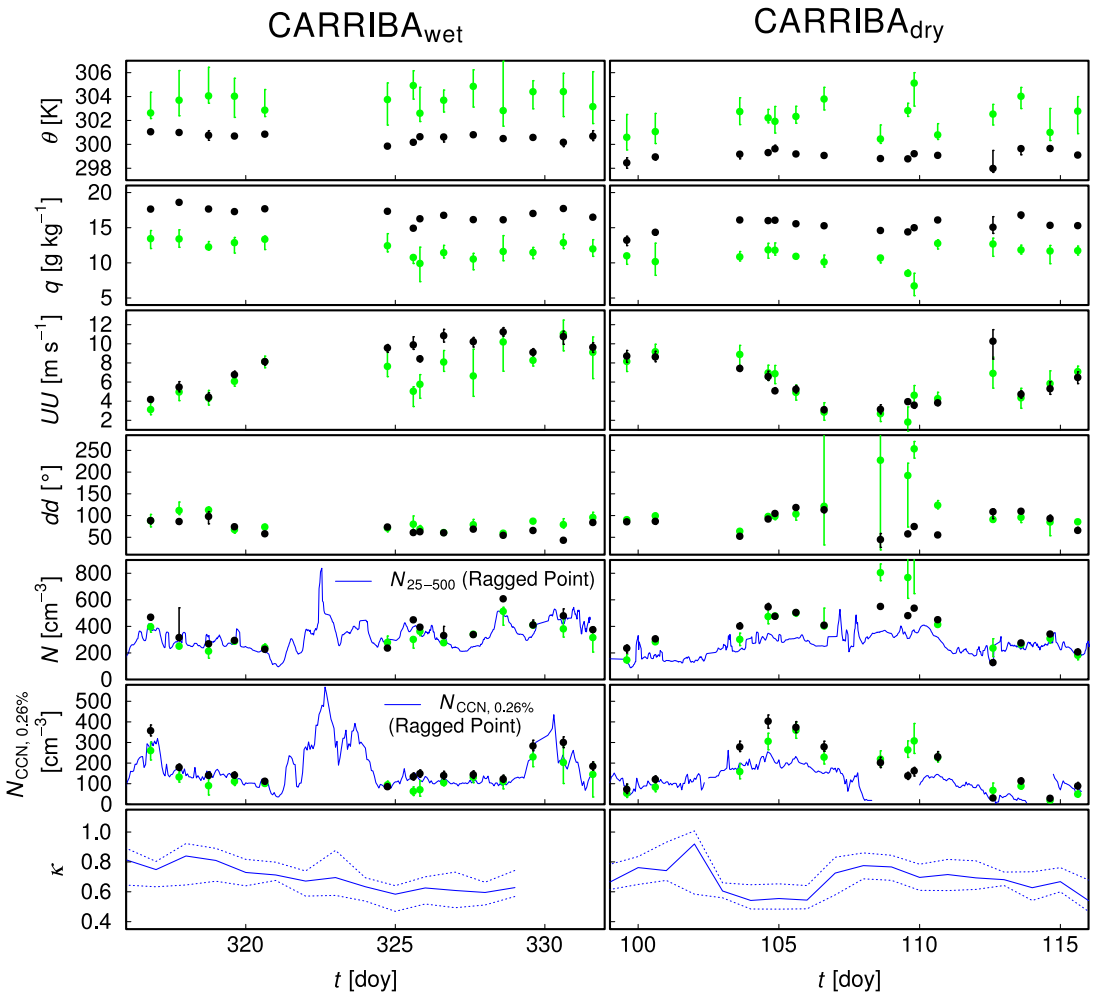

Figure 3.2: Median values and interquartile spread (error bars) of potential temperature (θ), specific humidity (q), horizontal wind speed (UU), wind direction (dd), total particle number concentration for particles larger than $D_p > 6\,nm$ (N) and cloud condensation nucleus concentration measured at 0.26% supersaturation ($N_{CCN,\,0.26\%}$). Quantities are calculated for sub-cloud layer (black) and cloud layer (green) of each research flight. Additionally, median N_{25-500} (total particle number concentration for particles in the size range of $25\,nm < D_p < 500\,nm$), $N_{CCN,\,0.26\%}$ and κ measured at Ragged Point are shown in the lowermost three panels (blue lines). Dashed lines in the lowermost panel represent the interquartile spread.

are observed during an episode of low horizontal wind speed with variable wind direction.

For many flights N and $N_{CCN,\,0.26\%}$ show similar values in CL and SCL. Differences between CL and SCL values vary from flight to flight. In cases of strong layering, CL and SCL values strongly differ (e.g., during doy 104–106, where Barbados was influence by lofted layers of Saharan dust).

In addition to the airborne data, Fig. 3.2 presents ground-based measurements observed at Ragged Point. For technical reasons, all aerosol instruments at Ragged Point were operated down-stream of a cyclone with a size cut of $D_{\mathrm{p,\,cut}} \approx 500\,\mathrm{nm}$, while the upper size cut of the airborne measurements is $D_{\mathrm{p,\,cut}} \approx 2500\,\mathrm{nm}$. Therefore, following comparisons refer to different particle size ranges. The number concentration of particles in the size range of $25\,\mathrm{nm} < D_{\mathrm{p}} < 500\,\mathrm{nm}$ (N_{25-500}) agrees with average values of N (total particle number concentration for particles larger than $D_{\mathrm{p}} > 6\,\mathrm{nm}$) in the SCL within $\pm 15\%$ during $\mathrm{CARRIBA_{wet}}$. During $\mathrm{CARRIBA_{dry}}$, N_{25-500} underestimates the airborne measurements of N especially during the dust period (doy 104–106) and a second period during doy 108–110. Possible reasons for the mismatch are the different size ranges of N and N_{25-500} and vertical inhomogeneities. Losses in the inlet line from the measurement tower to the instrument at Ragged point were corrected according to the best of knowledge (cf. Sec. 2.4.1). Nevertheless, errors from that correction cannot be fully precluded.

The CCN measurements ($N_{\mathrm{CCN,\,0.26\%}}$) show a similar behavior as reported for N and N_{25-500}. While during the first campaign the agreement between ground-based $N_{\mathrm{CCN,\,0.26\%}}$ and airborne measurements is good, there is a underestimation during the same periods as mentioned above (doy 104–106 and doy 108–110), possibly resulting from the same reasons.

The lowermost panel shows averaged κ values derived from size-segregated activation behavior measured with a combination of DMA and CCNc. The hygroscopicity parameter κ roughly varies within 0.6 and 0.8, while the overall mean for both campaigns is $\kappa = 0.7$. During the dust period κ shows constantly lower values of $\kappa = 0.6$.

Vertical profiles

In this subsection, vertical profiles of selected parameters measured over the ocean East of Barbados are presented. Filters were applied to ensure that the profiles are free of any direct influence of clouds or the island.

Figure 3.3 shows median vertical profiles of the cloud-free atmosphere up to an altitude of $z_{\mathrm{baro}} = 3000\,\mathrm{m}$ for $\mathrm{CARRIBA_{wet}}$. The profiles are calculated for height bins of 50 m, the shaded area denotes the 5th and 95th percentile of the observations to demonstrate the overall spread of the observations.

Vertical profiles of θ feature very low variation with values around 301 K as well as well-mixed conditions in the SCL. Above $z_{\mathrm{baro}} \approx 600\,\mathrm{m}$, θ increases representing conditionally unstable stratification. The specific humidity q is generally highest in the SCL and varies around $17\,\mathrm{g\,kg^{-1}}$. Above the SCL, q decreases with some stronger dips, indicating drier lofted layers. Within the SCL, 90% of observed q is between 15 and $20\,\mathrm{g\,kg^{-1}}$. The relative humidity shows the lowest variation in the SCL with values around 80%. The increased spread in higher

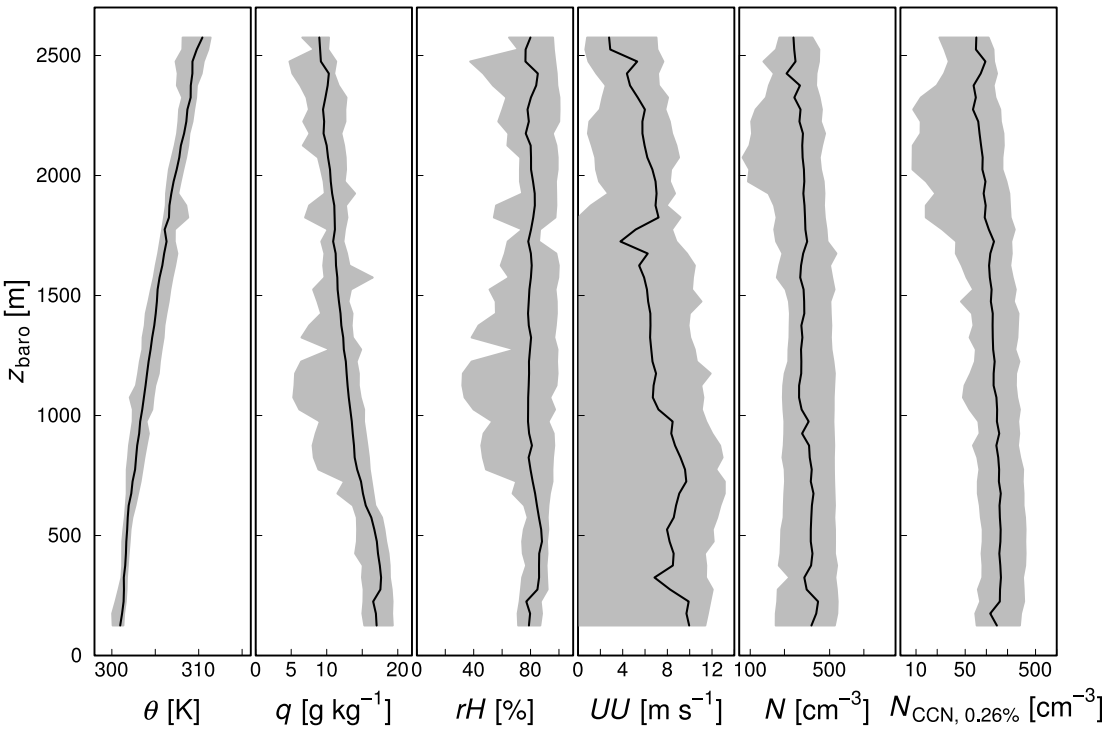

Figure 3.3: Median vertical profiles (black lines) of potential temperature (θ), specific humidity (q), relative humidity (rH), horizontal wind speed (UU), aerosol particle number concentration (N) and CCN number concentration measured at 0.26% supersaturation ($N_{\mathrm{CCN,\,0.26\%}}$) during CARRIBA$_{\mathrm{wet}}$. The shaded area denotes 5th and 95th percentile. Quantities are calculated for altitude bins of 50 m.

altitudes results from penetrating drier air layers as well as upwelling plumes of moist air. The horizontal wind speed varies up to 12 m s^{-1} with a weak tendency to lower values for increasing altitude. Median profiles of the wind direction are not shown here since averaging between flights may lead to confusing results.

Average profiles of N and $N_{\mathrm{CCN,\,0.26\%}}$ do not show significant gradients, which is due to the averaging. In total, N ($N_{\mathrm{CCN,\,0.26\%}}$) varies roughly between 100 and 600 cm^{-3} (20 and 450 cm^{-3}).

Figure 3.4 shows a similar plot as Fig. 3.3 but for CARRIBA$_{\mathrm{dry}}$. In general, the vertical profiles show similar results as for CARRIBA$_{\mathrm{wet}}$, with some exceptions. The potential temperature θ and q are slightly lower (roughly by 1 K and 2 g kg^{-1}). The observed range of N is dramatically increased to 100–5000 cm^{-3} which can be attributed to observed local anthropogenic pollution event on April 19. The variation of $N_{\mathrm{CCN,\,0.26\%}}$ is also increased however less pronounced (20–500 cm^{-3}).

The shaded areas represent 90% of all measurements emphasizing the low variability for θ,

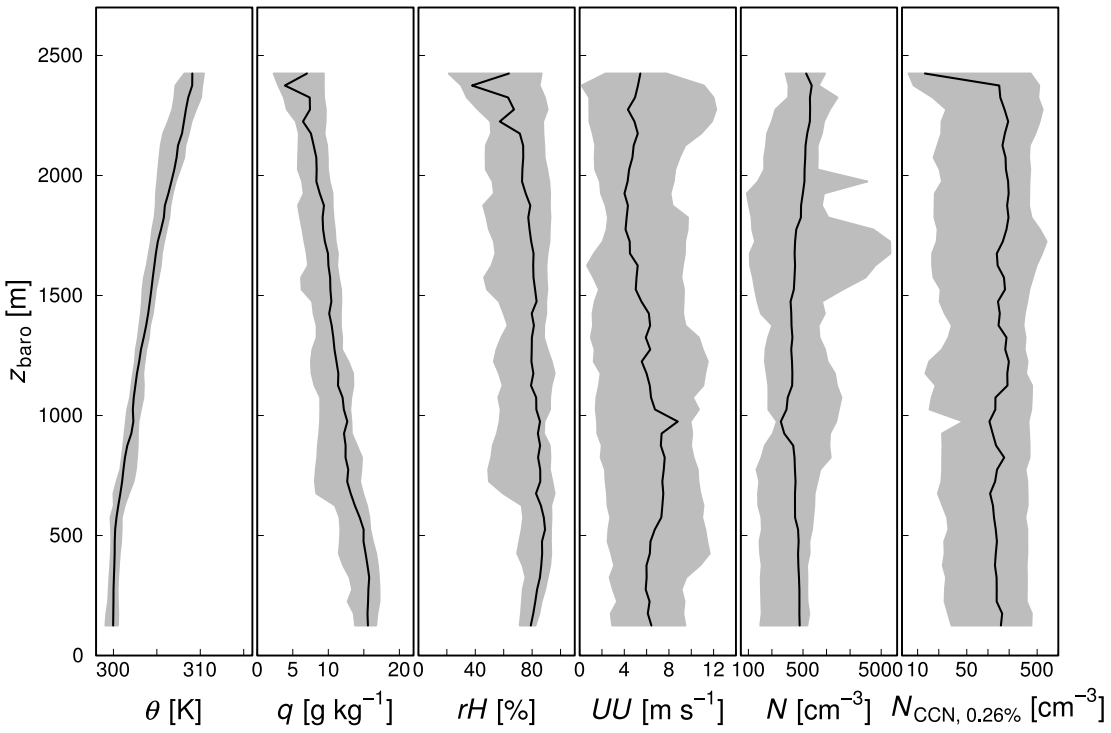

Figure 3.4: Median vertical profiles (black lines) of potential temperature (θ), specific humidity (q), relative humidity (rH), horizontal wind speed (UU), aerosol particle number concentration (N) and cloud condensation nucleus concentration measured at 0.26% supersaturation ($N_{\mathrm{CCN},\,0.26\%}$) during CARRIBA$_{\mathrm{dry}}$. The shaded area denotes 5th and 95th percentile. Quantities are calculated for altitude bins of 50 m.

q and rH (at least for the SCL) observed during both CARRIBA campaigns.

Aerosol particle number size distributions

Figure 3.5 gives an overview over the observed aerosol particle number size distributions (NSDs) measured in the sub-cloud and cloud layer during CARRIBA$_{\mathrm{wet}}$ (left picture) and CARRIBA$_{\mathrm{dry}}$ (right picture). The shaded area corresponds to the spread between the 5th and 95th percentile of all observations (possible contamination during start and landing procedure is excluded).

Even though Fig. 3.5 shows averaged data, the marine nature is visible. The median NSDs feature for both campaigns a bimodal structure with a distinct Hoppel minimum around $D_{\mathrm{p}} \approx 80\,\mathrm{nm}$ and comparable particle number concentration. In general, for both campaigns the range of observations for particles smaller than $D_{\mathrm{p}} \approx 15\,\mathrm{nm}$ increases, which is due to an increased measurement uncertainty in that size range and occasionally observed events of new particle formation at higher altitudes and in the vicinity of clouds. Focusing on accumulation

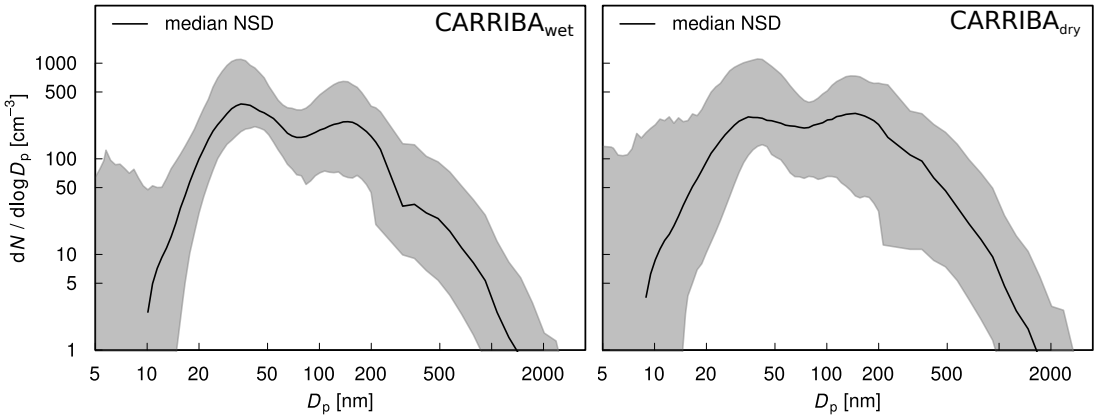

Figure 3.5: Median aerosol particle number size distributions measured in the sub-cloud and cloud layer during CARRIBA$_{\mathrm{wet}}$ and CARRIBA$_{\mathrm{dry}}$. Shaded area represents 90% of all measurements.

mode particles (80 nm $< D_{\mathrm{p}} <$ 1 μm), the NSDs observed during CARRIBA$_{\mathrm{dry}}$ feature larger values and an increased range. As already mentioned above, Barbados was influenced by Saharan dust during the second campaign, explaining this increase. The increased range during CARRIBA$_{\mathrm{dry}}$ also implies a larger variability in the CCN concentration, which agrees well with a larger variability of $N_{\mathrm{CCN,\,0.26\%}}$ observed for the whole altitude range (compare vertical profiles Fig. 3.3 and Fig. 3.4).

In contrast to the comparatively low variability of the meteorological parameters (e.g., θ, q), the NSDs show a wide spread of observations (please note the logarithmic scale). Particularly, the large variability in the accumulation mode size range significantly influences the CCN concentration. Moreover, the vertical distribution of total particle and CCN number concentration features different layers.

Comparison of ground based and airborne aerosol measurements

The above shown vertical profiles give already an impression about the vertical distribution of particle and CCN number concentration. In the presence of lofted aerosol layers, ground-based measurements cannot represent the aerosol properties at higher altitude sufficiently. Nevertheless, for the well-mixed conditions in the SCL, ground-based measurements are supposed to agree with airborne measurements. Figure 3.2 shows flight-averaged ground-based data of total particle number concentration and CCN concentration compared to measurements in the SCL. As discussed above, the agreement is remarkable well with some exceptions.

Figure 3.6 shows mean particle number size distributions (NSDs) measured at Ragged Point

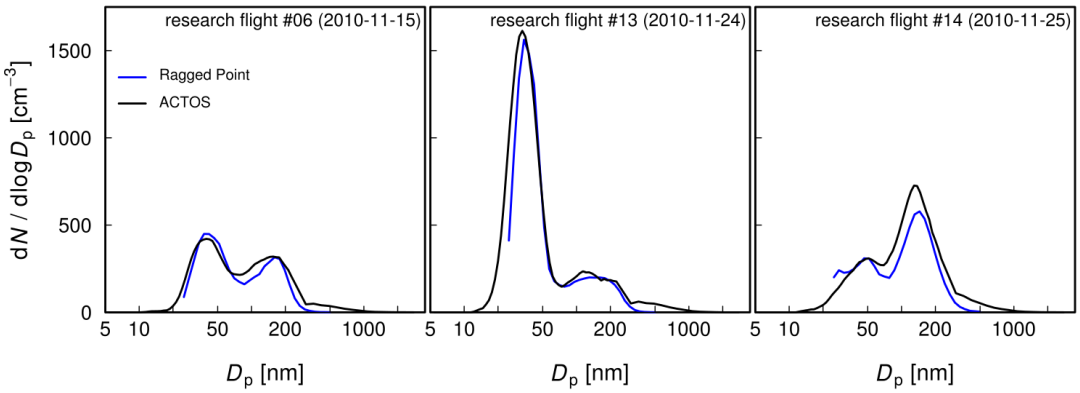

Figure 3.6: Comparison of aerosol particle number size distributions (NSDs) measured at Ragged Point (blue lines) and on ACTOS (black lines) for 3 different research flights. Ground based NSDs are averaged over the flight time of ACTOS. Airborne NSDs are averaged over measurements inside the sub-cloud layer.

and inside the SCL for three different research flights (#06, #13 and #14). Ground-based NSDs are averaged over the time of the respective research flight of ACTOS. The NSDs show three different shapes featuring either a dominating Aitken (#13), a dominating accumulation mode (#14), or equal concentration in both modes (#06) which is representative for a large portion of all observations during CARRIBA (cf. Fig. 3.5). For all three different flights and different shapes of the NDSs, the mean mode diameters and their particle number concentration measured at Ragged Point and with ACTOS agree within $\pm 15\%$. There is a constant underestimation of the ground-based measurements for particles larger than $D_\mathrm{p} \approx 500\,\mathrm{nm}$ which results from their upper size limit (see Section 2.4.1). These results indicate that ground-based measurements are to major degree representative for the aerosol properties in the well-mixed SCL.

Chapter 4

Statistical Analysis of individual Clouds

This chapter is motivated by the question: What controls cloud droplet number concentration of trade wind cumuli. First, a comparison of the number size distributions of interstitial particles inside one cloud and the particle number size distributions in the cloud-free environment is presented. Furthermore, a method to derive the number concentration of activated particles is introduced, which serves as the basis for a comprehensive statistical analysis covering individual clouds from 10 research flights. The statistical analysis is supported by a sensitivity study using a cloud microphysical parcel model.

4.1 Case study: Comparison of activated and non-activated aerosol particles

In the following section, the vertical stratification as well as measurements at cloud level during research flight #06 (cf. Tab. C.1) on Nov. 15th, 2010 are presented with emphasis on comparing the microphysical properties of the activated and non-activated aerosol particles.
The horizontal dimensions of each of the trade wind cumuli measured during the two intensive campaigns was often on the order of several hundred meters. Since the mobility particle size spectrometer (SMPS, see Sec. 2.2.2) has a measurement frequency of $f = 1/120\,\mathrm{s}^{-1}$, it is not possible to obtain complete particle number size distributions (NSDs) inside of clouds with a horizontal extend less than $d = \mathrm{TAS} \cdot f^{-1} = 20\,\mathrm{m\,s}^{-1} \cdot 120\,\mathrm{s} = 2.4\,\mathrm{km}$.
During this research flight, it was however possible to obtain complete in-cloud particle number size distributions. Research flight #06 started at 10:07 and ended at 11:40 local time. The research flight featured a typical flight pattern for a flight under cloudy conditions

starting with a horizontal leg at 250 m asl over the open sea off the east coast of Barbados. After reaching the navigation point C1, a vertical profile was performed between C1 and C2 up to an altitude of 2300 m asl . This part of the research flight was followed by cloud chasing in altitudes between 800–1750 m. Finally, ACTOS flew back to the airport along the east coast of Barbados. The complete flight track is plotted as a projection on the ground surface in Fig. 4.1(b).

4.1.1 Vertical Stratification

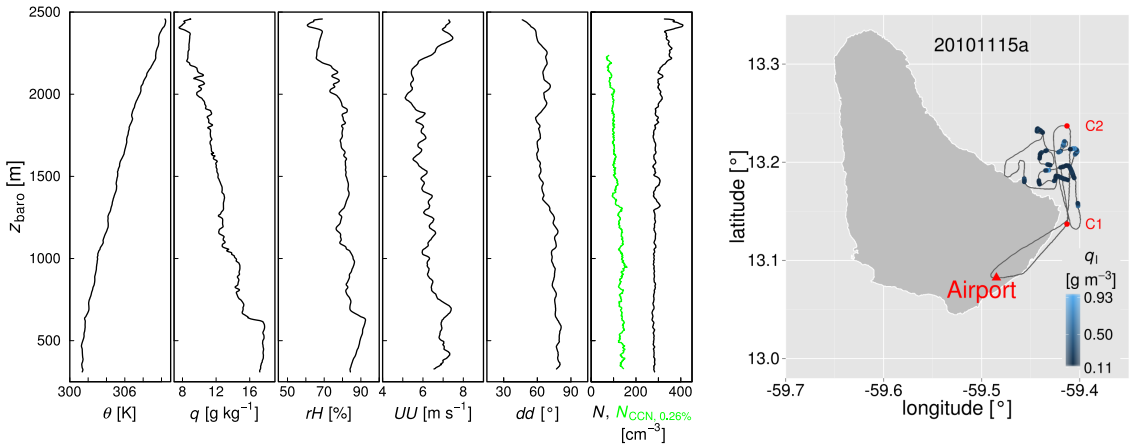

(a) Vertical profiles of selected parameters.

(b) Flight track and clouds.

Figure 4.1: Left panel: vertical profiles of potential temperature (θ), specific humidity (q), relative humidity (rH), horizontal wind speed (UU), wind direction (dd), total particle number concentration and CCN concentration (at 0.26%, green line) corrected for standard temperature and pressure (N, $N_{\mathrm{CCN},\,0.26\%}$). Right panel: flight track of ACTOS (grey line) and measured liquid water content (q_l) as indicator of the location of the observed clouds. Additionally, the location of the airport and the navigational points C1 and C2 is given.

In the left panel of Fig. 4.1, vertical profiles of potential temperature (θ), specific humidity (q), horizontal wind speed (UU), wind direction (dd), total particle number concentration (N) and CCN number concentration measured at 0.26% supersaturation ($N_{\mathrm{CCN},\,0.26\%}$) both corrected to standard temperature and pressure are shown. All presented aerosol particle and CCN data in this work are corrected to standard temperature and pressure (stp)[1]. From the vertical profiles of q and θ, the atmosphere can be divided into two major parts: (a) a well-mixed layer up to 600 m asl, and (b) the cloud layer above 600 m asl, which is consistent with the average vertical profiles shown in Sec. 3.2. The potential temperature features constant

[1]standard temperature and pressure: $T = 288.15\,\mathrm{K}$, $p = 1013.25$ hPa

values around 301 K in the well-mixed layer and an increase with increasing altitude above. The average $\mathrm{d}\theta/\mathrm{d}z_{\mathrm{baro}} \approx 5\,\mathrm{K\,km^{-1}}$ in the cloud layer indicates a conditionally unstable stratified atmosphere. Within the well-mixed layer, q stays almost constant at $q = 17\,\mathrm{g\,kg^{-1}}$. At higher altitudes, q decreases with increasing altitude. rH increases during the lowermost 600 m from 83% to above 90%. Above the well-mixed layer, rH decreases and ranges within 65–80%.

Wind direction and horizontal wind velocity do not show significant vertical gradients and represent typical trade wind conditions with wind from East-North-East with $6\,\mathrm{m\,s^{-1}}$. The total particle number concentration features almost constant conditions of $N \approx 300\,\mathrm{cm^{-3}}$ up to an altitude of $z = 1800\,\mathrm{m}$. Above, N increases with increasing z_{baro}. The CCN concentration decreases slightly with increasing altitude, mean values in the well-mixed layer are close to $135\,\mathrm{cm^{-3}}$.

In comparison to the average vertical profiles presented in Fig. 3.3, research flight #06 represents typical conditions measured during $\mathrm{CARRIBA_{wet}}$.

The right panel in Fig. 4.1 shows the flight track of ACTOS during research flight #06 and the locations of the observed clouds (bluish dots). In this particular flight, all clouds were sampled over the ocean between the navigational points C1 and C2 and north-west of Ragged Point.

4.1.2 Measurements at cloud level

Figure 4.2 shows time series of observed parameters during the whole flight (left figure). The uppermost panel illustrates again the flight pattern beginning with a horizontal leg at constant altitude followed by a vertical profile and the cloud chasing part. The lowermost panel shows the liquid water content (q_{l}) which should in this context only indicate when ACTOS penetrated clouds. In the panel in between, N is plotted featuring an almost constant value of $N = 300\,\mathrm{cm^{-3}}$ in the vicinity of clouds, which is interrupted by plunges at the same time when q_{l} increases.

The aerosol inlet on ACTOS is designed to measure the interstitial aerosol particles exclusively (see. Sec. 2.1). Therefore, particles activated to cloud droplets do not enter the inlet system, which explains the plunges in the time series of N in the presence of clouds. The right panel in Fig. 4.2 shows a subsection of the recorded time series of N and q_{l} for an approximately 12 km long horizontal leg at about 1500 m altitude to underline the anti-correlation of N and q_{l}.

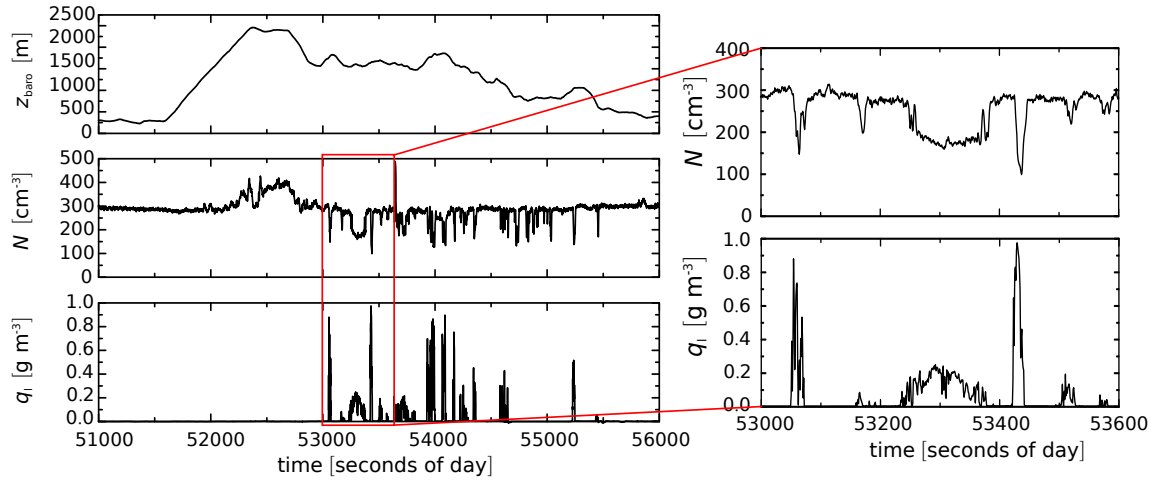

Figure 4.2: Time series of barometric height (z_{baro}), total aerosol concentration (N) and liquid water content (q_{l}).

4.1.3 Activated and non-activated aerosol particles

Figure 4.3 shows particle number size distributions inside (blue lines) and outside (red lines) of clouds (all NSDs are corrected to stp). The NSDs outside of clouds feature a bimodal shape with a distinct minimum, which is typical for a marine submicrometer aerosol (*Hoppel et al.*, 1986). This minimum results from mass accumulation in the droplet phase, hence, it is an indicator that particles larger than this Hoppel minimum have already been activated (*Hoppel et al.*, 1986) in the past and evaporated, again.

The NSDs observed inside clouds (blue lines), recorded during a 150 s long cloud passage in an altitude of $z_{\mathrm{baro}} = 1500\,\mathrm{m}$ (cloud passage at $t \approx 53300\,\mathrm{s}$ shown in Fig. 4.2), feature a monomodal distribution missing most of the accumulation mode particles, which are activated to cloud droplets. The integral over the difference between both curves (indicated by the shaded area in Fig. 4.3) represents the number of activated particles (N_{act}):

$$N_{\mathrm{act}} = \int_{D_{\mathrm{p,\,min}}}^{D_{\mathrm{p,\,max}}} \mathrm{NSD}_{\mathrm{inside}}(D_{\mathrm{p}}) - \int_{D_{\mathrm{p,\,min}}}^{D_{\mathrm{p,\,max}}} \mathrm{NSD}_{\mathrm{outside}}(D_{\mathrm{p}})\,. \tag{4.1}$$

In this case, N_{act} is calculated to $95 \pm 10\,\mathrm{cm}^{-3}$. This can be compared to the time series of N in Fig. 4.2. The difference of N outside ($N \approx 300\,\mathrm{cm}^{-3}$ at $t \approx 53200\,\mathrm{s}$) to N inside the cloud ($N \approx 200\,\mathrm{cm}^{-3}$ at $t \approx 53300\,\mathrm{s}$) calculates to $\Delta N \approx 100\,\mathrm{cm}^{-3}$, which agrees remarkable well with the derived N_{act}, indicating that the mobility and optical particle spectrometers provide a robust dataset to analyze total as well as interstitial particles. Furthermore, Fig. 4.3 shows

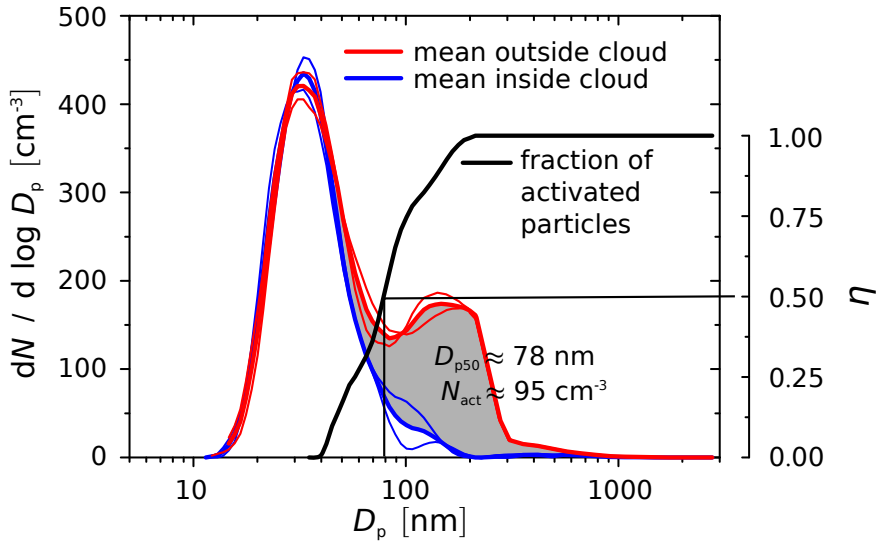

Figure 4.3: Left ordinate: particle number size distributions inside (blue lines) and outside (red lines) clouds. Right ordinate: fraction of activated particles (η). Shaded area represents the number of activated particles.

the fraction of activated particles (η, black line, right ordinate) defined as:

$$\eta(D_\mathrm{p}) = 1 - \frac{\mathrm{NSD}_\mathrm{inside}(D_\mathrm{p})}{\mathrm{NSD}_\mathrm{outside}(D_\mathrm{p})}\,. \tag{4.2}$$

The fraction of activated particles shows a steep increase for increasing diameters in a size range of 40 nm $< D_\mathrm{p} <$ 150 nm. For larger particles η advances unity. For $\eta = 0.5$ a 50% activation diameter ($D_{\mathrm{p}50}$) is defined, meaning that 50% of the particles with that diameter are activated. In the presented case study, the 50% activation diameter is calculated to $D_{\mathrm{p}50} \approx 78$ nm, which is close to the above mentioned Hoppel minimum. With the help of κ-Köhler theory (see Appendix A.1) the critical supersaturation necessary to activate a particle with a diameter of $D_\mathrm{p} = D_{\mathrm{p}50}$ can be calculated. ACTOS itself is not equipped with instruments to determine κ. Therefore, here the mean $\kappa = 0.7$ measured at Ragged Point is used, resulting in a critical supersaturation of $S_{crit} = 0.22\%$. These findings are comparable to those of (*Politovich*, 1988), who examined the variability of the quasi-steady supersaturation of cumulus clouds. The range of their observations is between 0.1% and 0.4%, depending on the degree of cloud dilution. Furthermore, *Hammer et al.* (2014) investigated the supersaturation in cumulus clouds at the high-altitude research station Jungfraujoch using a similar method as presented here. They found a slightly higher range of supersaturation values between 0.37% and 0.5%, which may result from lower particle hygroscopicity or higher updraft velocities due to the local topography at the Jungfraujoch. Entrainment and mixing lowers the number of activated particles, and hence, increase the activation diameter which can also

account for a lowering of the in this study derived supersaturation. Nevertheless, the above presented findings result from only one cloud. In Sec. 4.3.3 a statistical analysis of individual clouds is presented to evaluate the range of N_{act}, $D_{\mathrm{p,act}}$ and S_{crit} of measurements during 10 research flights.

4.2 Determination of the number concentration of activated particles

Motivated by the case study discussed above, where inside cloud and outside cloud measurements of the particle number size distribution together with observations of the total versus interstitial particle number concentration agree remarkable well, a systematic analysis of the number concentration of activated particles for each cloud is introduced.

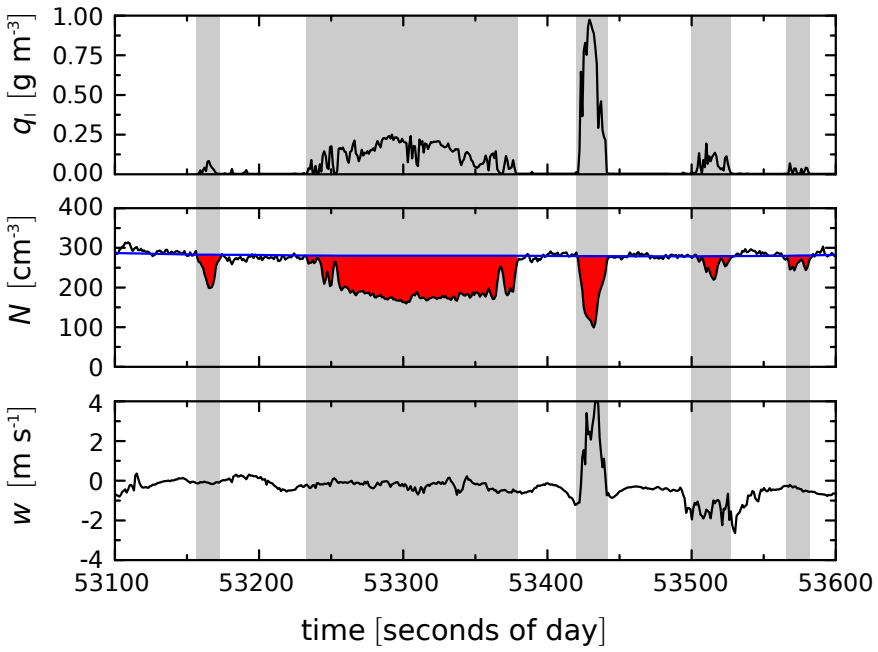

Figure 4.4: Time series of liquid water content (q_l), total particle number concentration (N, in case of clouds: interstitial particle number concentration) and vertical wind velocity (w) for a subsection of a horizontal leg at cloud altitude. The blue line indicates the running median of total particle number concentration outside the cloud. The difference between interstitial particle number concentration inside clouds and the running median of outside cloud conditions represents the number of activated particles (highlighted in red).

4.2.1 Methodology

Figure 4.4 shows the same subsection as shown before in the above case study (Fig. 4.2) to illustrate the methodology of deriving N_{act} from the time series of N. The grey shaded areas denote the clouds ACTOS penetrated, whereby, q_{l} in the uppermost panel is used to distinguish between clouds and the cloud-free environment. In principle, N_{act} is defined as the difference between the minimum particle number concentration inside one cloud and the running median of the outside cloud number concentration ($\overline{N}_{tot}$).
To calculate N_{act}, the original time series of all measured parameters is divided into cloudy and cloud-free subsections. Subsections are defined as cloudy subsections, when the one-second mean liquid water content fulfills $\overline{q}_{\mathrm{l,\,1\,s}} \geq 0.02\,\mathrm{g\,m^{-3}}$. This threshold is of technical character and should only ensure to exclude measurement artifacts resulting from noise.
Each subsection covers one complete cloud passage. The traversed cloud passages encompass measurements of cloud cores as well as cloud edges. Therefore, the interstitial particle number concentration varies inside one cloud and from cloud to cloud. In this analysis, the 10th percentile of the probability density function of the interstitial particle number concentration (pdf(N)) during one cloud passage is used as a measure for the minimum N_{int} inside the traversed cloud. The number concentration of activated particles for cloud number i is then calculated as follows:

$$N_{\mathrm{act,\,i}} = \overline{N}_{\mathrm{tot,\,i}} - N_{\mathrm{int,\,i}}. \tag{4.3}$$

With this method every cloud is related to one specific value of N_{act}.

4.2.2 Limitations

The application of the introduced method above is limited to cases, where vertical distribution of the particle properties is homogeneous. In cases with strong layering, the algorithm is not able to distinguish between dips in the time series of N resulting from activating particles to cloud droplets or resulting from measuring different air parcels with different aerosol properties.
Therefore, the cross-correlation function (CCF) for q_{l} and N is separately calculated for each research flight:

$$\mathrm{CCF}_{N,\,q_{\mathrm{l}}^*}(k) = \frac{\frac{1}{n-2k}\sum_{i=1+k}^{n-k}\left[(N(t_i)-\overline{N})(q_{\mathrm{l}}^*(t_{i+k})-\overline{q_{\mathrm{l}}^*})\right]}{\sqrt{\frac{1}{n}\sum_i^n (N(t_i)-\overline{N})^2 \cdot \frac{1}{n}\sum_i^n (q_{\mathrm{l}}^*(t_i)-\overline{q_{\mathrm{l}}^*})^2}}\,, \tag{4.4}$$

where i is the index of summation, n is the total number of samples and k denotes the shift of the time series of N and $q_{\mathrm{l}}^* = -q_{\mathrm{l}}$ (producing a positive peak in the CCF). The liquid water content q_{l} and N should be anti-correlated if the dips in N are caused by the

presence of clouds, resulting in a distinct peak in the CCF. Furthermore, the CCF is used to correct for the time shift in N compared to q_l resulting from the response time and inlet pipe of the CPC (cf. Sec. 4.2.3), as well as the spatial displacement of the aerosol inlet and the PVM. Figure 4.5 shows the $\mathrm{CCF}_{\mathrm{N},\,\mathrm{q_l^*}}(\mathrm{k})$ calculated from Eq. 4.4 at a measurement frequency of 100 Hz for time lags (k) between 0 and 600, corresponding to 0 to 6 s for two different research flights (#06, #29). The CCF in Fig. 4.5(a) shows a clear maximum at $k \approx 480$, indicating that N and q_l are clearly anti-correlated and shifted in time by about 4.8 s. Instead, in Fig. 4.5(b) the CCF does not show a clear maximum. Therefore, research flight #23 is excluded from the statistical analysis in this work. For all flights included in this analysis, the time shift between N and q_l is calculated and corrected separately. In total for 10 of 31 research flights, the calculated CCF features a clear maximum.

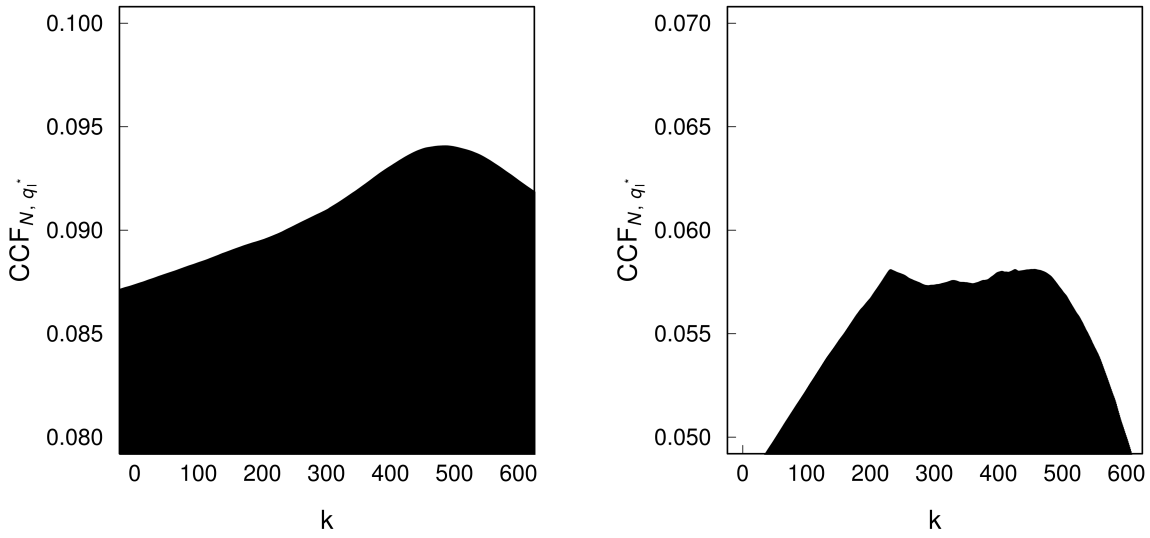

(a) research flight #06, Nov. 15th, 2010

(b) research flight #23, April 23th, 2011

Figure 4.5: Cross correlation function (CCF) of q_l^* and N for 100 Hz measurement frequency.

4.2.3 Activated particles vs. cloud droplet number concentration

ACTOS offers the great opportunity to compare the derived number concentration of activated particles with measured cloud droplet number concentrations. As introduced in Sec. 2.3.1, a cloud droplet size spectrometer was operated during both measurement campaigns providing information on the droplet size and velocity. Furthermore, cloud droplet number concentration can be calculated. This subsection deals with a comparison of the derived concentration of activated particles and the observed cloud droplet number concentration (N_d). Due to technical reasons, a comparison is only possible for five research flights

(#07, #10, #11, #12, #14). A comparison of N_{act} and N_d requires a close and individual look at both quantities at first.

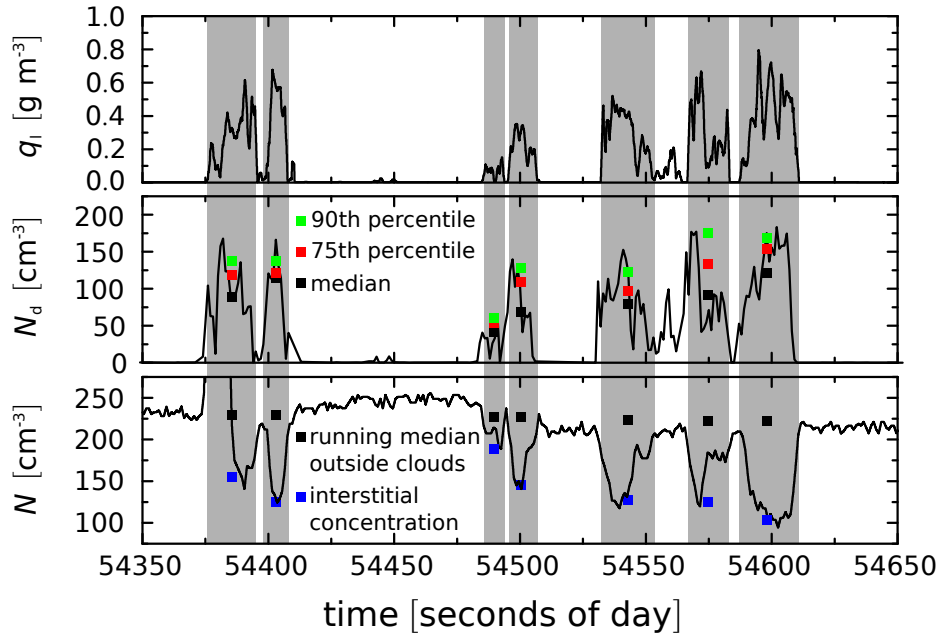

Figure 4.6: Time series of q_l, cloud droplet number concentration (N_d) and particle number concentration (N, in cases of clouds only interstitial particles are measured) for a selected subsection at cloud level during research flight #11. Clouds are indicated by q_l and shaded in grey. Green, red and black squares in the mid panel denote the 90th, 75th percentile and median values of N_d within one cloud. Black and blue squares in the lowermost panel show the running average of outside cloud conditions (N_{tot}) and the 10th percentile of N inside each cloud (N_{int}), respectively.

Figure 4.6 shows q_l, N_d and N for different observed clouds during research flight #11 (see Tab. C.1). The shaded areas mark the times when ACTOS penetrated clouds. Both q_l and N_d show a higher variability compared to the time series of N. The reason for this behavior lies in the different time resolution and response times of the instruments. The CPC measures N with 1 s time resolution, however, the response time on the order of 1–2 s causes a smoothing of the time series.

In contrast, for q_l and N_d 1 s-mean values are calculated. The original measurement frequency of the liquid water content measurements is 100 Hz. The droplet number concentration is calculated from the time series of instantaneously recorded droplets, both without any response time effects.

Generally, N_{int} and N_d show an anti-correlation. In order to compare N_{act} and N_d statistical quantities are separately calculated for each cloud. The mid panel of Fig. 4.6 shows the median, 75th percentile and 90th percentile (black, red and green square) of N_d during each

cloud passage. The lowermost panel shows N_{int} (blue squares) and the running median of N_{tot} outside clouds. As introduced above, the difference between both defines the number of activated particles.

Figure 4.7 shows boxplots of the observed median (Fig. 4.7(a)), 75th percentile (Fig. 4.7(b)) and 90th percentile (Fig. 4.7(c)) of N_{d} versus the derived N_{act} for the 5 research flights, during which both, the cloud droplet spectrometer and the CPC were running (research flights #07, #10, #11, #12, #14). In total, 265 clouds are analyzed. The results are binned in classes of $20\,\mathrm{cm}^{-3}$. Boxes show the first and third quartile and the median (horizontal line). The error bars represent 75% of the data points. The black straight line denotes the 1:1 line, the red dashed lines indicate a deviation of $\pm\,20\%$. The upper x-axis shows the number of samples for each bin.

In Fig 4.7(a) the median values of N_{d} lie below the 1:1 line, indicating a systematic deviation of the median N_{d} towards lower values compared to N_{act}. The 75th percentile in Fig. 4.7(b) shows a reasonable good agreement up to $N_{\mathrm{act}} < 180\,\mathrm{cm}^{-3}$. The deviation for larger concentrations may result from bad statistics (only 8% of all samples within this comparison feature a concentration of $N_{\mathrm{act}} > 180\,\mathrm{cm}^{-3}$) or a decrease in N_{d} caused by coagulation.

Since N_{act} is calculated with the help of the 10th percentile of N (see Eq. 4.3), it should agree best with the 90th percentile of N_{d}. In fact, the agreement is worse for the 90th percentile of N_{d} plotted in Fig. 4.7(c). The median values for the 90th percentile of N_{d} is shifted towards higher values overestimating the number of activated particles. As already mentioned above, this is probably resulting from the higher measurement resolution of N_{d}, followed by a finer detection of the maximum cloud droplet number concentration in a cloud core.

Nevertheless, here, two completely different measurement approaches to derive the number of activated particles on the one hand and the cloud droplet number concentration on the other hand are compared. The reasonably good agreement shown above encourages the use of N_{act} for further statistical analysis and to interpret this as a suitable measure for the cloud droplet number concentration.

For technical reasons, cloud droplet number concentration data are unfortunately not available for the first half of $\mathrm{CARRIBA}_{\mathrm{wet}}$ and throughout the whole $\mathrm{CARRIBA}_{\mathrm{dry}}$ campaign. Therefore, N_{act} is used instead of N_{d} in the context of an aerosol-cloud interaction study which enlarges the statistics and the bandwidth of observed particle number concentration values.

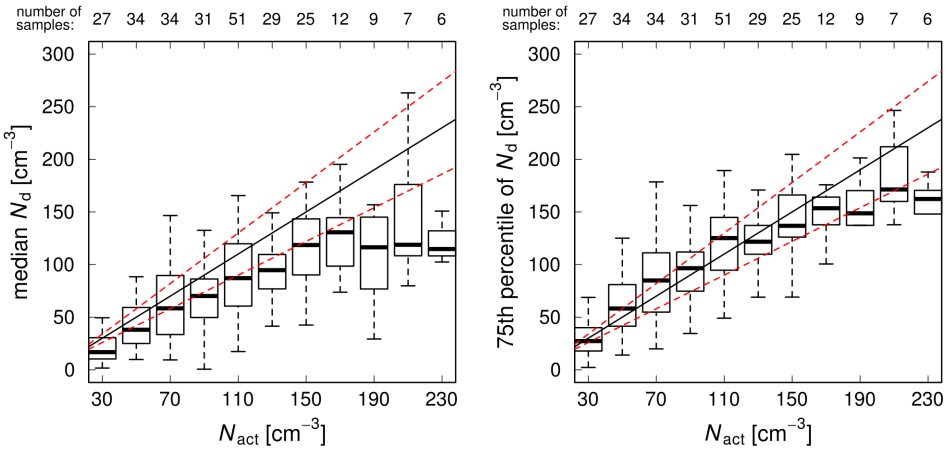

(a) Median of N_d vs. N_{act}.

(b) 75th percentile of N_d vs. N_{act}.

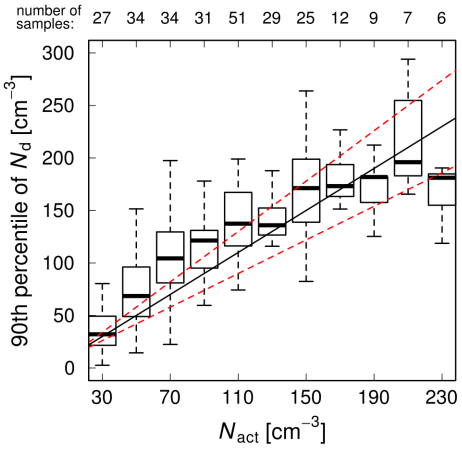

(c) 90th percentile of N_d vs. N_{act}.

Figure 4.7: Boxplot of observed median, 75th percentile and 90th percentile cloud droplet number concentration (N_d) vs. derived activated particles (N_{act}). Black straight lines represent the 1:1 line and red lines denote $\pm 20\%$. The upper x-axis shows the number of samples for each bin.

4.3 Cloud statistics

The above introduced method is applicable to 10 research flights, 8 flights during the campaign in November 2010 and 2 flights in April 2011. All together, 687 clouds are selected and analyzed covering total particle number concentrations between 200 cm^{-3} and 700 cm^{-3} and concentrations of activated particles up to 400 cm^{-3}. The main topic of this work are aerosol-cloud interactions focusing on the cloud droplet number concentration during the activation process. Therefore, the focus is on young and actively growing clouds. The following section introduces filter criteria to sort for the most active clouds. Afterwards, results of one research flight are presented, followed by a statistical analysis of the measurements during 10 research flights.

4.3.1 Filters to sort for most active clouds

One major characteristic of clouds in the trade wind regime is their short lifetime. Already *Langmuir* (1948) recognized that those clouds often develop rain within less than 30 minutes. Therefore, during one single research flight, ACTOS observed actively growing as well as mature and decaying clouds directly next to each other.

Here, filter criteria are introduced with the goal to extract the 30% most active clouds. Please note, that for the above shown comparison between N_{act} and N_d the evolution stage of the cumulus clouds is not of importance, therefore, no filters have been applied.

Technical filters

Technical filters are applied to account for measurement uncertainties. As mentioned above the CPC measuring N has a response time on the order of 1–2 seconds. Hence, cloud passages shorter than 2 s are neglected. Additionally, the measurement uncertainty of the CPC is on the order of 10%. Therefore, all cloud passages are rejected where $N_{act}/N < 0.1$.

Filter for decaying clouds

Decaying clouds feature different microphysical properties compared to those, which are just developing. One property of a decaying cloud is that large areas are characterized by downdrafts. Here, the 90th percentile of the vertical wind velocity (w_{90}) inside a cloud is used as a measure for the peak wind velocity. For further statistical analysis only clouds are used fulfilling $w_{90} \geq 0.8\,m\,s^{-1}$.

Filter for cloud cores

To distinguish between cloud cores and diluted cloud parcels the liquid water content (q_l) is used. Therefore, the 95th percentile of q_l is calculated for height bins of 100 m ($q_{\mathrm{l},\,95\%}(z)$) and used to normalize all single measurements according to their altitude (z) in the following way: $q_\mathrm{l,norm}(z) = \frac{q_\mathrm{l}(z)}{q_{\mathrm{l},\,95\%}(z)}$ (see Appendix D for a detailed description of the determination of $q_{\mathrm{l},\,95\%}(z)$). To exclude diluted cloud parts only those measurements are taken into account which feature $q_\mathrm{l,norm} > 0.4$.

Table 4.1: Summary of filter criteria and the corresponding passing rate of the clouds.

Filter	Criterion	Passing rate
technical filters	$\Delta t > 2\,\mathrm{s}$	68%
	$N_\mathrm{act}/N > 0.1$	80%
cloud core filter	$q_{\mathrm{l},\,\mathrm{norm}} > 0.4$	46%
updraft filter	$w_{90} > 0.8\,\mathrm{m\,s^{-1}}$	39%
total passing rate		30%

Table 4.1 summarizes all applied filters and the passing rates for all 687 individual clouds. In Appendix E a contour plot of the passing rates for different filter criteria is shown underlining the close relationship between $q_{\mathrm{l},\,\mathrm{norm}}$ and w_{90} filters.

4.3.2 Results for one Research flight

In this section, exemplarily, the results of research flight #07 are presented without and with applying the above introduced filters. Figure 4.8 shows the derived N_act over the 90th percentile of the vertical wind velocity (w_{90}) for research flight #07. The 90th percentile of w is chosen to be a characteristic value for the peak upwind inside the cloud core region.
The observations show a wide spread covering already descending clouds ($w_{90} < 0\,\mathrm{m\,s^{-1}}$), clouds with moderate upwinds and very active clouds with a vertical wind velocity up to $w_{90} \approx 4.5\,\mathrm{m\,s^{-1}}$.
The colors of the circles indicate if clouds are passing the applied filters. Black circles show clouds not fulfilling the criteria of the technical filters. These clouds feature a horizontal extension less than 40 m (corresponding to $\Delta t = 2\,\mathrm{s}$, at a true air speed of $20\,\mathrm{m\,s^{-1}}$) or a number concentration of activated particles less than 10% of the outside cloud total particle number concentration ($N_\mathrm{act}/N < 0.1$).
Blue circles belong to clouds passing the technical filters, but do not pass the filters for decaying clouds and cloud cores. Green circles pass all filters, and are therefore, in the main

focus of further investigations.

The red line indicates results of the cloud microphysical parcel model by *Simmel and Wurzler* (2006). The parcel model is described in Sec. 2.5. In this context

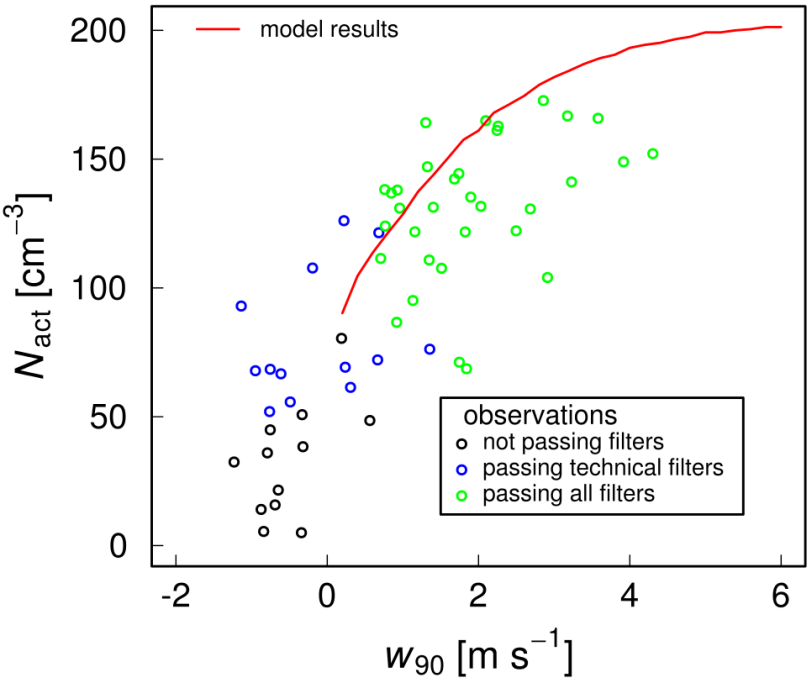

Figure 4.8: Number of activated particles (N_{act}, circles) versus 90th percentile of vertical wind velocity (w_{90}) for research flight #07. Black circles denote clouds not passing the filter criteria. Blue and green circles represent clouds passing technical and all filters, respectively. Red line indicates results of the cloud microphysical parcel model.

the model is used to give information on the adiabatic cloud droplet number concentration (CDNC). The model was initialized with pressure, temperature and humidity as well as the particle number size distributions measured in the well-mixed layer during research flight #07 and a bulk hygroscopicity parameter (κ) derived from ground measurements (as described in Sec. 3.2). Details are given in Tab. 4.2. Adiabatic CDNC is modeled by driving the box model with a fixed updraft up to an altitude above cloud base at which CDNC is constant. Since the focus of this investigation is on the activation process, collision/coalescence and entrainment are not taken into account. Here, adiabatic CDNC is only used to compare to our observations of N_{act}.

For research flight #07, the modeled CDNC shows a steep increase for upwind velocities up to 2 m s^{-1} followed by a weak increase for higher wind speeds resulting from the shape of the measured aerosol NSDs.

Overall, the observed clouds feature a wide spread in N_{act} up to 170 cm^{-3}. The observations

Table 4.2: Initial parameters for cloud microphysical parcel model.

Quantity		initial value
altitude	z	250 m asl
atmospheric pressure	p	979.5 hPa
air temperature	T	299.3 K
specific humidity	q	18.4 g kg^{-1}
hygroscopicity parameter	κ	0.7

of N_{act} for clouds, which do not pass the technical filters range within 0 cm^{-3} and 80 cm^{-3}. Instead, the clouds which pass the technical filters but do not pass the filters for the most active clouds (blue circles) range within 50 cm^{-3} and 130 cm^{-3}. The observed clouds passing all filters (green circles) show values within 50 cm^{-3} and 170 cm^{-3} and a weak increase for increasing w_{90}. The model results for the adiabatic CDNC seem to serve as an upper limit for N_{act}. The highest N_{act} values are observed for wind speeds in the range of 1.5 to 4 m s^{-1}. The large range of N_{act} even for the most active clouds may result from entrainment and mixing of dry air, leading to partial evaporation of cloud droplets and lowering of N_{act}. In cases where N_{act} is larger than the modeled CDNC, the observed cloud probably experienced a higher vertical wind velocity during its formation than at the time ACTOS penetrated the cloud.

The following analysis is based on the most active clouds passing all filter criteria.

With the help of N_{act}, it is possible to derive the activation diameter ($D_{\mathrm{p,\,act}}$) using the particle number size distribution (NSD). Therefore, for each research flight a set of NSDs representative for the marine boundary layer (MBL) and the vicinity of clouds are selected from the whole dataset. Hereinafter, these NSDs are called master-NSDs.

The master-NSDs are selected under consideration of the following criteria:

- NSDs measured under cloud-free conditions during horizontal flight legs in MBL or cloud level
- $\int_{D_{\mathrm{p,\,min}}}^{D_{\mathrm{p,\,max}}} \mathrm{NSD}(D_{\mathrm{p}})$ matches total number concentration outside of clouds within $\pm\,10\%$.

$D_{\mathrm{p,\,act}}$ is then obtained from N_{act} and the master-NSDs ($\mathrm{NSD}(D_{\mathrm{p}})$) such that

$$N_{\mathrm{act}} = \int_{D_{\mathrm{p}}=D_{\mathrm{p,\,act}}}^{D_{\mathrm{p}}=D_{\mathrm{p,\,max}}} \mathrm{NSD}(D_{\mathrm{p}})\,\mathrm{d}D_{\mathrm{p}}\,. \tag{4.5}$$

Using a set of master-NSDs produces a set of $D_{\mathrm{p,\,act}}$ representing the variability of the aerosol conditions within the considered area. This variability is used as a measure for the uncertainty concerning further calculations.

As mentioned above, the critical supersaturation necessary to activate aerosol particles with $D_{\mathrm{p}} = D_{\mathrm{p,\,act}}$ can be derived with the help of κ-Köhler theory (see Appendix A.1). Again, ACTOS itself is not equipped with instruments to determine κ, therefore, the following results are calculated using the mean $\kappa = 0.7$ derived from ground-based measurements at Ragged Point.

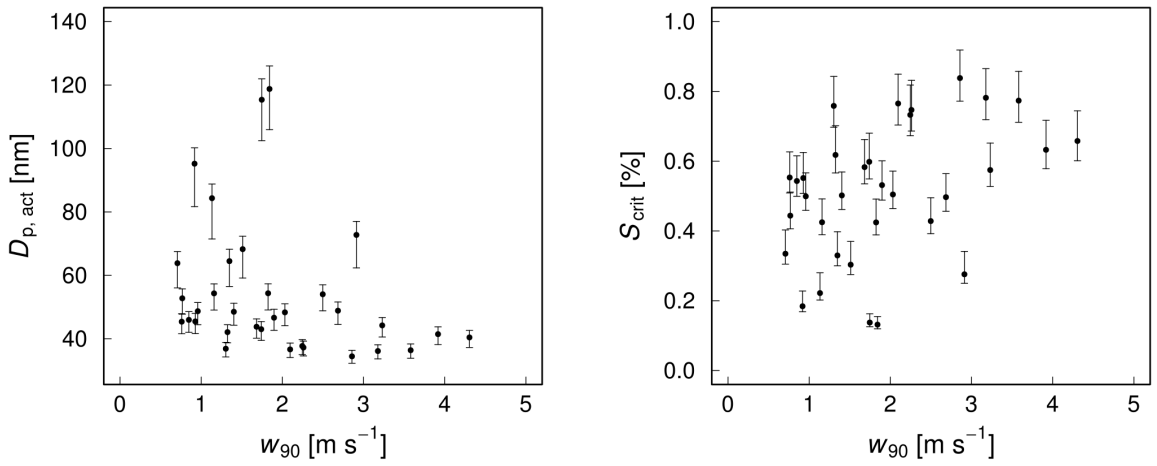

(a) $D_{\mathrm{p,\,act}}$ vs. w_{90}

(b) S_{crit} vs. w_{90}

Figure 4.9: Activation diameter $D_{\mathrm{p,\,act}}$ and critical supersaturation S_{crit} derived from N_{act} with the help of Eq. 4.5 and Eq. A.6 for research flight #07. Observations of 30% most active clouds are shown. The error bars result from calculations using a set of master-NSDs and represent the aerosol variability.

Figure 4.9 shows the activation diameter $D_{\mathrm{p,\,act}}$ (Fig. 4.9(a)) and critical supersaturation S_{crit} (Fig. 4.9(b)) of the most active clouds derived from N_{act} with the help of Eq. 4.5 and Eq. A.6, respectively. According to the large spread in N_{act} also $D_{\mathrm{p,\,act}}$ and S_{crit} show a large spread. The error bars result from the calculation of $D_{\mathrm{p,\,act}}$ and S_{crit} using a set of master-NSDs and represent the aerosol variability.

The smallest observed activation diameter are on the order of $D_{\mathrm{p,\,act}} \approx 40\,\mathrm{nm}$ requiring a critical supersaturation of $S_{\mathrm{crit}} \approx 0.8\%$. These extreme values occur over the whole wind range of $1.5 < w_{90} < 4.5\,\mathrm{m\,s^{-1}}$, while the range of observed $D_{\mathrm{p,\,act}}$ and S_{crit} narrows for high vertical wind velocities. Finally, these data show a clear trend towards small $D_{\mathrm{p,\,act}}$ and high S_{crit} for the largest observed vertical wind velocities.

It is obvious, that only observations of N_{act} close to the adiabatic CDNC give reliable information on $D_{\mathrm{p,\,act}}$ and S_{crit} during the formation process of the respective cloud. As already mentioned, there are even for the most active clouds observations which deviate from the model calculations of the adiabatic CDNC (cf. Fig. 4.8). The larger this deviation, the

probably less meaningful is the derived $D_{\mathrm{p,\,act}}$ and S_{crit} for the conditions during the activation process. Nevertheless, the here derived information on N_{act}, $D_{\mathrm{p,\,act}}$ and S_{crit} cover a wide spectrum of observations of fast developing cumulus clouds. Most probably the observations with the highest N_{act} (lowest $D_{\mathrm{p,\,act}}$ and highest S_{crit}) give the best estimate of the cloud properties of freshly formed cumuli.

4.3.3 Results of all Research flights

In this section, results of all flights are presented, for which the in Sec. 4.2.1 introduced method to derive N_{act} is applicable. Table 4.3 contains details of all flights used for this analysis including the flight number, date, observed aerosol type and shape of the used master-NDSs as well as median particle number concentration outside of clouds ($\overline{N}$), median (flight-averaged) CCN concentration at 0.26% supersaturation measured in the well-mixed marine boundary layer ($\overline{N}_{\mathrm{CCN,\,0.26\%}}$), and the hygroscopicity parameter κ derived from ground measurements (see Sec. 3.2). Since the daily variability in κ is comparable to its day to day variability during the two campaigns, the campaign average of $\kappa = 0.7$ is used for the calculation of S_{crit} of all research flights except #21, where κ is lowered during the advection of an African particle plume (cf. Fig. 3.2).

Table 4.3: Details of all flights used for the statistical analysis of this work.

Flight No.	date [yyyy-mm-dd]	aerosol type	shape of NSD	$\overline{N}$ [cm^{-3}]	$\overline{N}_{\mathrm{CCN,\,0.26\%}}$ [cm^{-3}]	κ
#05	2010-11-14	marine	bimodal	231 ± 24	142 ± 30	0.7
#06	2010-11-15	marine	bimodal	281 ± 28	140 ± 28	0.7
#07	2010-11-16	marine	bimodal	250 ± 22	110 ± 27	0.7
#10	2010-11-21	marine	bimodal	400 ± 60	149 ± 36	0.7
#11	2010-11-22	marine	bimodal	273 ± 27	138 ± 36	0.7
#12	2010-11-23	marine	bimodal	346 ± 26	144 ± 37	0.7
#14	2010-11-25	marine	bimodal	427 ± 26	280 ± 49	0.7
#15	2010-11-26	marine	bimodal	413 ± 76	302 ± 51	0.7
#18	2011-04-10	marine	bimodal	300 ± 37	120 ± 33	0.7
#21	2011-04-14	Afr. mix	monomodal	477 ± 48	403 ± 64	0.6

Figure 4.10 shows histograms of w_{90}, N_{act}, $D_{\mathrm{p,\,act}}$ and S_{crit} for the 30% most active clouds. Mean and median values as well as standard deviation and interquartile spread are listed in Tab. 4.4.

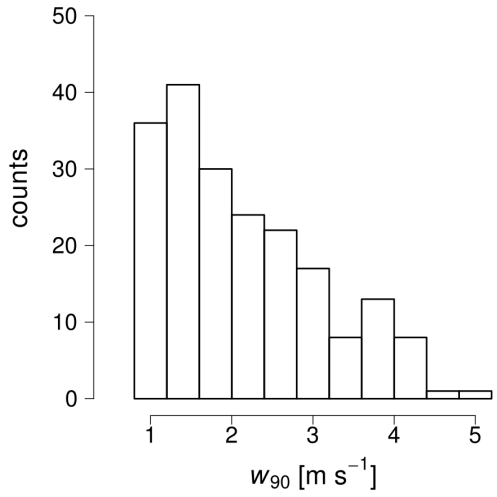

(a) Histogram of w_{90}.

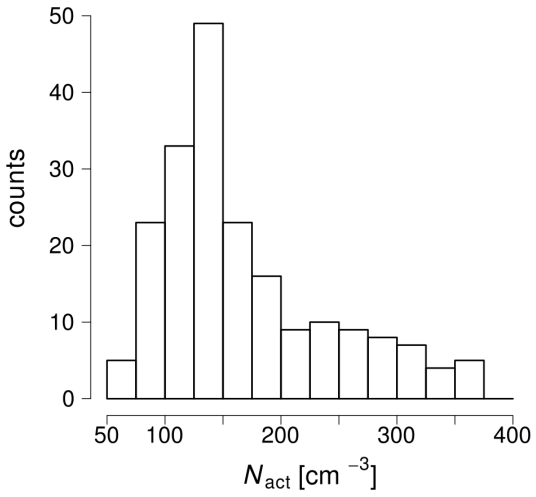

(b) Histogram of N_{act}.

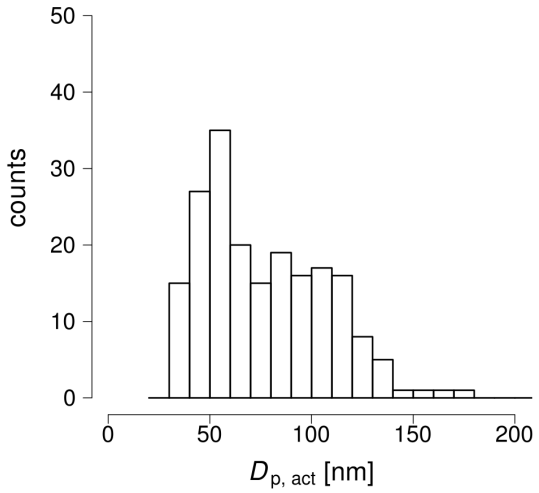

(c) Histogram of $D_{\mathrm{p,\,act}}$.

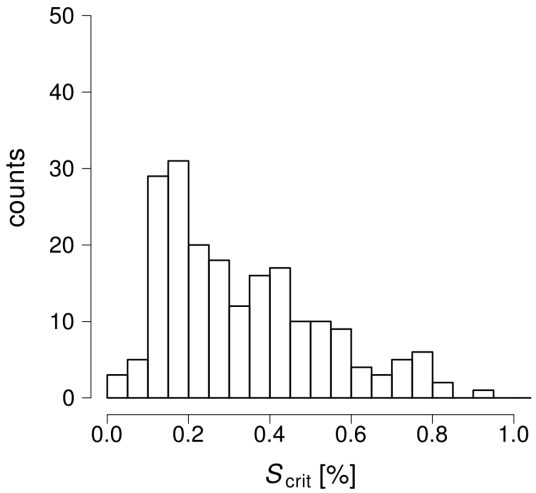

(d) Histogram of S_{crit}.

Figure 4.10: Histograms of 90th percentile of vertical wind velocity (w_{90}), number of activated particles (N_{act}), derived activation diameter ($D_{\mathrm{p,\,act}}$) and derived critical supersaturation (S_{crit}). The histograms cover 210 clouds (30% most active ones) from 10 research flights (8 during November 2010 and 2 during April 2011).

The histogram of w_{90} shows a broad distribution with the majority of observed vertical wind velocities below $2\,\mathrm{m\,s^{-1}}$. The largest observed vertical wind velocities are on the order of $5\,\mathrm{m\,s^{-1}}$, while the mean value is $2.1 \pm 0.98\,\mathrm{m\,s^{-1}}$.
The number of activated particles features also a broad distribution with a clear maximum at approximately $N_{\mathrm{act}} \approx 130\,\mathrm{cm^{-3}}$. Its range is between 50 and $370\,\mathrm{cm^{-3}}$ with a mean concentration of $N_{\mathrm{act}} = 170 \pm 72\,\mathrm{cm^{-3}}$. In general, the droplet number concentration of maritime clouds is expected to be on the order of a few hundred per cubic centimeter. During the RICO experiment ("Rain in shallow cumulus over the Ocean", *Rauber et al.*, 2007) they found average droplet number concentrations between $50\,\mathrm{cm^{-3}}$ and $200\,\mathrm{cm^{-3}}$ (*Colón-Robles et al.*, 2006; *Hudson and Mishra*, 2007), which agrees with the here presented N_{act} values.

Table 4.4: Statistics of vertical wind velocity w_{90}, number concentration of activated particles N_{act}, activation diameter $D_{\mathrm{p,\,act}}$ and critical supersaturation S_{crit}.

	w_{90} [$\mathrm{m\,s^{-1}}$]	N_{act} [$\mathrm{cm^{-3}}$]	$D_{\mathrm{p,\,act}}$ [nm]	S_{crit} [%]
mean ± standard deviation	2.1 ± 0.98	170 ± 72	81 ± 41	0.33 ± 0.19
median ± interquartile spread	1.9 ± 1.35	146 ± 86	72 ± 49	0.28 ± 0.27

The histogram of the derived activation diameter shows one distinct maximum at $D_{\mathrm{p,\,act}} \approx 55\,\mathrm{nm}$ and a plateau between $D_{\mathrm{p,\,act}} \approx 60\,\mathrm{nm}$ and $D_{\mathrm{p,\,act}} \approx 120\,\mathrm{nm}$. The lowest $D_{\mathrm{p,\,act}}$ are on the order of 40 nm, which is well below the Hoppel minimum. Only a few clouds feature activation diameters larger than 120 nm. The mean activation diameter is close to the Hoppel minimum at $D_{\mathrm{p,act}} = 81 \pm 41\,\mathrm{nm}$.
Calculated S_{crit} values range between 0.03 and 0.9% supersaturation. The distribution shows a maximum close to 0.2% and a broad tail towards higher supersaturations. The mean critical supersaturation calculated from the 30% most active clouds is $0.33 \pm 0.19\%$. Different studies to examine the supersaturation inside clouds show similar results with a smaller bandwidth of observations. As already mentioned earlier, *Politovich* (1988) examined the variability of the quasi-steady supersaturation of cumulus clouds and found supersaturations between 0.1% and 0.4%. Furthermore, *Hammer et al.* (2014) calculated supersaturation values ranging within 0.37% and 0.5% cumulus clouds at the high-altitude research station Jungfraujoch using a similar method as presented here. *Mason* (1971) expect the supersaturation inside maritime clouds to be within 0.3% and 0.8%, which is very close to the derived values here. The broad tail towards higher supersaturation values suggests that locally very high supersaturation values can be observed. One reason for locally high supersaturation could be vortex spin-out of droplets *Shaw et al.* (1998).

4.4 What controls the cloud droplet number concentration?

One of the main questions driving the analysis of aerosol-cloud interactions in this work is: What controls the cloud droplet number concentration? In the above introduced analysis the number of activated particles is derived and validated against the measured cloud droplet number concentration. Furthermore, filters have been defined to sort for the 30% most active clouds. In the following section major factors affecting N_{act} of the 30% most active clouds will be identified.

4.4.1 Meteorology

In Chapter 3.2, the general meteorological situation during the two measurement campaigns is described reflecting that conditions in the marine boundary layer showed only marginal variation. Here, the focus is on the dynamics namely the distribution of w_{90} for different research flights.

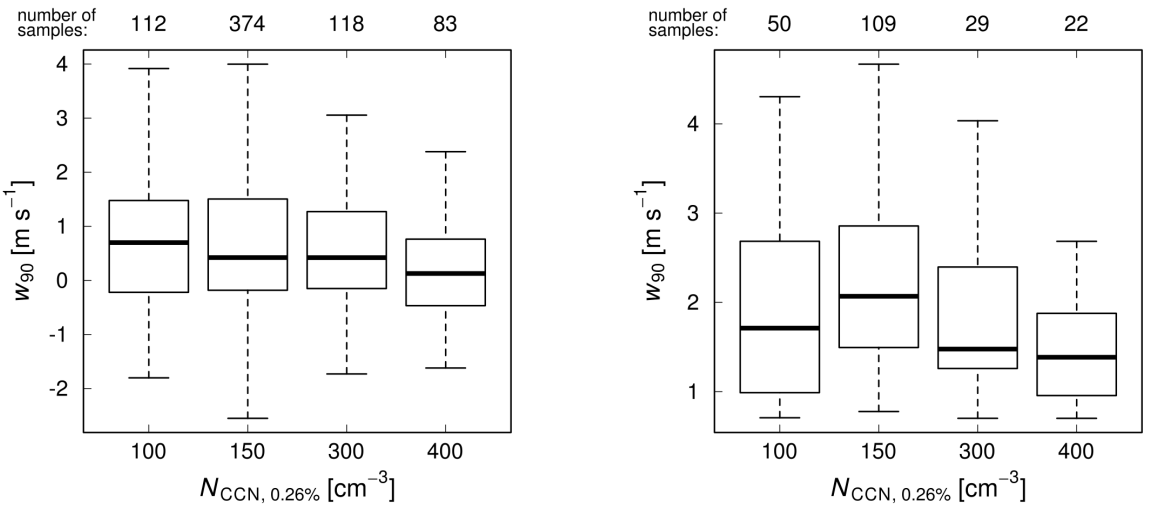

(a) without filters

(b) 30% most active clouds

Figure 4.11: Boxplots of 90th percentile of vertical wind velocity w_{90} versus the median (flight-averaged) CCN number concentration at 0.26% supersaturation ($\overline{N}_{\mathrm{CCN,\,0.26\%}}$) measured in the well-mixed marine boundary layer.

Figure 4.11 shows boxplots of 90th percentile of vertical wind velocity w_{90} versus $\overline{N}_{\mathrm{CCN,\,0.26\%}}$ for the unfiltered dataset and for the 30% most active clouds. In Fig. 4.11(a) the median w_{90} does not show a clear trend for different CCN concentrations. Nevertheless, for $\overline{N}_{\mathrm{CCN,\,0.26\%}} > 300\,\mathrm{cm}^{-3}$ less observations feature wind velocities larger than $3\,\mathrm{m\,s}^{-1}$. This behavior is more

pronounced in Fig. 4.11(b). Here, the median w_{90} slightly decreases for $\overline{N}_{\mathrm{CCN,\,0.26\%}} > 300\,\mathrm{cm^{-3}}$.

4.4.2 Aerosol effect vs. updraft velocity

As shown above, the median vertical wind velocity is not significant different for the different CCN number concentrations. Therefore, the influence of vertical wind velocity and CCN number concentration on the number of activated particles is separately investigated, now. The following analysis is focused on freshly formed cumulus clouds. Only clouds passing the filter criteria for the 30% most active clouds are thus taken into account.

Figure 4.12 shows boxplots of N_{act} vs. w_{90} and N_{act} versus $\overline{N}_{\mathrm{CCN,\,0.26\%}}$. The data are sorted into bins of $1\,\mathrm{m\,s^{-1}}$ and $50\,\mathrm{cm^{-3}}$, respectively. The secondary x-axis shows the number of samples in each bin.

The boxplot in Fig. 4.12(a) shows a pronounced increase of the median values (horizontal lines inside boxes) of N_{act} for increasing w_{90} up to $2.5\,\mathrm{m\,s^{-1}}$. Above, the median N_{act} levels out at about $150\,\mathrm{cm^{-3}}$ and features a strong scatter. Additionally, the median values of all observations for $w_{90} > 1\,\mathrm{m\,s^{-1}}$ only slightly exceed the mid 75th percentile (indicated by the upper horizontal border of the box) of the observations for $w_{90} < 1\,\mathrm{m\,s^{-1}}$, indicating a weak correlation.

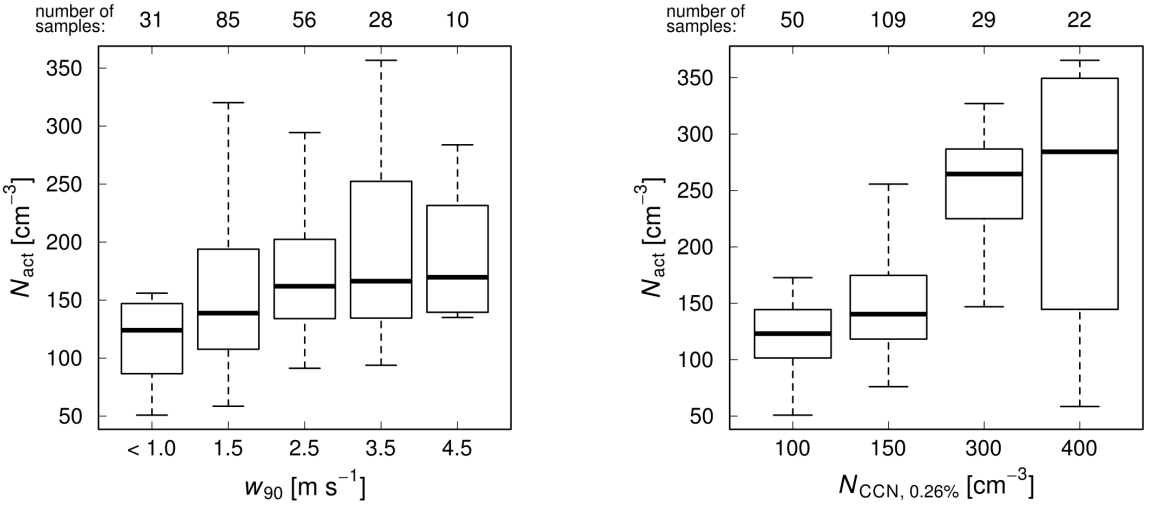

(a) Boxplot of N_{act} vs. w_{90}.

(b) Boxplot of N_{act} vs. CCN in well-mixed MBL.

Figure 4.12: Boxplots of activated particles (N_{act}) vs. 90th percentile of w (w_{90}) and N_{act} vs. $\overline{N}_{\mathrm{CCN,\,0.26\%}}$.

Instead, the boxplot in Fig. 4.12(b) shows a more pronounced relationship for N_{act} against

$N_{\mathrm{CCN},\,0.26\%}$. The median values feature a clear trend towards higher numbers of activated particles in cases of increased CCN number concentration. Beside the scatter, the largest median values observed for $N_{\mathrm{CCN},\,0.26\%} \approx 400\,\mathrm{cm}^{-3}$ is even larger than the upper whiskers of the two smallest categories pointing towards a strong influence of CCN on the number of activated particles.

The reason in the rather weak correlation in Fig. 4.12(a) is due to the superposition of both influences: vertical wind velocity and different amount of available CCN. The same plot again but grouped for different CCN loadings is presented in Fig. 4.13. There, boxplots of N_{act} against w_{90} are shown for different CCN concentrations: (a) $N_{\mathrm{CCN},\,0.26\%} < 250\,\mathrm{cm}^{-3}$ and (b) $N_{\mathrm{CCN},\,0.26\%} > 250\,\mathrm{cm}^{-3}$. These boxplots unmask the influence of the vertical wind velocity and reveal similar observations as already shown for a single flight in Fig. 4.8.

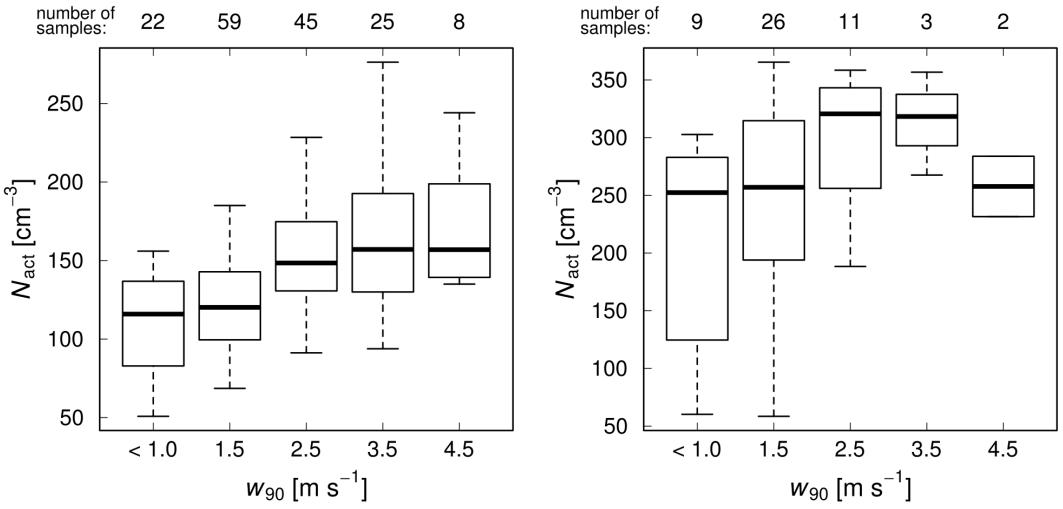

(a) $N_{\mathrm{CCN},\,0.26\%} < 250\,\mathrm{cm}^{-3}$ (b) $N_{\mathrm{CCN},\,0.26\%} > 250\,\mathrm{cm}^{-3}$

Figure 4.13: Boxplots of activated particles (N_{act}) vs. 90th percentile of the vertical wind velocity w_{90} for different $N_{\mathrm{CCN},\,0.26\%}$.

Figures 4.13 and 4.12 underline the importance of both: vertical wind velocity and the amount of available CCN. Considering on the one hand only observations of N_{act} with similar CCN number concentration, the influence of w_{90} is strong. On the other hand, N_{act} is strongly limited by the amount of available particles, which are able to nucleate droplets.

The following paragraph addresses the question whether N_{act} is more sensitive towards changes in w_{90} or towards changes in the total particle number concentration.

Figure 4.14 shows a contour plot of the observed median N_{act} of the 30% most active clouds calculated for pairs of observed w_{90} and N. Considering a fixed total number concentration

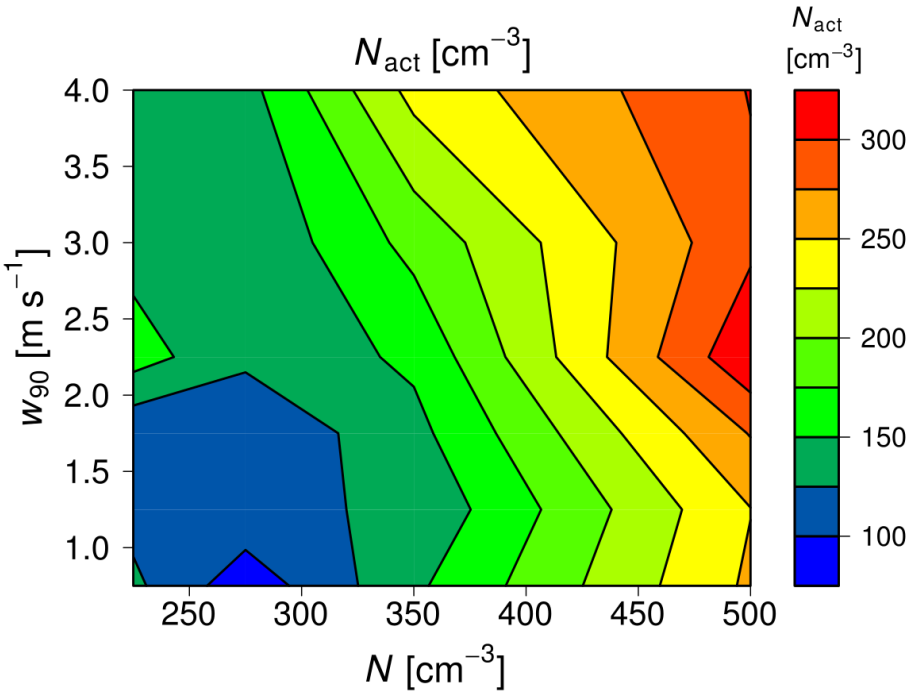

Figure 4.14: Median observed N_{act} of the 30% most active clouds calculated for pairs of observed w_{90} and N.

(e.g., $N = 350\,\mathrm{cm}^{-3}$) N_{act} varies only between 125 and 225 cm^{-3} over the whole range of vertical wind velocities. Instead, considering a fixed vertical wind velocity (e.g., $2.5\,\mathrm{m\,s}^{-3}$) N_{act} varies between 125 and 300 cm^{-3}. Hence, the rather vertical instead of horizontal orientation of the isolines indicates that the observed concentration of activated particles is more sensitive to changes in the aerosol particle number concentration than to changes in the updraft velocity.

4.4.3 Aerosol-Cloud Interaction Metric

In Fig. 4.14 the sensitivity of N_{act} towards changes in w_{90} and N is analyzed qualitatively. *Feingold and Remer* (2001) proposed following approach to quantify the influence of aerosols particle number concentration on clouds with an aerosol-cloud interaction metric:

$$\mathrm{ACI_N} = \left.\frac{\delta \ln(N_{act})}{\delta \ln(N)}\right|_{q_l}. \tag{4.6}$$

$\mathrm{ACI_N}$ is determined by plotting both N_{act} and N on a logarithmic scale and applying a linear fit. The slope of the fit curve is understood to be $\mathrm{ACI_N}$. Figure 4.15 shows $\ln(N_{act})$ versus

$\ln(N)$ for the 30% most active clouds grouped for four different liquid water contents. The slope of the linear fit represents $\mathrm{ACI_N}$.

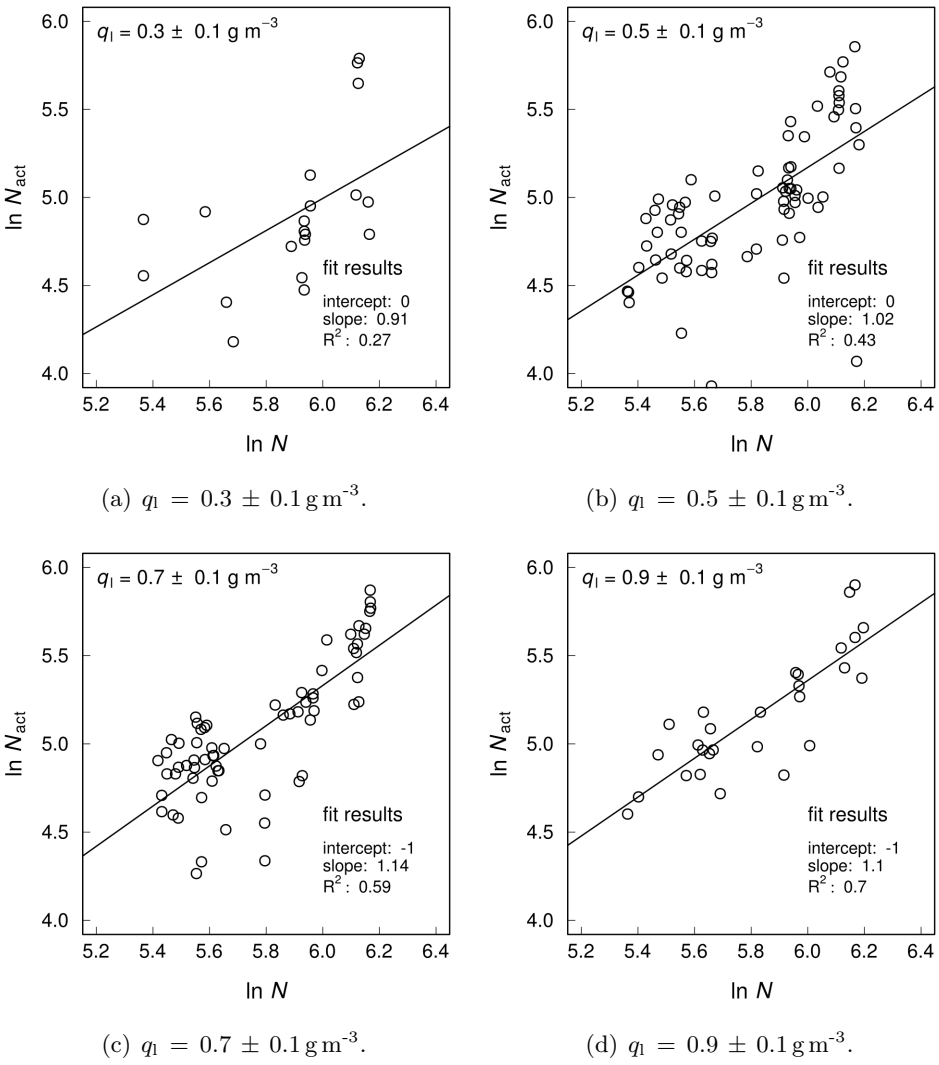

(a) $q_l = 0.3 \pm 0.1\,\mathrm{g\,m^{-3}}$.

(b) $q_l = 0.5 \pm 0.1\,\mathrm{g\,m^{-3}}$.

(c) $q_l = 0.7 \pm 0.1\,\mathrm{g\,m^{-3}}$.

(d) $q_l = 0.9 \pm 0.1\,\mathrm{g\,m^{-3}}$.

Figure 4.15: Calculation of aerosol-cloud interaction metric $\mathrm{d}\,ln(N_{\mathrm{act}})/\mathrm{d}\,ln(N)$ (slopes). Plotted are single measurements of the 30% most active clouds grouped for different liquid water content (q_l).

All plots in Fig. 4.15 feature a very large scatter. Consequently, the correlation of the linear fits is low ($R^2 < 0.7$). The scatter may result from additional processes modifying N_{act}, e.g., entrainment and mixing. As mentioned several times above, measurements affected by those processes cannot be fully excluded by the applied filter criteria for the most active clouds. The scatter reduces for increasing q_l, resulting in an increasing correlation. Furthermore, correlation is not a measure of the causal association between aerosol and

cloud properties (*McComiskey and Feingold*, 2012). Different studies show similar scatter in their derived ACI metrics, which they associate with natural variability and heterogeneities (e.g., *Painemal and Zuidema*, 2013; *Feingold*, 2003; *McComiskey and Feingold*, 2012).

Scatter can be reduced by aggregation of data, e.g., by averaging N_{act} for different classes of N. In that context, *McComiskey and Feingold* (2012) investigated the influence of data aggregation on ACI metrics, concluding, that aggregation can lead to significant biases. Therefore, in this study artificial increasing of the correlation by averaging was omitted. The in Fig. 4.15 shown $\mathrm{ACI_N}$ values are close to the physically meaningful maximum ($\mathrm{ACI_{N,\,max}} = 1$), emphasizing again the high sensitivity of trade wind cumuli towards changes in the aerosol particle number concentration. The weak overestimation of $\mathrm{ACI_{N,\,max}} = 1$ for $q_{\mathrm{l}} \leq 0.5\,\mathrm{g\,m^{-3}}$ may result from measurement uncertainties as well as statistical effects.

4.5 Sensitivity study

The results of the previous section identify clearly two major factors controlling the number of activated particles (N_{act}): vertical wind velocity (w_{90}) and the amount of available aerosol particles (CCN number concentration as well as total particle number concentration). Unfortunately, these findings are limited to measurements during 10 of 31 research flights. In this section, a sensitivity study is presented using the cloud microphysical parcel model by *Simmel and Wurzler* (2006). Beside evaluating the sensitivity of N_{d} on w and aerosol particle number concentration (N), also the shape of the particle number size distribution (NSD) and the particle hygroscopicity (κ) are taken into account.

The hereafter described sensitivity study follows a similar study done by *Reutter et al.* (2009), who evaluated the influence of aerosol chemical and microphysical properties as well as vertical wind velocity on pyro-convective clouds. Additionally, according to *Reutter et al.* (2009), the effects of changes to the shape of the particle number size distribution is considered in this work. Finally, the input parameters are chosen to represent the observations during the CARRIBA campaigns.

The cloud microphysical model is described in Sec. 2.5. The observed particle microphysical properties (cf. Fig. 3.5) are represented by two log-normal modes with fixed mean particle diameters of $D_{\mathrm{p,\,Aitken}} = 35\,\mathrm{nm}$ for the Aitken mode particles and $D_{\mathrm{p,\,acc}} = 140\,\mathrm{nm}$ for the accumulation mode particles. The standard deviation of both modes is fixed to 1.45. Further important parameters of the sensitivity study are summarized in Tab. 4.5.

The model is initialized with observations from the marine boundary layer: air pressure ($p = 1008\,\mathrm{hPa}$), air temperature ($T = 300\,\mathrm{K}$) and specific humidity ($q = 17.5\,\mathrm{g\,kg^{-1}}$). The

Table 4.5: Input parameters of the sensitivity study.

Parameter		Characteristics/ range of variation
updraft velocity	w	0.5–5 m s^{-1}
mean particle diameter of Aitken mode	$D_{\mathrm{p,\,Aitken}}$	35 nm (fixed)
mean particle diameter of accumulation mode	$D_{\mathrm{p,\,acc}}$	140 nm (fixed)
standard deviation of Aitken mode	σ_{Aitken}	1.45 (fixed)
standard deviation of accumulation mode	σ_{acc}	1.45 (fixed)
total particle number concentration	N	100–1000 cm^{-3}
ratio of Aitken to total particle number concentration	$\gamma = N_{\mathrm{Ait}}/N$	0.1–0.9
particle hygroscopicity	κ	0.1–0.9

resulting potential temperature ($\theta = 299.3\,\mathrm{K}$)[2] and q represent average conditions observed in the well-mixed marine boundary layer during both CARRIBA campaigns (cf. Sec. 3.2).
In the first step, the aerosol particle number size distribution is calculated for ambient humidity. Afterwards the air parcel is lifted using a prescribed fixed updraft velocity (w). Cloud base is defined as the altitude, where supersaturation (S) reaches its maximum. The air parcel is further lifted until N_{d} reaches constant values and $\mathrm{d}S/\mathrm{d}z \approx 0$.
The sensitivity study is based on model runs varying the four parameters: w, total particle number concentration (N), ratio of Aitken to total particle number concentration (γ) and hygroscopicity parameter (κ).
The parameter $\gamma = N_{\mathrm{Ait}}/N$ accounts for the ratio of the number concentration of Aitken mode particles (N_{Ait}) to the total particle number concentration. Therefore, γ helps to represent those cases where the particle number size distribution is dominated by Aitken mode particles ($\gamma > 0.5$) or accumulation mode particles ($\gamma < 0.5$).
Figure 4.16 schematically shows examples of NSDs for dominating Aitken mode particles (Fig. 4.16(c)), dominating accumulation mode particles (Fig. 4.16(a)) and equal number concentration of Aitken and accumulation mode particles (Fig. 4.16(b).

4.5.1 Different regimes of cloud droplet formation

At first, model runs with varied w, N and γ are presented. The particle hygroscopicity parameter is set to the mean value for both campaigns: $\kappa = 0.7$. The influence of the

[2] $\theta = T(\frac{p_0}{p})^{\frac{R_{\mathrm{dry}}}{c_{\mathrm{p}}}}$, where R_{dry} is the gas constant of dry air ($R_{\mathrm{dry}} = 281\,\mathrm{J\,kg^{-1}\,K^{-1}}$), c_{p} is the specific heat capacity of air ($c_{\mathrm{p}} = 1004\,\mathrm{J\,kg^{-1}\,K^{-1}}$), and $p_0 = 1000\,\mathrm{hPa}$ is the reference air pressure.

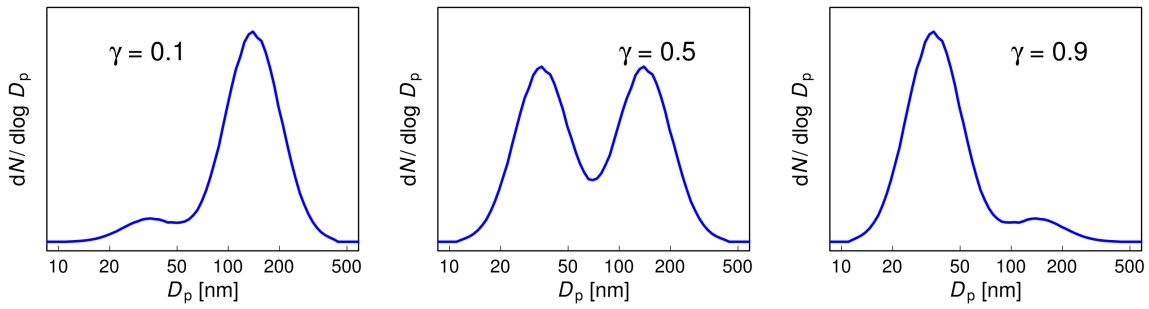

(a) $\gamma = 0.1$ (b) $\gamma = 0.5$ (c) $\gamma = 0.9$

Figure 4.16: Schematic examples of aerosol particle number size distributions for different values of γ.

hygroscopic behavior on N_d is discussed separately in Sec. 4.5.2.

Figure 4.17 shows contour plots of N_d as function of w and N for different shapes of the NSD. For accumulation mode dominated NSDs (Fig. 4.17(a)), the contour plot shows isolines, which are parallel to the w-axis. In this case, N_d is almost insensitive towards changes in the updraft velocity. In contrast, changes in N strongly affect N_d. A similar behavior is obvious for NSDs with equal particle number concentration in Aitken and accumulation mode (cf. Fig. 4.17(b)). Therefore, in both cases N_d is limited by the amount of available aerosol particles (aerosol-limited regime, cf. *Reutter et al.*, 2009).

For NSDs with a dominating Aitken mode (cf. Fig. 4.17(c)), isolines show a different behavior. Focusing on $w > 2\,\mathrm{m\,s^{-1}}$ and $N < 600\,\mathrm{cm^{-3}}$, N_d is more sensitive to changes in N. In the other cases, N_d is also sensitive to changes in w, indicating that N_d is sensitive to both w and N (updraft and aerosol sensitive regime, cf. *Reutter et al.*, 2009).

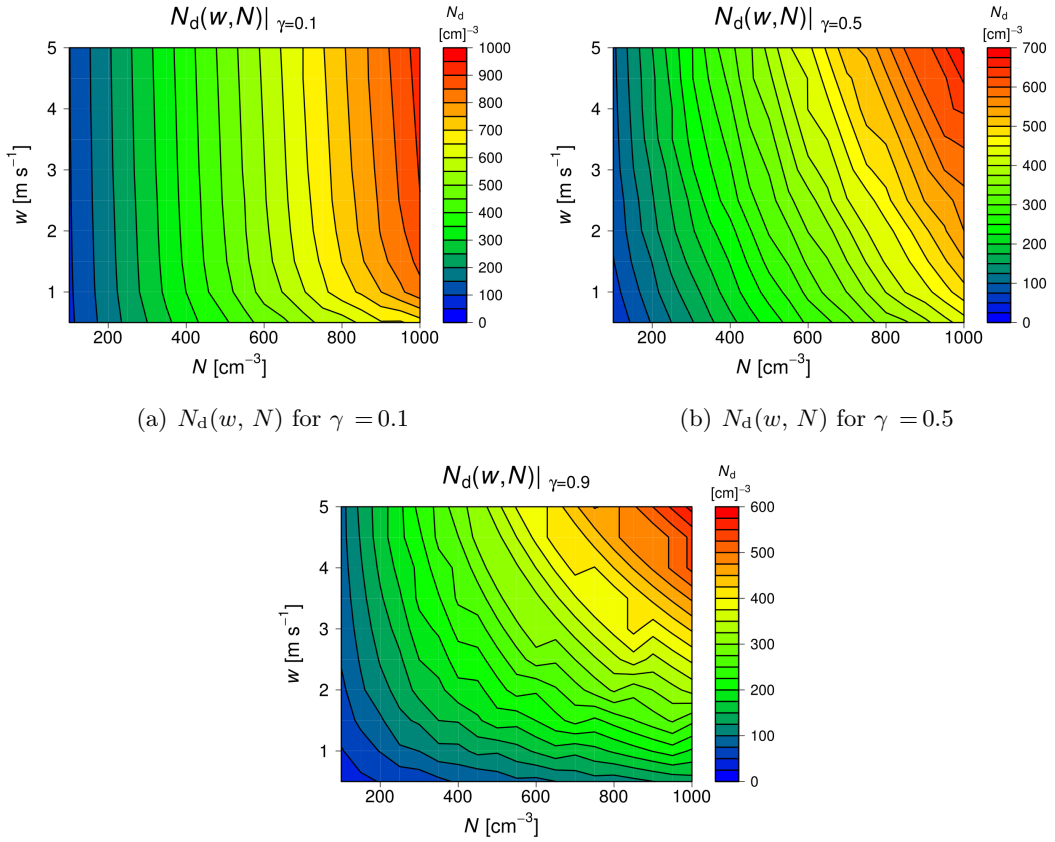

(a) $N_\mathrm{d}(w,\,N)$ for $\gamma\,=0.1$

(b) $N_\mathrm{d}(w,\,N)$ for $\gamma\,=0.5$

(c) $N_\mathrm{d}(w,\,N)$ for $\gamma\,=0.9$

Figure 4.17: Model calculations of N_d depending on w and total aerosol particle concentration N for different shapes of bimodal particle number size distribution (γ).

4.5.2 Influence of particle hygroscopicity on cloud droplet number concentration

In this section, the influence of particle hygroscopicity on N_d is investigated. Again, according to *Feingold and Remer* (2001) the susceptibility of the droplet number concentration (N_d) towards changes in other quantities (X_i) is defined as follows:

$$\zeta(X_\mathrm{i}) = \frac{\delta \ln N_\mathrm{d}}{\delta \ln X_i}\,, \tag{4.7}$$

whereby $X_\mathrm{i} \in (\kappa, N)$. To make a clear distinction between the observational results in Sec. 4.4.3 and the modeling results of this section (X_i) is used here instead of ACI, although both parameters are basically identical. In practice, $\zeta(X_\mathrm{i})$ is calculated by applying a linear regression fit to a scatter plot of $\ln(N_\mathrm{d})$ and $\ln(X_\mathrm{i})$. The slope of the linear fit represents $\zeta(X_\mathrm{i})$. The modeling results do not have to be constrained for different liquid water contents, because these results refer all to the same altitude above cloud base.

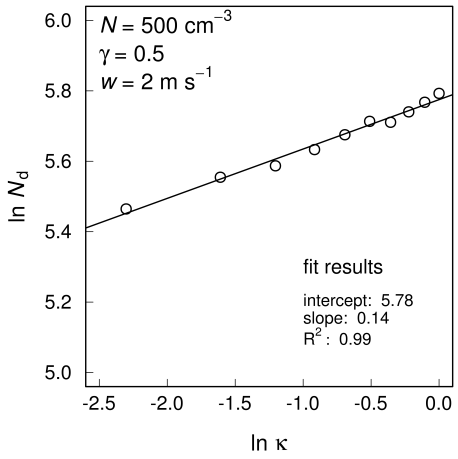

Figure 4.18: Logarithm of modelled N_d versus logarithm of κ for $N = 500\,\mathrm{cm}^{-3}$, $w = 2\,\mathrm{m\,s}^{-1}$ and $\gamma = 0.5$. Straight line represents a linear regression. The slope of this fit represents $\zeta(\kappa)$.

Figure 4.18 shows $\ln(N_\mathrm{d})$ versus $\ln(\kappa)$ for one model run calculated for $N = 500\,\mathrm{cm}^{-3}$, $w = 2\,\mathrm{m\,s}^{-1}$ and $\gamma = 0.5$ to demonstrate the calculation of $\zeta(\kappa)$. Since, $\zeta(\kappa) = \delta\ln(N_\mathrm{d})/\delta\ln(\kappa)$ can be approximated by $\approx (\Delta N_\mathrm{d}/N_\mathrm{d})/(\Delta\kappa/\kappa))$, for $\zeta = 0.14$ a relative change of 50% in κ results in a relative change of 7% in N_d.
Furthermore, $\zeta(\kappa)$ is calculated within this sensitivity study for different N and γ (Fig. 4.19(a)) and $\zeta(N)$ is calculated depending on κ and γ (Fig. 4.19(b)).
The contour plot in Fig. 4.19(a) shows low values for $\zeta(\kappa)$ ranging between 0 and 0.4, while its highest values are calculated for very high γ close to 0.9, representing an Aitken mode dominated NSD. Overall, the isolines are parallel to the ordinate indicating that the susceptibility of N_d towards κ is almost independent of N. For comparison, Fig. 4.19(b) shows $\zeta(N)$ ranging between 0.6 and 1, indicating that relative changes of N of 50% cause changes in N_d between 30% and 50%. The susceptibility $\zeta(N)$ is highest for accumulation mode dominated NSD, where relative changes in N influence N_d on the same degree. For the major part of Fig. 4.19(b), the isolines are parallel to the ordinate, which again emphasizes the rather weak influence of κ on N_d compared to N.

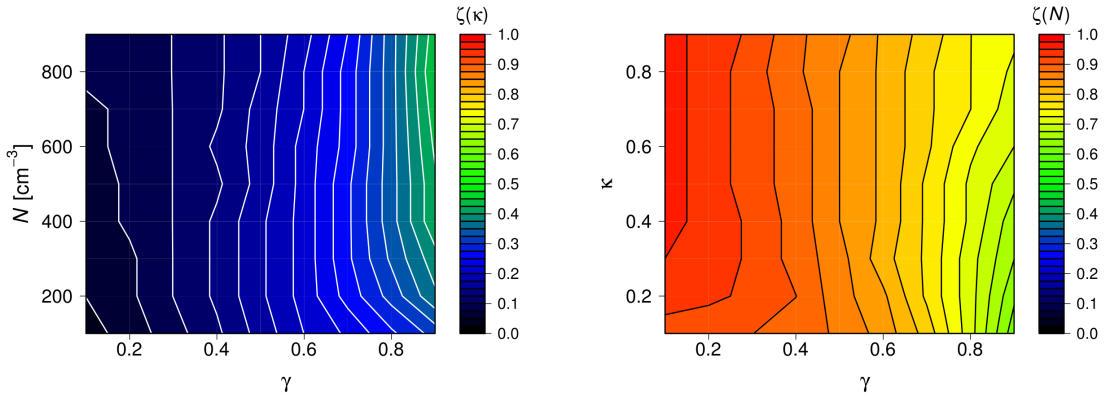

(a) Susceptibility of N_{act} towards κ ($\zeta(\kappa)$).

(b) Susceptibility of N_{act} towards N ($\zeta(N)$).

Figure 4.19: Modelled susceptibility (ζ) of number of activated particles towards hygroscopicity parameter κ and total aerosol particle number concentration N. The susceptibility $\zeta(\kappa)$ is calculated for different N and γ, $\zeta(N)$ is calculated for different κ and γ.

4.6 Conclusions

This chapter is motivated by the question: What does control the cloud droplet number concentration of trade wind cumuli? The analysis is based on one case study and a comprehensive statistical analysis of the 30% most active clouds observed during 10 research flights of $\mathrm{CARRIBA_{wet}}$ and $\mathrm{CARRIBA_{dry}}$ and a sensitivity study using a cloud microphysical parcel model.

At the beginning of this chapter, a method is introduced to calculated the number of activated particles as well as the activation diameter, providing a unique dataset of estimates of activation diameters and corresponding critical supersaturations in trade wind cumuli based on in-situ airborne measurements. The number concentration of activated particles reaches values up to 400 $\mathrm{cm^{-3}}$ and activation diameters range within 40–180 nm. Corresponding critical supersaturation values show a broad range of approximately 0.1–0.9%, which is in good agreement with literature values for maritime clouds (*Mason*, 1971). In comparison to ground-based results of *Hammer et al.* (2014) at the high-alpine station Jungfraujoch (0.37–0.5% supersaturation) and results of *Asmi et al.* (2012) at the Puy-de-Dôme (0.1–0.7% supersaturation), the here presented supersaturation estimates show generally similar values with a slight tendency to higher values for the trade wind cumuli.

Further results of the statistical analysis identified clearly the vertical wind velocity inside the clouds and the amount of available aerosol as major factors affecting the number of activated particles. This is hardly surprising, since both parameters are basic requirements for the development of clouds. Nevertheless, both parameters do not affect cloud droplet num-

ber concentration with the same intensity. Median number concentrations of the activated particles calculated for pairs of vertical wind velocity and particle number concentration (Fig. 4.14) imply a stronger influence of the number concentration of the available aerosol particles.

To my knowledge, this study presents the first ACI calculations for trade wind cumuli based on in-situ airborne observations. Calculated ACI_N are close to the physically meaningful maximum of 1, which underlines the strong sensitivity of the trade wind cumuli on changes in the particle number concentration. During VOCALS-REx *Wood et al.* (2011) aerosol-cloud interactions of large stratocumulus cloud fields were investigated. There, *Painemal and Zuidema* (2013) found also high ACI metrics between 0.76 and 0.92.

The applied sensitivity study allows to put the observational findings into a broader context. The input parameters of the sensitivity study are based on observations and cover the range of nearly all observations during the both measurement campaigns. Therefore, the results are fully representative for the trade wind regime near Barbados. Additionally, the cloud droplet activation is calculated by solving the droplet growth equation. Hence, the results are not limited by the application of any parameterization scheme as used in different approaches (e.g., *Ward et al.*, 2010).

With the help of a sensitivity study using a spectral cloud microphysical parcel model, the sensitivity of N_d towards changes in the particle number concentration and vertical wind velocity is investigated. In the trade wind regime, N_d is found to be aerosol-limited (*Reutter et al.*, 2009). Only in cases with very high Aitken mode particle number concentration (compared to total particle number concentration), the sensitivity of N_d is increased towards both: updraft velocity and aerosol particle number concentration (updraft and aerosol sensitive regime, cf. *Reutter et al.*, 2009). This dependence on the shape of the particle number size distribution agrees well with the findings of *Ward et al.* (2010), who investigated the effects of particle number size distribution and chemical composition on droplet activation with a Lagrangian parcel model.

Furthermore, the influence of particle hygroscopicity (κ) was investigated using the cloud microphysical parcel model. The susceptibility of the droplet number concentration towards changes in κ is approximately $\zeta(\kappa) = 0.2$. Only for Aitken mode dominated NSDs the susceptibility increases to $\zeta(\kappa) = 0.4$. In contrast, investigations on the susceptibility of N_d towards N shows much higher values: $0.6 \leq \zeta(\kappa) \leq 0.95$. This emphasizes again that trade wind cumuli are more sensitive towards changes in the microphysical aerosol particle properties rather than towards changes in the chemical particle properties, which agrees qualitatively with the findings of *Dusek et al.* (2006).

The low $\zeta(\kappa)$ partly results from a buffering mechanism. For a fixed supersaturation, a

change of the particle hygroscopicity to higher values would allow to activate smaller particles, resulting in an increased N_d. Therefore, κ should have a significant effect on N_d. However, the peak supersaturation at cloud base is not invariant to changes in particle properties. An increase in κ leads to a more intense hygroscopic growth, increasing particle surface area (of wet particles before activation) and a decrease in the peak supersaturation at cloud base. This effect counteracts the above described process and buffers the influence of κ on N_d. The same holds true for an increase in N (cf. Fig 4.17 for high N). Within the range of the here presented observations, the latter effect is less important.

Chapter 5

Case Studies

In the last chapter, a statistical analysis concerning the cloud droplet number concentration and its sensitivity towards changes in particle properties is presented. Thereby, the high sensitivity of the droplet number concentration towards changes in the particle number size distribution is proofed. This chapter introduces two scenarios leading to significant increases in the aerosol particle number concentration: (1) advection of an African particle plume and, (2) local anthropogenic pollution.

5.1 Influence of an advected African particle plume

During the period from April 14 to April 16, 2011, Barbados was influenced by a lofted aerosol particle layer between 2 and 4 km height.

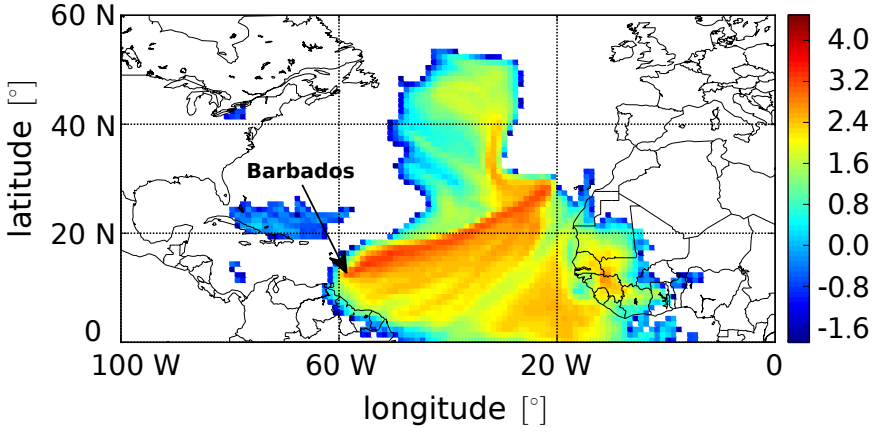

Figure 5.1: Footprint of 10-day backward simulations done with FLEXPART (*Stohl et al.*, 2005) for aerosol layers which crossed Barbados in the altitude range of 2000–4000 m on April 14, 2011 between 19:30–21:30 UTC. The color code corresponds to the logarithm of the sum of the residence time of all air parcels that have passed over a certain source region below 1000 m height.

The origin of the lofted particle layer is investigated with the help of the Lagrangian particle dispersion model FLEXPART, operated by the Norwegian Institute for Air Research (*Stohl et al.*, 1998; *Stohl and Thomson*, 1999; *Stohl et al.*, 2005). Further details about FLEXPART can be found in Appendix F.

Results of the transport modeling of 50,000 air parcels is shown in Fig. 5.1. The plot represents air masses, which arrived at Barbados between 2000 and 4000 m height at 19:30 UTC on April 14, 2011 (time period of research flight #21). The color code corresponds to the logarithm of the sum of the residence time of all air parcels that have passed over a certain source region. Thereby, only air parcels that touched the height range below 1000 m within the last 10 days are considered.

As seen from this FLEXPART transport simulation, the respective particle layer was advected over large areas of the North-Atlantic and touched the western part of African continent.

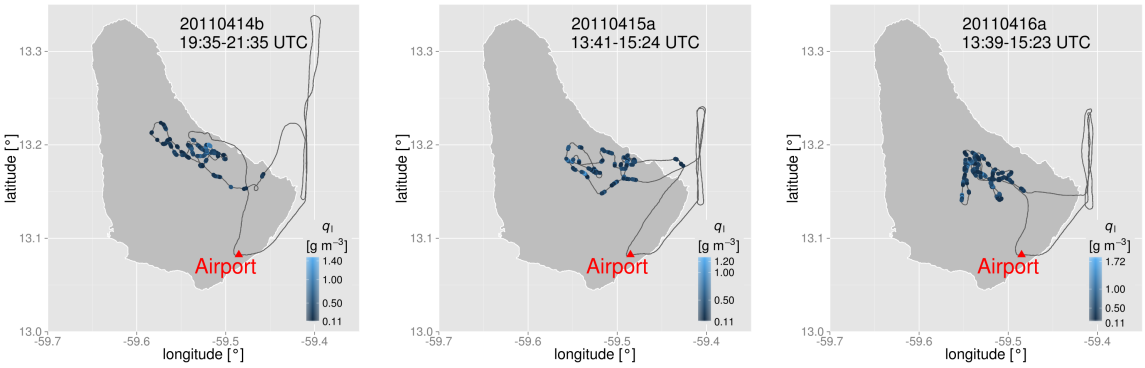

(a) Research flight #21. (b) Research flight #22. (c) Research flight #23.

Figure 5.2: Flight tracks of ACTOS during research flights #21 (15:35–17:35 LT), #22 (9:41–11:24 LT) and #23 (9:39–11:23 LT) on April 14, 15 and 16 in 2011. Bluish dots indicate the liquid water content (q_l) of observed clouds.

Figure 5.2 shows the flight tracks and location of the observed clouds (bluish dots) during the research flights #21, #22 and #23 on April 14, 15 and 16 in 2011. All three flights began with a horizontal leg at about 100 m altitude above the ocean east of the coast. The horizontal leg was followed by a vertical profile east of the island up to an altitude of approximately 2500 m and a cloud chasing part. During these three flights, clouds were sampled over the island.

5.1.1 Vertical profiles

The vertical stratification is shown in Fig. 5.3 in terms of vertical profiles of the potential temperature θ, specific humidity q, horizontal wind speed UU, wind direction dd, total particle number concentration N and CCN concentration measured at 0.26% supersaturation $N_{\mathrm{CCN,\,0.26\%}}$ for the research flights #21 (black), #22 (green) and #23 (blue).

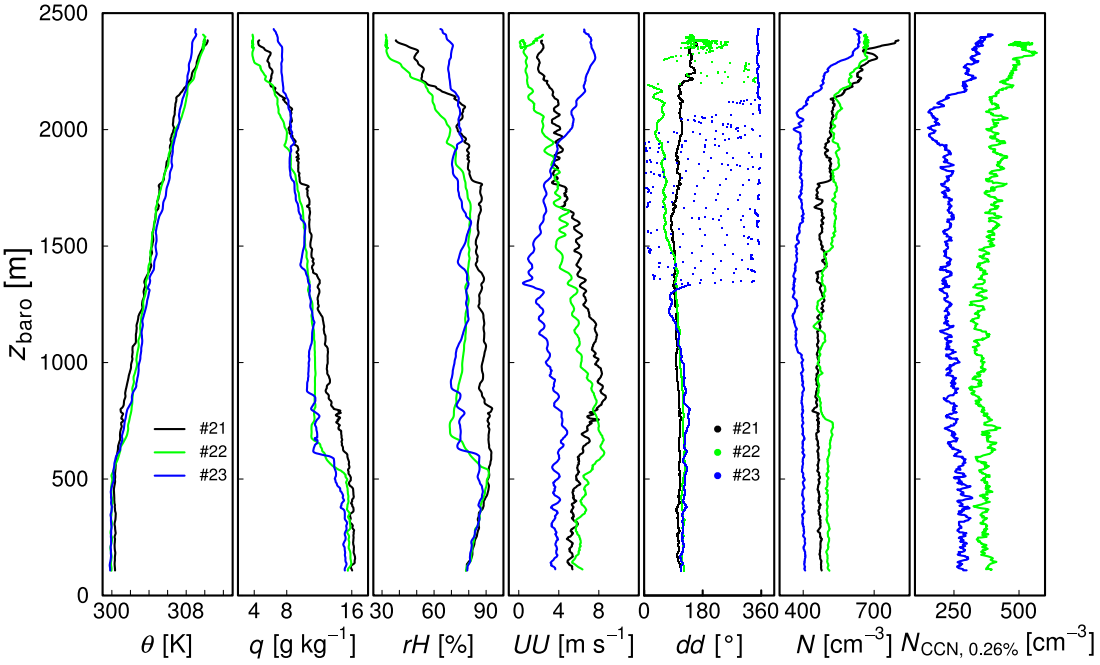

Figure 5.3: Vertical profiles during research flights #21 (black), #22 (green) and #23 (blue) on April 14, 15 and 16 in 2011 of potential temperature θ, specific humidity q, relative humidity rH, horizontal wind speed UU, wind direction dd, total particle number concentration N and CCN concentration measured at 0.26% supersaturation $N_{\mathrm{CCN,\,0.26\%}}$ (from left to right).

The stratification is similar in all three cases. Potential temperature θ and q are constant within the lowermost 600 m at 300 K and 16 g kg^{-1}, respectively. Above, θ increases indicating conditionally unstable stratification. Instead, q decreases with increasing altitude, whereas the decrease is most pronounced for research flights #22 and #23. The relative humidity increases within the well-mixed layer and features for research flights #22 and #23 a sharp decrease above 600 m, whereas in the profile of research flight #21, rH stays high. During the first two research flights, the wind comes from easterly directions almost independent of height with velocities between 5 and 8 m s^{-1} in the well-mixed layer. Above, UU decreases. The profile obtained during research flight #23 shows lower wind speeds and a shift to northerly wind directions for altitudes above 1300 m. Above 2000 m, UU in-

creases. For all individual research flights, N is constant within the well-mixed layer, while the highest concentrations are observed during research flight #22 ($N \approx 500\,\mathrm{cm}^{-3}$). All three profiles of N show an increase above 2000 m altitude by approximately $100\,\mathrm{cm}^{-3}$. The profiles of $N_{\mathrm{CCN},\,0.26\%}$ behave similar to those of N, also showing increasing concentrations up to $N_{\mathrm{CCN},\,0.26\%} \approx 500\,\mathrm{cm}^{-3}$ for increasing altitude. For technical reasons, there are no CCN concentrations available for research flight #21.

Coincident lidar measurements were performed from the Max Planck Institute for Meteorology (MPI-M, Hamburg) during all three flights at the Barbados Cloud Observatory (Deebles Point, Sec. 2.4.2). Figure 5.4 presents the averaged profiles of the particle backscatter coefficient at 355 and 532-nm wavelength (blue and green) for each flight period. Although the Raman method (*Ansmann et al.*, 1992) was used to determine the particle backscatter coefficient, low signal-to-noise ratio in the Raman channel prohibited the direct detection of the extinction coefficient. Profiles of the volume and particle linear depolarization ratio (532 nm) are shown in grey allowing the differentiation between spherical (almost 0) and non-spherical particles (> 0) (*Sassen*, 2005) and further aerosol characterization (*Freudenthaler et al.*, 2009; *Groß et al.*, 2013).

In all three cases, the backscatter coefficient increases in the well-mixed layer in accordance to the increasing relative humidity (Fig. 5.3) and hygroscopic growth of marine aerosol particles. The profile of the particle backscatter coefficient indicates free-tropospheric aerosol up to heights of 4 km in all cases. Above roughly 2 km height, the particle backscatter coefficient is wavelength independent at 355 and 532-nm wavelengths, which indicates large dust particles (*Tesche et al.*, 2009). In agreement, the particle linear depolarization ratio shows the highest values of > 20, 20, 15% for the three cases. However, those particle linear depolarization ratios are considerable lower than common observed particle linear depolarization ratios of pure and fresh Saharan dust of 30–35% (*Freudenthaler et al.*, 2009). The exact reason was not investigated, but a change of the dust properties itself due to aging during the transport or a mixing with different aerosol particles is likely. Results of the FLEXPART model calculation shown in Fig. 5.1 further support this.

In addition to the lidar data, the inlays in the right panels of Fig. 5.4(a–c) show the in-situ measured total particle and CCN number concentrations for particles smaller than $D_{\mathrm{p}} = 2.5\,\mu\mathrm{m}$. The particle depolarization ratio is most sensitive to particles larger than $1\,\mu\mathrm{m}$ (coarse mode) (e.g., *Ansmann et al.*, 2012). Nevertheless, N and $N_{\mathrm{CCN},\,0.26\%}$ correlate well with the particle linear depolarization ratio for research flights #21 and #22, indicating a concentration increase for both fine (particles smaller than $1\,\mu\mathrm{m}$) and coarse mode particles.

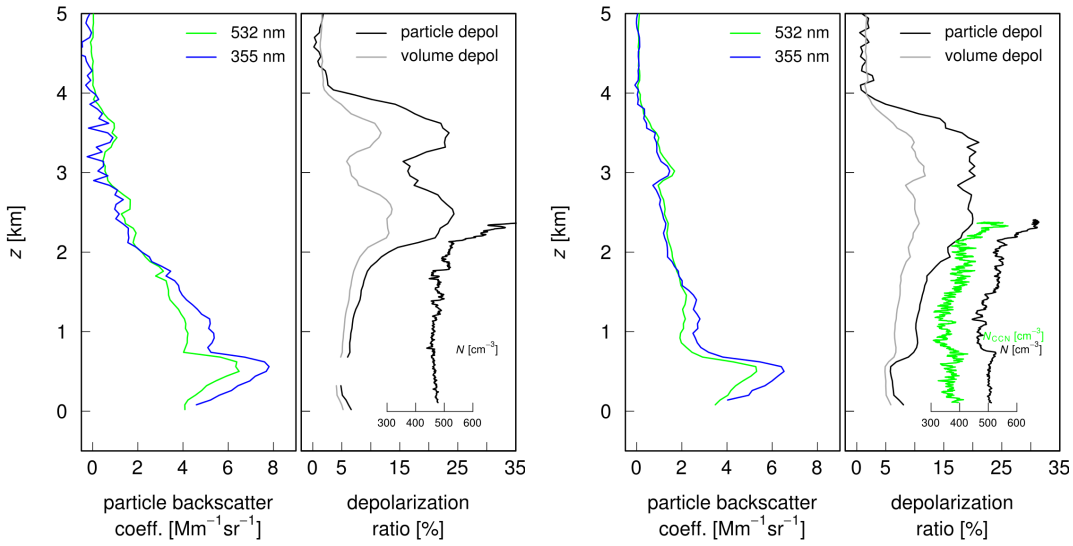

(a) Research flight #21.

(b) Research flight #22.

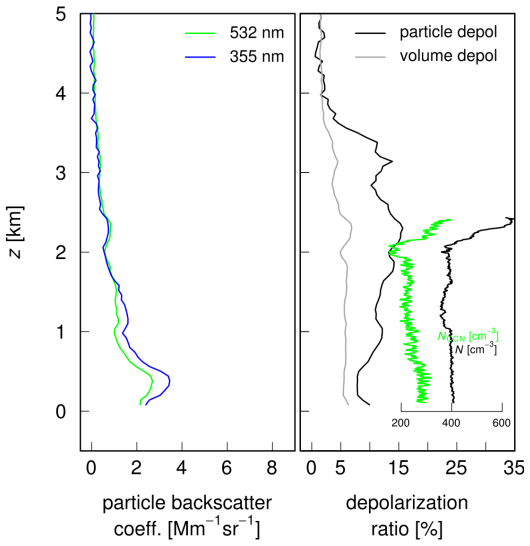

(c) Research flight #23.

Figure 5.4: Vertical profiles of the particle backscatter coefficient for two wavelengths: $\lambda = 532\,\text{nm}$ (green), $\lambda = 355\,\text{nm}$ (blue) and particle (black) as well as volume (grey) linear depolarization ratio averaged for the time of three research flights (#21, #22, #23). Inlays show the in-situ measured particle number (N, black) and CCN number concentration measured at 0.26% supersaturation ($N_{\text{CCN, 0.26\%}}$, green).

5.1.2 Particle number size distributions

In the following, average particle number size distributions measured at two different altitude ranges are presented in Fig. 5.5. Dashed lines refer to NSDs representative for the well-mixed layer below 600 m altitude, solid lines show NSDs measured above 2000 m altitude, corresponding the altitude range of the lofted particle layer. The colors indicate the different research flights.

The NSDs above 2000 m, which were measured during research flights #21 and #22, show a mono-modal distribution with a strong maximum at approximately $D_p = 130$ nm. The corresponding NSDs in the well-mixed layer (during research flights #21 and #22) show a nearly similar shape, but the concentration is especially during research flight #21 decreased for particles smaller than $D_p = 200$ nm. At the end of this event (research flight #23), the NSDs measured in the well-mixed layer show still similarities with those obtained during the two first research flights. In contrast to that, above 2000 m, the NSDs show a bimodal structure with a pronounced Aiken mode and much lower concentration for particles larger than $D_p = 100$ nm, indicating different particle properties, most likely resulting from an air mass change.

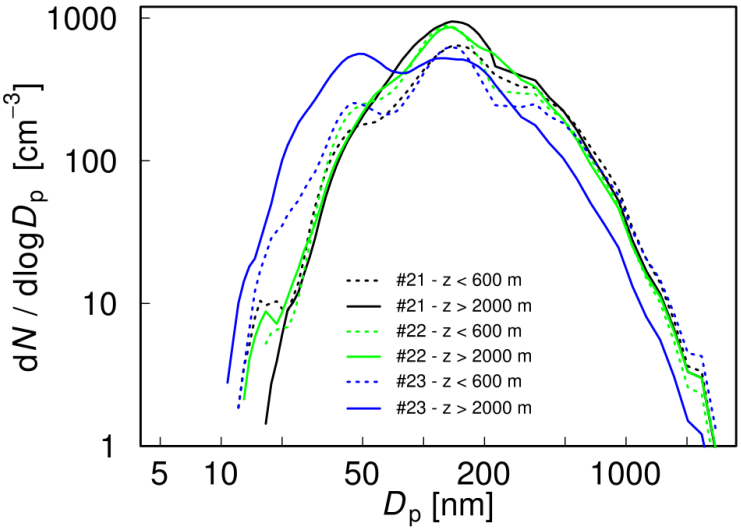

Figure 5.5: Average particle number size distributions of three measurement flights (#21, #22, #23). Thick lines represent size distributions above 2000 m altitude, dashed lines mark size distributions measured in the well-mixed marine boundary layer.

Former ground-based studies on particle number size distributions report much more pronounced modes of larger particles ($\approx$ 1 μm) for dust-influenced areas (e.g., *Schladitz et al.* (2011) for measurements on the Cape Verde island). Nevertheless, these measurements were obtained much closer to source of the dust particles. Measurements of

Kaaden et al. (2009) proof that dust particles can significantly contribute to the number fraction even for particle diameters smaller than 250 nm. The coincident lidar measurements and the FLEXPART analysis support that the in Fig. 5.5 shown NSDs are influenced by non-spherical particles. However, the peak at $D_p \approx 130$ nm in the NSDs measured during research flights #21 and #22 can not be explained purely by dust particles, rather than most probably by a mixture of particles originating the African continent. Finally, airborne measurements of *Jung et al.* (2013) show similar shaped NSDs during an intense African dust event over the western Atlantic and eastern Caribbean in early April 2010.

5.1.3 Impact on cloud droplet number concentration

In this part, the influence of the lofted particle layers on the cloud droplet number concentration is investigated. Since cloud droplet number concentration data are not available for the here introduced case study, the cloud microphysical parcel model of *Simmel and Wurzler* (2006) is applied (see Sec. 2.5).

The different shapes of the particle number size distributions are represented by three log-normal fits of single particle number size distributions measured in the well-mixed layer below 600 m altitude and above 2000 m. The corresponding average NSDs are presented in Fig. 5.5. According to the ground based measurements the particle hygroscopicity is set to $\kappa = 0.6$ (cf. Fig. 3.2).

The parcel model is initialized with: $T = 300$ K, $p = 1005$ hPa, $q = 16.2$ g kg^{-1} and a relative humidity of 78%. In the first model step, the particle number size distribution is calculated for ambient humidity. Afterwards, the model is run for different fixed updraft velocities ranging between 0.5–5 m s^{-1}.

Figure 5.6 shows the average modeled cloud droplet number concentration for different updraft velocities and different research flights. The results are grouped for the different particle properties in the well-mixed layer (black) and altitudes above 2000 m (green). In general, N_d decreases in the course of the three research flights, especially for the lofted particle layer, which is consistent with the shown NSDs in Fig. 5.5. The highest values and the highest variability of N_d are achieved for the lofted particle layer, measured during research flight #21 ($N_d \approx 530$ cm^{-3}). Research flight #21 shows also the largest difference of approximately 20% between the results from the well-mixed layer and the lofted particle layer. During research flight #22, N_d is not significantly different for the two different altitudes, indicating a down-mixing of the particles from the upper part of the atmosphere into the boundary layer. The lowest values of N_d are calculated for research flight #23 ranging within 280 and 430 cm^{-3}.

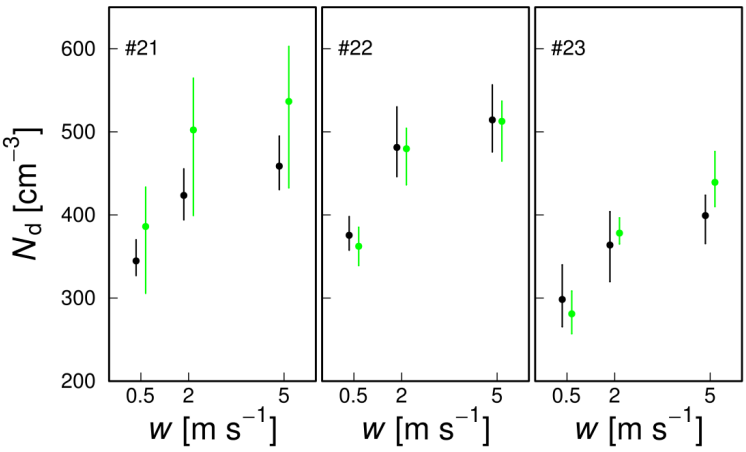

Figure 5.6: Average modeled cloud droplet number concentration for different updraft velocities (0.5, 2, 5 m s^{-1}) and different initial particle number size distributions representing the conditions in the well-mixed layer (black) and above 2000 m altitude (green) during research flight #21 (left panel), #22 (middle panel) and #23 (right panel). The error bars represent the minimum and maximum values resulting from the initialization with single NSDs.

5.1.4 Conclusions

In this case study, the effect of a lofted aerosol particle layer, which most likely originated from the African continent, on the cloud droplet number concentration is investigated. Vertical profiles of in-situ and remote sensing data clearly identified a layer of non-spherical particles, which were mixed into the well-mixed marine boundary layer.

The particle number size distributions obtained within the lofted layer indicate an increase in the particle number concentration and a rather mono-modal shape. Thus, these NSDs embody a contrast to the average NSDs obtained during CARRIBA$_{\mathrm{wet}}$ and CARRIBA$_{\mathrm{dry}}$ (cf. Fig. 3.5). The measured CCN concentration at 0.26% supersaturation shows values up to 500 cm^{-3}, which also represents the upper edge of all CCN measurements during both campaigns (cf. Fig. 3.2).

Additionally, the shape of the NSDs during this event is comparable to the accumulation mode dominated aerosol scenarios introduced in the sensitivity study in Chapter 4, meaning that increases in N directly influence the number concentration of large particles and the CCN concentration. For those cases, the sensitivity of the cloud droplet number concentration towards changes in the particle number concentration is highest ($\zeta(N) > 0.9$). Furthermore, the sensitivity of N_{d} towards changes in the particle hygroscopicity is for this case comparable low (approximately $\zeta(\kappa) = 0.2$, cf. Fig. 4.19(a)).

Finally, in the course of this event, the modeled N_d varies by approximately 30% (com-

pare e.g., model results of research flights #21 and #23 for $2\,\mathrm{m\,s^{-1}}$) and barely falls below $N_\mathrm{d} = 300\,\mathrm{cm^{-3}}$.

The here presented findings proof that an advected African particle plume, transported several thousands of kilometers over the Atlantic, is able to substantially alter cloud microphysical properties of trade wind cumuli.

5.2 Influence of local anthropogenic pollution

On April 19, several small fires were observed in the North of Barbados. Therefore, two measurement flights were conducted with similar flight pattern. During both flights, vertical profiles up to an altitude of 2400 m asl east off the coast of Barbados were performed to characterize the stratification unbiased by the local anthropogenic pollution. Afterwards, ACTOS flew to the west coast of Barbados, where a quasi-stationary cloud field developed close to the capital of Barbados — Bridgetown. The measurements close to Bridgetown were probably influenced by both: local fires and anthropogenic pollution probably caused by traffic.

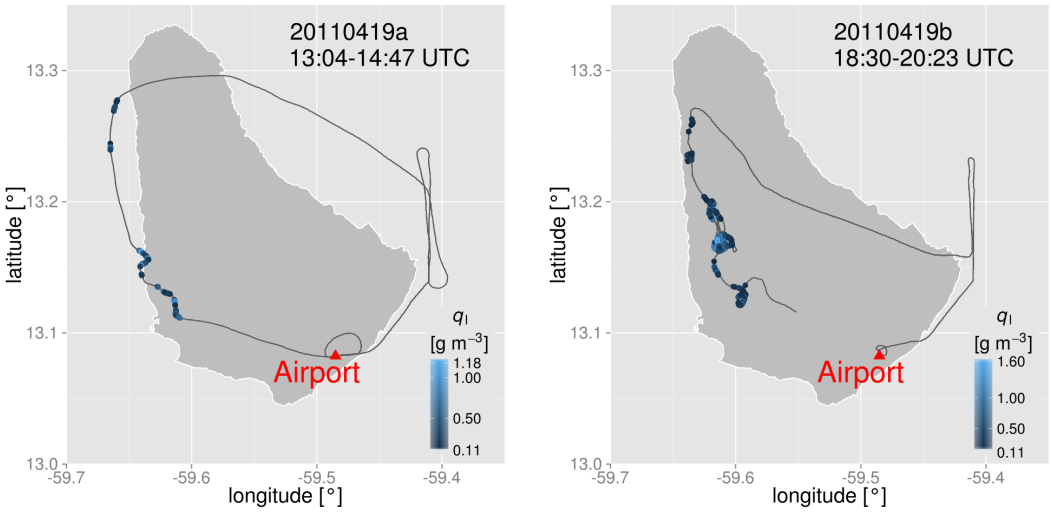

(a) Research flight #25.

(b) Research flight #26.

Figure 5.7: Flight tracks of ACTOS during research flights #25 (9:04–10:47 LT) and #26 (14:30–16:23 LT) on April 19, 2011. Bluish dots indicate liquid water content (q_l) of observed clouds.

Figure 5.7 shows the flight pattern and the location of the observed clouds (bluish dots). Unfortunately, for technical reasons, there are no data available for the last minutes of research flight #26. Here, data are shown until the final descent towards the airport until an altitude of 950 m.

5.2.1 Vertical Profiles

Figure 5.8 shows vertical profiles of selected parameters during the ascents of the research flights #25 (black lines) and #26 (green lines). Additionally, the shaded areas represent the 5th and 95th percentile of all observations over the west coast of the island during research flights #25 (grey area) and #26 (green area).

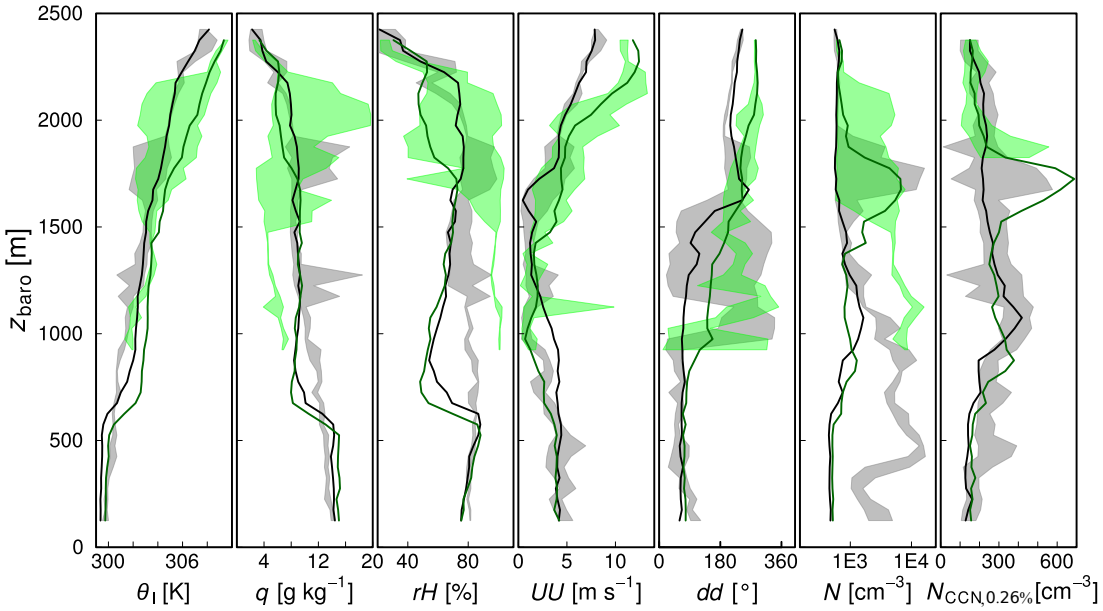

Figure 5.8: Vertical profiles during research flights #25 (black lines) and #26 (green lines) on April 19 in 2011 of liquid potential temperature θ_l, specific humidity q, relative humidity rH, horizontal wind speed UU, wind direction dd, total particle number concentration N and CCN concentration measured at 0.26% supersaturation $N_{CCN,\,0.26\%}$. Lines refer to measurements over the ocean east off the coast. The shaded areas refers to 5th and 95th percentile of the observations over the west coast of the island during research flights #25 (grey shaded area) and #26 (green shaded area).

First, I focus on the vertical profiles obtained during the ascents east of the island (thick lines). Both profiles show similar results for the research flights #25 and #26. The liquid potential temperature θ_l[1] is constant within the sub-cloud layer indicating a well-mixed layer up to 600 m. The well-mixed layer is topped by an inversion and, above the inversion $\mathrm{d}\theta_l/\mathrm{d}z$ decreases. Nevertheless, $\mathrm{d}\theta_l/\mathrm{d}z$ remains positive, indicating conditionally unstable stratification. Above 1600 m, $\mathrm{d}\theta_l/\mathrm{d}z$ increases again. The specific humidity q is also constant within the SCL at around 15 g kg^{-1} and decreases above, rH shows a similar behavior. In the lowermost 1000 m, the wind comes from east with 4 m s^{-1}. Above, UU decreases towards very low values and increases again at 1600 m coming from westerly directions. The N and $N_{CCN,\,0.26\%}$ feature constant concentrations of $N \approx 500\,\mathrm{cm}^{-3}$ and $N_{CCN,\,0.26\%} \approx 150\,\mathrm{cm}^{-3}$ in the well-mixed layer. At approximately 1100 m altitude, N and $N_{CCN,\,0.26\%}$ increase

[1]The liquid potential temperature takes into account the latent heat release during condensation (after *Betts* (1973)): $\theta_l = \theta\left(1 - \frac{q_l \cdot L_v}{c_p \cdot T}\right)$, where $L_v = 2.5\,10^6\,\mathrm{J\,kg^{-1}}$ is the latent heat of condensation and $c_p = 1004\,\mathrm{J\,kg^{-1}\,K^{-1}}$ is the specific heat capacity of air. Outside of clouds, where $q_l = 0\,\mathrm{g\,m^{-3}}$, θ_l equals θ.

during research flight #25 to $N \approx 1000\,\mathrm{cm^{-3}}$ and $N_{\mathrm{CCN},\,0.26\%} \approx 350\,\mathrm{cm^{-3}}$ and decrease above. During research flight #26, this first maximum is less pronounced at a lower altitude ($z_{baro} \approx 900\,\mathrm{m}$). A second maximum appears at an altitude of about 1700 m, where N and $N_{\mathrm{CCN},\,0.26\%}$ exceed values of $8000\,\mathrm{cm^{-3}}$ and $700\,\mathrm{cm^{-3}}$, respectively. Since the altitude of this aerosol layer correlates with westerly winds, it is probably originating from the transport of anthropogenic pollution particles from the island to the East.

As mentioned above, the shaded areas represent 90% of all observations during the two flights above the island inside and in the vicinity of a quasi-stationary cloud field for height intervals of 50 m. Observations of θ_l and q show a large variability in the range of 302–308 K and 4–20 $\mathrm{g\,kg^{-1}}$ indicating that ACTOS penetrated upwelling moist air parcels and compensational dry downdrafts from the atmosphere above (also visible in the rH-profiles). The varibility in dd indicates changing wind directions, including westerly directions, which could explain the elevated particle number concentrations measured east of the island. During the penetration of the pollution plumes, N dramatically increases towards $N \approx 20000\,\mathrm{cm^{-3}}$, while $N_{\mathrm{CCN},\,0.26\%}$ increases towards $600\,\mathrm{cm^{-3}}$.

5.2.2 Measurements at cloud level

Measurements at cloud level indicate, that the clouds over the west coast of the island developed directly within the plumes of anthropogenic pollution. Figure 5.9 shows time series of liquid water content q_l, potential (and liquid potential) temperature θ (θ_l), specific humidity q, particle number concentration N and CCN concentration $N_{\mathrm{CCN},\,0.26\%}$ during several cloud penetrations at a constant altitude of $1800 \pm 100\,\mathrm{m}$.

The liquid water content (uppermost panel) is anti-correlated with θ_l and correlated with q and θ, which indicates that the clouds developed in warm and moist air parcels. Instead, the environmental air is comparable dry ($q \approx 8\,\mathrm{g\,kg^{-1}}$). Mostly, θ_l features lower values inside the clouds than in the environment, while θ is either increased or almost constant during cloud penetrations, emphasizing conditionally unstable stratification. Furthermore, strong peaks in N occur at the same locations where ACTOS penetrates the clouds. Although, N represents only the interstitial particles, it increases substantially in the vicinity and inside the clouds roughly by an order of magnitude reaching values higher than $10000\,\mathrm{cm^{-3}}$. The CCN concentration at 0.26% supersaturation shows a different behavior, $N_{\mathrm{CCN},\,0.26\%}$ drops, when ACTOS enters the cloud, indicating that the supersaturation inside the cloud is larger than 0.26%. In the clean environment outside of clouds, which is characterized by $N < 1000\,\mathrm{cm^{-3}}$, $N_{\mathrm{CCN},\,0.26\%}$ features concentrations around $250\,\mathrm{cm^{-3}}$. In contrast, close to the measured clouds at 52380 and 52520 seconds of day $N_{\mathrm{CCN},\,0.26\%}$ exceeds values of $600\,\mathrm{cm^{-3}}$, when ACTOS was measuring close to cloud top. Since $N_{\mathrm{CCN},\,0.26\%}$ drops towards

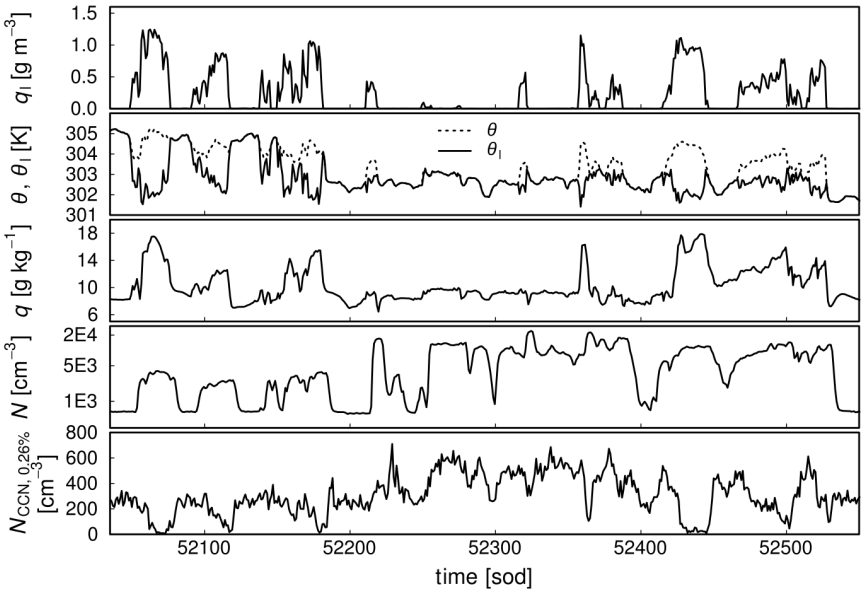

Figure 5.9: Time series of liquid water content q_l, potential (and liquid potential) temperature θ (θ_l), specific humidity q, particle number concentration N and CCN concentration $N_{CCN,\,0.26\%}$ during a horizontal leg at cloud level over the west coast of Barbados during research flight #25. The complete time series corresponds to a flight distance of approximately 10 km.

zero inside the clouds, one can expect droplet number concentrations larger than 600 cm^{-3}. For technical reasons, cloud droplet number concentration can not be calculated for this research flight.

5.2.3 Particle number size distributions

In Fig. 5.10 particle number size distributions are plotted. The blue NSDs were measured in the well-mixed layer below 600 m during research flight #25 (blue), black NSDs refer to the same research flight and were obtained at cloud level at approximately 1750 ± 100 m height during the same time period as shown in Fig. 5.9. Red NSDs were also obtained at cloud level at approximately 1700 ± 100 m height during research flight #26.

The NSDs at cloud level illustrate nicely the origin of the large particle number concentration. They show an overall higher number concentration also for larger particle diameters, which is typical for anthropogenic pollution (e.g., *Wehner and Wiedensohler*, 2003; *Hussein et al.*, 2004). Additionally, the NSDs feature a very pronounced nucleation mode (particles smaller than approximately $D_p = 30$ nm), which probably results from gas to particle conversion of anthropogenic emissions. Furthermore, the NSDs measured during research flight #26 (afternoon flight) exhibit higher concentrations than during research flight #25. De-

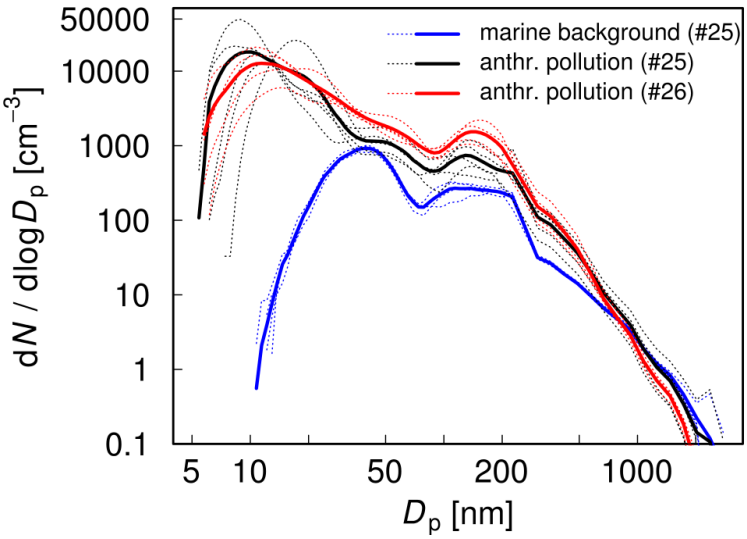

Figure 5.10: Particle number size distributions of the maritime background (blue, measured during research flight #25), the local pollution before noon (black, measured during research flight #25) and the local pollution in the afternoon (red, measured during research flight #26). Thick lines indicate mean size distributions.

spite the dominating high particle number concentration in the nucleation and Aitken mode, there is still a distinct minimum at approximately $D_\mathrm{p} = 95\,\mathrm{nm}$. For marine particle number size distributions, this minimum is associated with the so-called Hoppel minimum. In this particular case, the location of this minimum is probably also influenced by the pollution particles. Nevertheless, assuming that the minimum develops, such as the Hoppel minimum, by mass aggregation in the droplet phase, then the minimum gives information on the activation diameter. Since the minima of the polluted NSDs are increased compared to the Hoppel minimum of the marine NSDs, one could conclude that the activation diameter is also increased for polluted clouds. Possible reasons for such an increase in the activation diameter and the coinciding decrease in the critical supersaturation needed to activate particles of that size are: decreasing vertical wind velocity and, (more likely) the increased particle number concentration probably combined with a change in the particle hygroscopicity.

5.2.4 Impact on cloud droplet number concentration

For technical reasons, there are no cloud droplet number concentration data available for the research flights #25 and #26. Therefore, the effects of the increased particle number concentration and changed particle hygroscopicity, associated with the local anthropogenic pollution particles, on the cloud droplet number concentration are investigated with the help of the cloud microphysical parcel model by *Simmel and Wurzler* (2006) (see Sec. 2.5).

Each of the different particle number size distributions presented in Fig. 5.10 is represented in the model by three log-normal fits. The particle hygroscopicity of the marine aerosol particles is defined by the average particle hygroscopicity derived from ground-based measurements during $\text{CARRIBA}_{\text{wet}}$ and $\text{CARRIBA}_{\text{dry}}$ ($\kappa_{\text{marine}} = 0.7$).
Since ACTOS is not equipped with instruments to measure the chemical particle composition, the particle hygroscopicity of the pollution particles has to be estimated from literature. In general, particles originating from anthropogenic pollution are supposed to be significantly less hygroscopic. Likely, the aerosol plume over the west coast of Barbados is influenced by traffic. *Jurányi et al.* (2013) investigated the hygroscopicity of urban aerosol particles close to Paris and found κ-values between 0.1 and 0.28. Furthermore, the observed clouds were probably influenced by local fires. *Rose et al.* (2010) derived κ-values between 0.1–0.3 for biomass-burning events in China. Similar results were obtained by *Lathem et al.* (2013) based on airborne measurements of arctic and Canadian biomass-burning aerosol particles. To capture the range of these measurements, different model runs were performed with two different κ-values: $\kappa_{\text{poll}\,1} = 0.1$ and, $\kappa_{\text{poll}\,2} = 0.35$.
The cloud microphysical parcel model is initialized with: $T = 21°\text{C}$, $p = 900\,\text{hPa}$, $q = 17\,\text{g}\,\text{kg}^{-1}$ and a relative humidity of $rH = 92\%$. In the first model step, the particle number size distribution is calculated for ambient humidity. Similar to the above case study, the model is run for different fixed updraft velocities ranging between $0.5–5\,\text{m}\,\text{s}^{-1}$.
Figure 5.11 shows the average modeled cloud droplet number concentrations for different vertical wind velocities and the different particle number size distributions. For the marine particle number size distribution (left panel of Fig. 5.11), N_{d} ranges between $180\,\text{cm}^{-3}$ (for $w = 0.5\,\text{m}\,\text{s}^{-1}$) and $450\,\text{cm}^{-3}$ (for $w = 5\,\text{m}\,\text{s}^{-1}$).
The mid panel of Fig. 5.11 shows the average N_{d} calculated for the polluted NSDs during research flight #25 for two different κ-values. Depending on κ, the mean N_{d} varies between $250\,\text{cm}^{-3}$ and $800\,\text{cm}^{-3}$. For the afternoon flight conditions (research flight #26), a further increase up to $1100\,\text{cm}^{-3}$ is recognized. The error bars refer to the minimum and maximum values calculated for the different NSDs and represent the variability in the aerosol particle properties.

5.2.5 Conclusions

In contrast to the case study in Sec. 5.1, where the large scale advection of particles from the African continent influenced the particle properties over Barbados, the here introduced case study shows a scenario of very localized anthropogenic pollution.
Isolated fires in the North of the island as well as anthropogenic pollution over the capital of Barbados lead to an increase in N by one order of magnitude. The NSDs show that most of

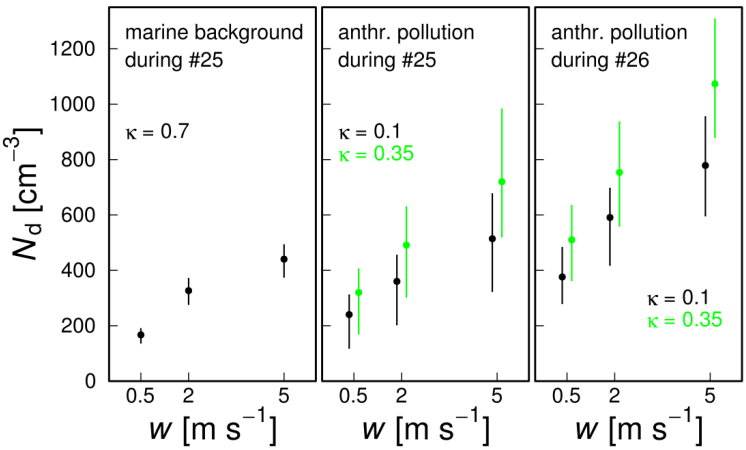

Figure 5.11: Average modeled cloud droplet number concentration for different updraft velocities (0.5, 2, 5 m s^{-1}) and different initial particle number size distributions representing the marine NSDs (left panel) and the pollution particles during research flight #25 (middle panel) and #26 (right panel). For the pollution particles the model was run with two different particle hygroscopicity values: $\kappa_{\mathrm{poll\,1}} = 0.1$ (black) and $\kappa_{\mathrm{poll\,2}} = 0.35$ (green). The error bars represent the minimum and maximum values resulting from the initialization with the different NSDs (dotted lines in Fig. 5.10).

the particle number concentration increase is caused by particles smaller than $D_{\mathrm{p}} = 30\,\mathrm{nm}$. Nevertheless, for larger particles the concentration increases as well, leading to an increase of $N_{\mathrm{CCN,\,0.26\%}}$ by a factor of three. This increase for larger particles is more pronounced for the second research flight on that day, which may result from particle accumulation and/or coagulation and particle growth by condensation.

Because of the high total particle number concentration and the shape of the NSDs for the pollution particles, N_{d} is expected to be more sensitive towards changes in the particle hygroscopicity than in the case study in Sec. 5.1 (see conclusions of section 4.6). Therefore, the different particle hygroscopicity of the marine and pollution particles are taken into account in the performed model calculations. The modeled cloud droplet number concentrations inside the pollution plumes exceed the calculated N_{d} for the marine background case by more than a factor of two (compare e.g., results for 2 m s^{-1} of research flights #25 and #26).

Due to the very localized particle sources, the spatial variability of N and the NSDs is extremely high which is illustrated in the approximately 10 km long time series shown in Fig. 5.9. This is also reflected by the large error bars in the parcel model results. In comparison to the average particle number size distributions observed during CARRIBA$_{\mathrm{wet}}$ and CARRIBA$_{\mathrm{dry}}$, the NSDs measured inside the pollution plumes represent outstanding particle properties and a very effective particle number concentration source. Thus on local

scales, the local anthropogenic pollution is able to alter significantly the droplet number concentration of trade wind cumuli.

Chapter 6

Summary

Within the scope of this dissertation, a fundamental characterization of the average microphysical properties of aerosol particles in the trade wind regime and their variability including cases of natural and anthropogenic pollution is presented. On this basis, the sensitivity of the number concentration of activated particles and the cloud droplet number concentration of trade wind cumuli towards changes in the aerosol particle properties are investigated using in-situ observations and model calculations. Both, the observations and model results imply high sensitivities of trade wind cumuli towards changes in the aerosol particle number concentration (particularly in the accumulation mode) close to the physically meaningful maximum.

The findings of this dissertation are based on measurements performed by the helicopter-borne measurement platform ACTOS (Airborne Cloud Turbulence Observation System, see *Siebert et al.*, 2006b). ACTOS is an autonomous platform carried by means of a 140 m long kevlar cable beneath a helicopter. Its true air speed of $20\,\mathrm{m\,s^{-1}}$ allows for measurements on the decimeter scale for selected meteorological parameters. Within the scope of this dissertation, measurements performed during the CARRIBA (Clouds, Aerosols, Radiation and tuRbulence in the trade wind regime over BArbados) experiment (*Siebert et al.*, 2013) are analyzed. Two intensive measurement periods were carried out in November 2010 and April 2011, including 31 research flights close to the easternmost Caribbean island — Barbados.

As a basis for the analysis, the microphysical properties of aerosol particles in the trade wind regime are investigated. The observed aerosol particle number size distributions during the two campaigns exhibit mainly bimodal structures with a distinct minimum at approximately $D_\mathrm{p} \approx 80\,\mathrm{nm}$, which is characteristic for marine aerosol particles (e.g., *Hoppel et al.*, 1986). The flight-averaged integral particle number concentration shows moderate variability between 100–1000 $\mathrm{cm^{-3}}$, which is generally much lower compared to continental European particle number concentrations (in the order of several thousands per cubic centimeter, cf. e.g.,

Neusüß, 2002, *Hamburger et al.*, 2012). Beside measurements of the total aerosol particle spectrum, one key aspect of this study is to concentrate on activated aerosol particles inside individual trade wind cumulus clouds. Here, a method is presented to derive the number of activated particles, the corresponding activation diameter and the necessary critical supersaturation from measurements of the interstitial and total aerosol particles. So, a unique dataset is created, covering almost 700 individual clouds and providing the first estimates of activation diameter and critical supersaturation inside trade wind cumulus clouds. A comprehensive statistical analysis for the 30% most active clouds (defined by the joint probability density function of liquid water content and updraft velocity) measured by ACTOS reveals activation diameters ranging within 40–180 nm and corresponding critical supersaturations up to 0.9%. There are only a few studies available, which provide aerosol-derived estimates about the critical supersaturation inside of clouds. Recent studies based on ground-based measurements at the high-alpine site Jungfraujoch (*Hammer et al.*, 2014) and Puy-de-Dôme high altitude site in France (*Asmi et al.*, 2012) show slightly lower supersaturation values.

Furthermore, the introduced statistical analysis for the 30% most active clouds clearly identifies major factors affecting the cloud droplet number concentration: (1) the vertical wind velocity inside the clouds and, (2) the CCN (cloud condensation nuclei) number concentration. Additionally, this study presents the first $\mathrm{ACI_N}$ metrics (the change in cloud microphysical properties with a change in aerosol particle number concentration) (*Feingold and Remer*, 2001) of trade wind cumuli based on airborne in-situ measurements. The derived values are close to the physical meaningful maximum of unity, proving that trade wind cumuli are as sensitive towards changes in N as stratiform clouds in the eastern Pacific (*Painemal and Zuidema*, 2013).

However, the statistical analysis is limited to cases, where the method to derive the number of activated particles is applicable. Therefore, a sensitivity study using the cloud microphysical parcel model of *Simmel and Wurzler* (2006) is carried out to calculate the sensitivity of trade wind cumuli towards changes in the particle number size distribution and hygroscopicity covering the whole range of observations during the measurement campaigns. The sensitivity study affirms that the droplet number concentration of trade wind cumuli is most sensitive towards changes of the particle number concentration rather than the updraft velocity, which agrees qualitatively with the observations. To quantify this sensitivity, the so-called susceptibility ($\zeta(N) = \frac{\delta \ln N_\mathrm{d}}{\delta \ln N}$) is calculated. The susceptibility is highest for accumulation mode dominated particle size distributions ($\zeta(N) \approx 0.9$) and decreases towards ≈ 0.6 if 90% of all particles are located in the Aitken mode size range. In contrast, the susceptibility of the droplet number concentration towards changes in the particle hygroscopicity is significantly lower (< 0.2), which underlines, that cloud microphysical properties are more sensitive to

changes in the physical particle properties than e.g., chemical particle composition (e.g., *Dusek et al.*, 2006). Nevertheless, in cases of Aitken mode dominated particle number size distributions, high total particle number concentration (e.g., higher than 800 cm^{-3}) and low updraft velocity, the susceptibility towards changes in particle hygroscopicity increases up to 0.4. Qualitatively, this is also in agreement with findings of *Ward et al.* (2010), who postulate that the sensitivity of the droplet number concentration towards changes in the aerosol composition can be predicted from the particle number size distribution and vertical wind velocity.

The statistical analysis for the 30% most active clouds and the sensitivity study clearly proof the high sensitivity of trade wind cumuli towards changes in the physical properties of the aerosol particles, in particular the particle number size distribution. Therefore, two case studies with significantly increased particle number concentration are presented which embody natural and anthropogenic perturbations of the aerosol particle properties: (1) African particle plume and, (2) local anthropogenic pollution.

Occasionally, Barbados is influenced by African particle plumes and Saharan dust, which is transported over the Atlantic (e.g., *Prospero and Carlson*, 1972; *Smirnov et al.*, 2000; *Reid*, 2002). Within the course of the advection of an African plume in April 2011, the microphysical particle properties were significantly modified compared to the average particle properties. The particle number size distributions show a rather mono-modal distribution (instead of the typical bimodal shape) with increased particle number concentration, which is most-pronounced diameters larger than 100 nm. The shape of the particle number size distributions of the African aerosol mixture is comparable to the accumulation mode dominated aerosol scenarios of the sensitivity study (see Chapter 4.5). Hence, the droplet number concentration is expected to be very sensitive towards changes in the particle number concentration, which proofs that airmasses advected from the African continent are able to substantially alter cloud microphysical properties of trade wind cumuli. In contrast to the particle size distributions influenced by dust, the majority of freshly-generated anthropogenic pollution particles is smaller than approximately 100 nm (e.g., *Wehner and Wiedensohler*, 2003). In the here presented case study, isolated fires in the North of Barbados and local pollution over the capital city Bridgetown lead to an increase of the total particle number concentration by more than one order of magnitude. The measurements of the particle number size distributions show an increase for the entire particle size range and, additionally, a very pronounced nucleation mode, representing outstanding particle properties compared to the average marine conditions. Model results based on the observed particle properties of the polluted and marine conditions reveal an increase of cloud droplet number concentrations by a factor of two caused by local anthropogenic pollution.

Key aspects within the scope of this dissertation are the characterization of the microphysical aerosol particle properties in the trade wind regime and, the quantification of the sensitivity of the microphysical properties of trade wind cumulus clouds towards changes in the aerosol particle properties. Thereby, a unique dataset is presented, which may serve as a basis for model studies concerning aerosol-cloud interactions. In particular, the presented findings concerning the sensitivity of the droplet number concentration towards changes in the particle number size distributions may help to evaluate the predicted sensitivity by climate models and reduce the uncertainties in climate sensitivity estimates. Finally, the derived aerosol-cloud interaction metrics can be used as basis for observationally-based radiative forcing estimates, in order to validate radiative forcing estimates of climate models.

Appendix A

Köhler Theory

For homogeneous nucleation the saturation vapor pressure $e_{\mathrm{s}}(r)$ over a curved surface of a spherical droplet with radius r, surface tension σ and density ρ_{L} at temperature T is given by Kelvin's Law:

$$e_{\mathrm{s}}(r) = e_{\mathrm{s}}(\infty) \exp\left(\frac{2\sigma}{r R_{\mathrm{v}} \rho_{\mathrm{L}} T}\right) , \tag{A.1}$$

where $e_{\mathrm{s}}(\infty)$ is the saturation vapor pressure over a plain surface of pure water and R_{v} denotes the gas constant of water vapor. Equation A.1 shows an exponential increase of saturation vapor pressure for decreasing values of droplet radius (r). Dissolved substances tend to decrease saturation vapor pressure over liquids. This reduction is described by Raoult's law:

$$\frac{e'}{e_{\mathrm{s}}(\infty)} = \frac{n_0}{n + n_0} , \tag{A.2}$$

where e' is the saturation vapor pressure over a solution of n solute and n_0 water molecules. Assuming $n \ll n_0$ for a diluted solution and ionic dissociation of the solute Eq. A.2 can be expressed by following equation (see *Rogers and Yau*, 1989, p. 87):

$$\frac{e'}{e_{\mathrm{s}}(\infty)} = 1 - \frac{b_{\mathrm{R}}}{r^3} , \tag{A.3}$$

where $b_{\mathrm{R}} = 3 i m_{\mathrm{v}} M/(4\pi\rho_{\mathrm{L}} m_{\mathrm{s}})$ and M indicates the mass of the solute and m_{s} and m_{v} are the molecular masses of solute and water. Combining Kelvin and Raoult effects (Eq. A.1 and Eq. A.3) leads to an equation for the saturation vapor of a solution droplet:

$$\frac{e'_s}{e_s(\infty)} = \left[1 - \frac{b_{\mathrm{R}}}{r^3}\right] e^{a_{\mathrm{K}}/r} , \tag{A.4}$$

where $a_K = 2\sigma/(\rho_L R_v T)$. For not too small radii, this equation can be approximated to the so-called Köhler equation:

$$\frac{e'_s}{e_s(\infty)} = 1 + \frac{a_K}{r} - \frac{b_R}{r^3}\,. \tag{A.5}$$

During the last years the original Köhler theory was subject to further refinements to account for e.g., insoluble particle fractions or for simplification (e.g., *Khvorostyanov and Curry*, 2007; *Petters and Kreidenweis*, 2007; *Wex et al.*, 2007).

A.1 κ-Köhler theory

In this work, the κ-Köhler theory is used to calculate so-called Köhler curves showing the equilibrium supersaturation S as function of the diameter D of a solution droplet (see *Petters and Kreidenweis*, 2007):

$$S(D) = \frac{D^3 - D_{dry}^3}{D^3 - D_{dry}^3(1-\kappa)} \exp\left(\frac{4\sigma_{s/a} M_w}{RT\rho_w D}\right), \tag{A.6}$$

whereby D_{dry}, κ, $\sigma_{s/a}$, M_w, R, T and ρ_w denote the volume equivalent dry diameter, the hygroscopicity parameter, the surface tension of the solution air interface, the molecular weight of water, the universal gas constant, the temperature and density of water.

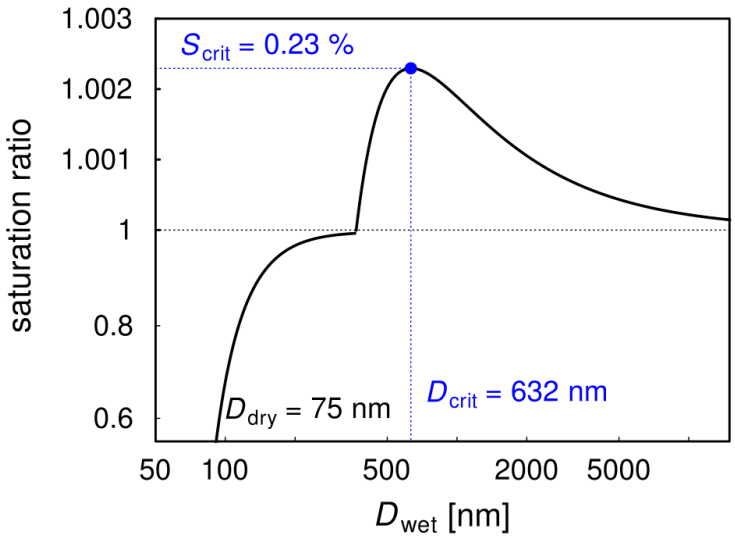

Figure A.1: Equilibrium supersaturation ratio $e'_s/e_s(\infty)$ for different wet diameter (D_{wet}) of a particle with a dry diameter of $D_{dry} = 75\,\text{nm}$ and $\kappa = 0.7$.

Figure A.1 shows the so-called Köhler curve, meaning the equilibrium saturation ratio ($e'_s/e_s(\infty)$) for different wet diameters (D_{wet}) of a particle with a dry diameter of $D_{dry} = 75\,\text{nm}$ and $\kappa = 0.7$.

With the help of size-segregated CCN measurements pairs of activation diameter ($D_{\mathrm{p,\,act}}$) and critical supersaturation (S_{crit}) can be estimated. For those pairs the hygroscopicity parameter κ is calculated as follows (see *Petters and Kreidenweis* (2007)):

$$\kappa = \frac{4A^3\ \sigma^3_{\mathrm{s/a}}(T)}{27\ T^3\ D^3_{\mathrm{p,\,act}}\ \ln^2 S_{\mathrm{crit}}}\,, \tag{A.7}$$

where $A\ =\ 8.69251\,\mathrm{x}\,10^{-6}\,\mathrm{K\,m^3\,J^{-1}}$.

Appendix B

Modified conductivity and diffusivity

In Sec. 2.5 the spectral cloud microphysical parcel model of *Simmel and Wurzler* (2006) is introduced. In Eq. 2.2 a modified version of the conductivity (K^*) and diffusivity (D^*) is used, which is calculated following (from *Simmel and Wurzler* (2006)):

$$K^* = K\left[\frac{K}{\alpha_{\mathrm{T}} c_{\mathrm{p}} \rho_{\mathrm{air}}}\sqrt{\frac{2\pi}{R_{\mathrm{dry}} T}}\frac{1}{r} + \frac{r}{r + d_{\mathrm{T}}}\right]^{-1}, \tag{B.1}$$

$$D^* = D\left[\frac{D}{\alpha_{\mathrm{C}}}\sqrt{\frac{2\pi}{R_{\mathrm{v}} T}}\frac{1}{r} + \frac{r}{r + d_{\mathrm{v}}}\right], \tag{B.2}$$

with conductivity (K) and diffusivity (D):

$$K = 418.510^{-5}(5.69 + 0.017(T - 273.15)), \tag{B.3}$$

$$D = 4.01221^{-5}\frac{T^{1.94}}{p}, \tag{B.4}$$

where α_{T} and α_C are the thermal and water accomodation coefficients, c_{p} is the specific heat capacity of air, R_{dry} the gas constant of dry air, p the air pressure, d_{T} and d_{v} the thermal and vapor jump length.

Appendix C

Research Flights during CARRIBA

Table C.1: Research flights during November 2010, Barbados is located in time zone UTC-4h.

Flight No	Date [yyyy-mm-dd]	Start [UTC] [hh:mm]	Landing [UTC] [hh:mm]	Duration [h:mm]
#01	2010-11-12	14:17	15:38	1:21
#02	2010-11-12	18:51	20:27	1:36
#03	2010-11-13	13:14	14:37	1:22
#04	2010-11-13	17:45	19:23	1:38
#05	2010-11-14	17:26	18:55	1:29
#06	2010-11-15	14:07	15:40	1:33
#07	2010-11-16	14:43	15:54	1:11
#08	2010-11-20	16:52	18:40	1:48
#09	2010-11-21	13:30	15:21	1:51
#10	2010-11-21	18:45	20:46	2:01
#11	2010-11-22	13:53	15:44	1:50
#12	2010-11-23	13:32	15:34	2:01
#13	2010-11-24	13:29	15:25	1:56
#14	2010-11-25	13:31	15:24	1:53
#15	2010-11-26	14:00	15:47	1:47
#16	2010-11-27	13:31	15:26	1:55

Table C.2: Research flights during April 2011, Barbados is located in time zone UTC-4h.

Flight No	Date [yyyy-mm-dd]	Start [UTC] [hh:mm]	Landing [UTC] [hh:mm]	Duration [h:mm]
#17	2011-04-09	13:30	15:08	1:38
#18	2011-04-10	13:44	15:29	1:45
#19	2011-04-13	13:47	15:28	1:41
#20	2011-04-14	13:53	15:46	1:53
#21	2011-04-14	19:35	21:35	2:00
#22	2011-04-15	13:41	15:24	1:43
#23	2011-04-16	13:39	15:23	1:44
#24	2011-04-18	13:44	15:29	1:45
#25	2011-04-19	13:04	14:47	1:43
#26	2011-04-19	18:30	20:23	1:53
#27	2011-04-20	14:27	16:21	1:54
#28	2011-04-22	13:29	15:22	1:53
#29	2011-04-23	13:27	15:24	1:57
#30	2011-04-24	14:13	16:07	1:54
#31	2011-04-25	13:50	15:42	1:52

Appendix D

Normalization of the liquid water content

Since the cloud base and air temperature in the marine boundary layer off the coast of Barbados does not vary significantly (see Sec. 3.2), vertical profiles of the adiabatic liquid water content should also not vary by much from research flight to research flight. Therefore, the q_l measurements of all research flights are used to calculate representative values for the maximum q_l. Here the 95th percentile is determined for 100 m altitude bins.
Figure D.1 shows the calculated 95th percentile of q_l (black circles). The red line indicates an exponential fit and the shaded area denotes the adiabatic liquid water content values for cloud base heights h_cb between 450 m and 650 m and cloud base temperatures T_cb between 21°C and 24°C (which is representative for both CARRIBA campaigns).
Finally, $q_{\mathrm{l},\,95\%}(z)$ is calculated by applying an exponential to all single $q_{\mathrm{l},\,95\%}$ values. The normalized liquid water content is calculated in the following way: $q_\mathrm{l,norm}(z) = \frac{q_\mathrm{l}(z)}{q_{\mathrm{l},\,95\%}(z)}$.
For the lowermost 900 m $q_{\mathrm{l},\,95\%}$ behaves linear and is close to adiabatic prediction. At higher altitudes the agreement gets worse. Therefore, in this analysis, $q_{\mathrm{l},\,95\%}(z)$ is used to normalize q_{rml} instead of the adiabatic q_l.

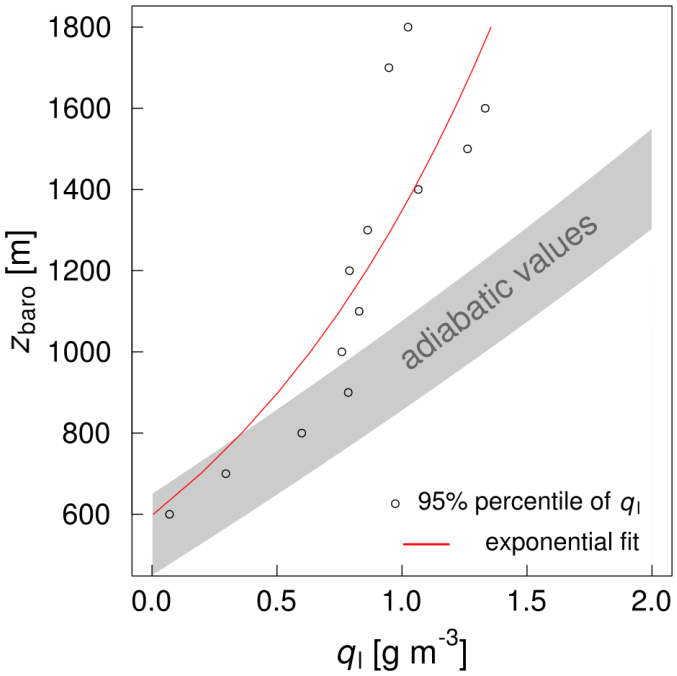

Figure D.1: Calculated 95th percentile of q_l (black circles). The red line indicates an exponential fit and the shaded area denotes the adiabatic liquid water content calculated for different cloud base heights and cloud base temperature T_{cb}.

Appendix E

Passing rate for different filter criteria

Figure E.1 shows a contour plot of the fraction of clouds passing the filter criteria (passing rate) for different values of the normalized liquid water content ($q_{\mathrm{l,\,norm}}$, ordinate) and 90th percentile of the vertical wind velocity (w_{90}, abscissa). The technical filters (N_{act}/N, Δt) are fixed.

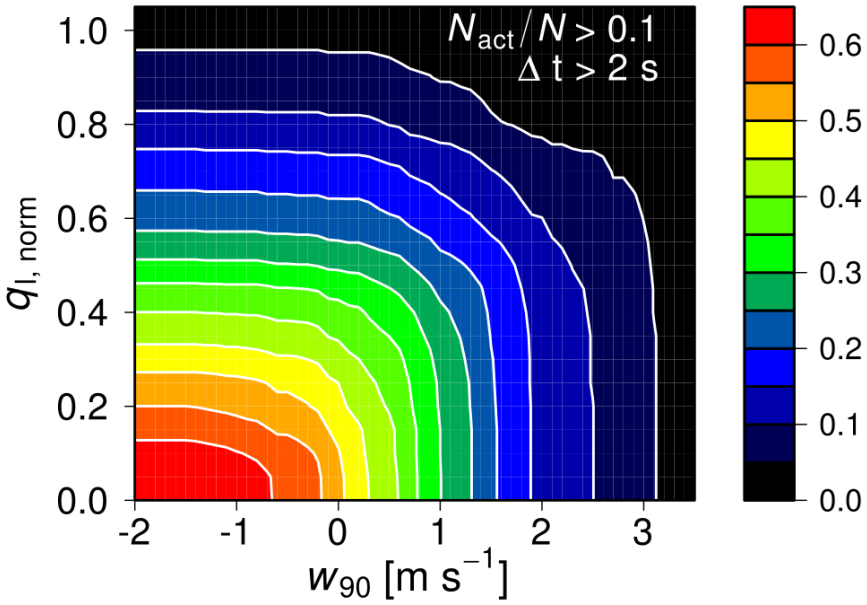

Figure E.1: Contour plot of the fraction of clouds passing the filter criteria for normalized liquid water content ($q_{\mathrm{l,\,norm}}$, ordinate) and 90th percentile of the vertical wind velocity (w_{90}).

The contour lines show a decreasing passing rate for increasing $q_{l,\,norm}$ and w_{90}. Their shape (hitting abscissa and ordinate perpendicularly) indicates that an increase in one filter is immediately followed by an increase in the other, pointing towards a strong dependence of both. The filter criteria are chosen to select the 30% most active clouds.

Appendix F

FLEXPART

In Sec. 5.1 the source region of the aerosols observed over Barbados is investigated with the help of the Lagrangian particle dispersion model FLEXPART. Lagrangian particle models compute trajectories of a large number of so-called particles (not necessarily representing real particles, but infinitesimally small air parcels) to describe the transport and diffusion of tracers in the atmosphere (*Stohl et al.*, 2005).

FLEXPART can simulate long-range and mesoscale transport, diffusion, dry and wet deposition, and radioactive decay of tracers released from point, line, area or volume sources (*Stohl et al.*, 2005). The model parameterizes turbulence in the boundary layer and in the free troposphere by solving Langevin equations. To account for convection, a parameterization scheme is used which is based on the buoyancy sorting principle (*Stohl and Thomson*, 1999; *Stohl et al.*, 2005).

The lidar group at TROPOS has implemented FLEXPART on an own server which allows extensive model runs. The model is driven by global model-level data. We use the archived meteorological data from the NCEP FNL (National Centers for Environmental Prediction final analysis) Global Tropospheric Analyses with a temporal resolution of 6 hours (00, 06, 12, 18 UTC) and a horizontal resolution of $1^\circ \times 1^\circ$. The FNL data are provided by the CISL (Computational & Information Systems Laboratory) Research Data Archive which is managed by NCAR's (National Center for Atmospheric Research) data support section (see http://rda.ucar.edu/datasets/ds083.2/, last check on 3 December, 2013).

Particles are transported both by the resolved winds and by parameterized subgrid motions. The procedures to calculate dry and wet deposition, radioactive decay and gravitational settling of particulate matter were not used in this study.

Bibliography

Albrecht, B. (1989), Aerosols, cloud microphysics, and fractional cloudiness, *Science*, *245*(4923), 1227–1230.

Ansmann, A., M. Riebesell, U. Wandinger, C. Weitkamp, E. Voss, W. Lahmann, and W. Michaelis (1992), Combined Raman elastic-backscatter lidar for vertical profiling of moisture, aerosol extinction, backscatter, and lidar ratio, *Appl. Phys. B*, *B55*, 18–28.

Ansmann, A., P. Seifert, M. Tesche, and U. Wandinger (2012), Profiling of fine and coarse particle mass: case studies of Saharan dust and Eyjafjallajökull/Grimsvötn volcanic plumes, *Atmos. Chem. Phys.*, *12*(20), 9399–9415, doi:10.5194/acp-12-9399-2012.

Asmi, E., E. Freney, M. Hervo, D. Picard, C. Rose, A. Colomb, and K. Sellegri (2012), Aerosol cloud activation in summer and winter at puy-de-Dôme high altitude site in France, *Atmos. Chem. Phys.*, *12*(23), 11589–11607, doi:10.5194/acp-12-11589-2012.

Baron, P. A., and K. Willeke (2001), *Aerosol Measurements: Principles Techniques and Applications*, 1131 pp., John Wiley and Sons, New York.

Betts, A. K. (1973), Non-precipitating cumulus convection and its parameterization, *Q. J. R. Meteorol. Soc.*, *99*(419), 178–196, doi:10.1002/qj.49709941915.

Brenguier, J., P. Chuang, and Y. Fouquart (2000), An overview of the ACE-2 CLOUDYCOLUMN closure experiment, *Tellus B*, *52*(2), 815–827, doi:10.1034/j.1600-0889.2000.00047.x.

Chuang, P. Y., E. W. Saw, J. D. Small, R. A. Shaw, C. M. Sipperley, G. A. Payne, and W. D. Bachalo (2008), Airborne Phase Doppler Interferometry for Cloud Microphysical Measurements, *Aerosol Sci. Technol.*, *42*(8), 685–703, doi:10.1080/02786820802232956.

Colón-Robles, M., R. M. Rauber, and J. R. B. Jensen (2006), Influence of low-level wind speed on droplet spectra near cloud base in trade wind cumulus, *Geophys. Res. Lett.*, *33*(20), 1–6, doi:10.1029/2006GL027487.

Conant, W. C. (2004), Aerosol-cloud drop concentration closure in warm cumulus, *J. Geophys. Res.*, *109*(D13), 1–12, doi:10.1029/2003JD004324.

Denman, K., G. Brasseur, A. Chidthaisong, P. Ciais, P. Cox, R. Dickinson, D. Hauglustaine, C. Heinze, E. Holland, D. Jacob, U. Lohmann, S. Ramachandran, P. da Silva Dias, S. Wofsy, and X. Zhang (2007), *Couplings Between Changes in the Climate System and Biogeochemistry. In: Climate Change 2007: The Physical Science Basis. Contribution of*

Working Group I to the Fourth Assessment Report of the Intergovernmental Panel on Climate Change, Cambridge University Press, Cambridge, United Kingdom and New York, NY, USA.

Dusek, U., G. P. Frank, L. Hildebrandt, J. Curtius, J. Schneider, S. Walter, D. Chand, F. Drewnick, S. Hings, D. Jung, S. Borrmann, and M. O. Andreae (2006), Size matters more than chemistry for cloud-nucleating ability of aerosol particles., *Science*, *312*(5778), 1375–8, doi:10.1126/science.1125261.

Feingold, G. (2003), Modeling of the first indirect effect: Analysis of measurement requirements, *Geophys. Res. Lett.*, *30*(19), 1997, doi:10.1029/2003GL017967.

Feingold, G., and L. Remer (2001), Analysis of smoke impact on clouds in Brazilian biomass burning regions: An extension of Twomey's approach, *J. Geophys. Res.*, *106*(NO. D19), 22,907 – 22,922.

Freudenthaler, V., M. Esselborn, M. Wiegner, B. Heese, M. Tesche, A. Ansmann, D. Müller, D. Althausen, M. Wirth, A. Fix, G. Ehret, P. Knippertz, C. Toledano, J. Gasteiger, M. Garhammer, and M. Seefeldner (2009), Depolarization ratio profiling at several wavelengths in pure Saharan dust during SAMUM 2006, *Tellus B*, *61*(1), 165–179, doi:10.1111/j.1600-0889.2008.00396.x.

Fuchs, N. (1963), On the stationary charge distribution on aerosol particles in a bipolar ionic atmosphere, *Geofis. pura e Appl.*, (2).

Garrett, T. J., L. F. Radke, and P. V. Hobbs (2002), Aerosol Effects on Cloud Emissivity and Surface Longwave Heating in the Arctic, *J. Atmos. Sci.*, *59*(3), 769–778, doi:10.1175/1520-0469(2002)059⟨0769:AEOCEA⟩2.0.CO;2.

Gerber, H. (1991), Direct measurement of suspended particulate volume concentration and far-infrared extinction coefficient with a laser-diffraction instrument., *Appl. Opt.*, *30*(33), 4824–31.

Groß, S., M. Esselborn, B. Weinzierl, M. Wirth, A. Fix, and A. Petzold (2013), Aerosol classification by airborne high spectral resolution lidar observations, *Atmos. Chem. Phys.*, *13*(5), 2487–2505, doi:10.5194/acp-13-2487-2013.

Guibert, S., J. Snider, and J. Brenguir (2003), Aerosol activation in marine stratocumulus clouds: 1. Measurement validation for a closure study, *J. Geophys. Res.*, *108*(D15), 1–17, doi:10.1029/2002JD002678.

Gunn, R. (1956), The hyperelectrification of raindrops by atmospheric electric fields, *J. Meteorol.*, *13*.

Hagen, D., and D. Alofs (1983), Linear inversion method to obtain aerosol size distributions from measurements with a differential mobility analyzer, *Aerosol Sci. Technol.*, *2:4*, 465–475, doi:http://dx.doi.org/10.1080/02786828308958650.

Hamburger, T., G. McMeeking, A. Minikin, A. Petzold, H. Coe, and R. Krejci (2012), Airborne observations of aerosol microphysical properties and particle ageing processes in the troposphere above Europe, *Atmos. Chem. Phys*, *12*, 11533–11554, doi:10.5194/acp-12-11533-2012.

Hammer, E., N. Bukowiecki, M. Gysel, Z. Jurányi, C. R. Hoyle, R. Vogt, U. Baltensperger, and E. Weingartner (2014), Investigation of the effective peak supersaturation for liquid-phase clouds at the high-alpine site Jungfraujoch, Switzerland (3580 m a.s.l.), *Atmos. Chem. Phys.*, *14*(2), 1123–1139, doi:10.5194/acp-14-1123-2014.

Haywood, J. M., J. Pelon, P. Formenti, N. Bharmal, M. Brooks, G. Capes, P. Chazette, C. Chou, S. Christopher, H. Coe, J. Cuesta, Y. Derimian, K. Desboeufs, G. Greed, M. Harrison, B. Heese, E. J. Highwood, B. Johnson, M. Mallet, B. Marticorena, J. Marsham, S. Milton, G. Myhre, S. R. Osborne, D. J. Parker, J.-L. Rajot, M. Schulz, A. Slingo, D. Tanré, and P. Tulet (2008), Overview of the Dust and Biomass-burning Experiment and African Monsoon Multidisciplinary Analysis Special Observing Period-0, *J. Geophys. Res.*, *113*(October), 1–20, doi:10.1029/2008JD010077.

Hermann, M., B. Wehner, O. Bischof, H.-S. Han, T. Krinke, W. Liu, A. Zerrath, and A. Wiedensohler (2007), Particle counting efficiencies of new TSI condensation particle counters, *J. Aerosol Sci.*, *38*(6), 674–682, doi:10.1016/j.jaerosci.2007.05.001.

Hoppel, W., G. Frick, and R. Larson (1986), Effect of non-precipitating clouds on the aerosol size distribution in the marine boundary layer, *Geophys. Res. Lett.*, *13*(2), 125–128.

Hudson, J. G., and S. Mishra (2007), Relationships between CCN and cloud microphysics variations in clean maritime air, *Geophys. Res. Lett.*, *34*(16), 10–15, doi:10.1029/2007GL030044.

Hussein, T., A. Puustinen, P. P. Aalto, J. M. Mäkelä, K. Hämeri, and M. Kulmala (2004), Urban aerosol number size distributions, *Atmos. Chem. Phys.*, *4*(2), 391–411, doi:10.5194/acp-4-391-2004.

Jung, E., B. Albrecht, J. M. Prospero, H. H. Jonsson, and S. M. Kreidenweis (2013), Vertical structure of aerosols, temperature, and moisture associated with an intense African dust event observed over the eastern Caribbean, *J. Geophys. Res. Atmos.*, *118*(10), 4623–4643, doi:10.1002/jgrd.50352.

Jurányi, Z., T. Tritscher, M. Gysel, M. Laborde, L. Gomes, G. Roberts, U. Baltensperger, and E. Weingartner (2013), Hygroscopic mixing state of urban aerosol derived from size-resolved cloud condensation nuclei measurements during the MEGAPOLI campaign in Paris, *Atmos. Chem. Phys.*, *13*(13), 6431–6446, doi:10.5194/acp-13-6431-2013.

Kaaden, N., A. Massling, A. Schladitz, T. Müller, K. Kandler, L. Schütz, B. Weinzierl, A. Petzold, M. Tesche, S. Leinert, C. Deutscher, M. Ebert, S. Weinbruch, and A. Wiedensohler (2009), State of mixing, shape factor, number size distribution, and hygroscopic growth of the Saharan anthropogenic and mineral dust aerosol at Tinfou, Morocco, *Tellus B*, *61*(1), 51–63, doi:10.1111/j.1600-0889.2008.00388.x.

Khvorostyanov, V. I., and J. A. Curry (2007), Refinements to the Köhler's theory of aerosol equilibrium radii, size spectra, and droplet activation: Effects of humidity and insoluble fraction, *J. Geophys. Res.*, *112*(D5), 1–20, doi:10.1029/2006JD007672.

Langmuir, I. (1948), The production of rain by a chain reaction in cumulus clouds at temperatures above freezing, *J. Meteorol.*, *5*(5), 175–192.

Lathem, T. L., A. J. Beyersdorf, K. L. Thornhill, E. L. Winstead, M. J. Cubison, A. Hecobian, J. L. Jimenez, R. J. Weber, B. E. Anderson, and A. Nenes (2013), Analysis of CCN activity of Arctic aerosol and Canadian biomass burning during summer 2008, *Atmos. Chem. Phys.*, *13*(5), 2735–2756, doi:10.5194/acp-13-2735-2013.

Mason, B. J. (1971), The physics of clouds, Clarendon.

McComiskey, A., and G. Feingold (2012), The scale problem in quantifying aerosol indirect effects, *Atmos. Chem. Phys.*, *12*(2), 1031–1049, doi:10.5194/acp-12-1031-2012.

Neusüß, C. (2002), Characterization and parameterization of atmospheric particle number-, mass-, and chemical-size distributions in central Europe during LACE 98 and MINT, *J. Geophys. Res.*, *107*(D21), 1–13, doi:10.1029/2001JD000514.

Nuijens, L., I. Serikov, L. Hirsch, K. Lonitz, and B. Stevens (2013), The distribution and variability of low-level cloud in the North-Atlantic trades, *Q. J. R. Meteorol. Soc.*, doi: 10.1002/qj.2307.

Painemal, D., and P. Zuidema (2013), The first aerosol indirect effect quantified through airborne remote sensing during VOCALS-REx, *Atmos. Chem. Phys.*, *13*(2), 917–931, doi: 10.5194/acp-13-917-2013.

Peng, Y. (2002), The cloud albedo-cloud droplet effective radius relationship for clean and polluted clouds from RACE and FIRE.ACE, *J. Geophys. Res.*, *107*(D11), 4106, doi:10. 1029/2000JD000281.

Petters, M. D., and S. M. Kreidenweis (2007), A single parameter representation of hygroscopic growth and cloud condensation nucleus activity, *Atmos. Chem. Phys.*, pp. 1961–1971.

Pfeifer, S., W. Birmili, A. Schladitz, T. Müller, A. Nowak, and A. Wiedensohler (2014), A fast and easy-to-implement inversion algorithm for mobility particle size spectrometers considering particle number size distribution information outside of the detection range, *Atmos. Meas. Tech.*, *7*(1), 95–105, doi:10.5194/amt-7-95-2014.

Politovich, M. (1988), Variability of the supersaturation in cumulus clouds., *J. Atmos. Sci.*

Prospero, J. M., and T. N. Carlson (1972), Vertical and areal distribution of Saharan dust over the western equatorial north Atlantic Ocean, *J. Geophys. Res.*, *77*(27), 5255–5265, doi:10.1029/JC077i027p05255.

Prospero, J. M., and P. J. Lamb (2003), African droughts and dust transport to the Caribbean: climate change implications., *Science*, *302*(5647), 1024–7, doi:10.1126/science. 1089915.

Pruppacher, H. R., and J. D. Klett (1997), *Microphysics of Clouds and Precipitation: With an Introduction to Cloud Chemistry and Cloud Electricity*, 954 pp., Springer, New York.

Rauber, R. M., B. Stevens, H. T. Ochs III, C. Knight, B. A. Albrecht, A. M. Blyth, C. W. Fairall, B. J. Jensen, S. G. Lasher-Trapp, O. L. Mayol-Bracero, G. Vali, J. R. Anderson, B. A. Baker, A. R. Bandy, E. Burnet, J.-L. Brenguier, W. A. Brewer, P. R. A. Brown, P. Chuang, W. R. Cottom, L. D. Girolamo, B. Geerts, H. Gerber, S. Göke, L. Gomes, B. G. Heikes, J. G. Hudson, P. Kollias, R. P. Lawson, S. K. Krueger, D. H. Lenschow, L. Nuijens, D. W. O'Sullivan, R. A. Rilling, D. C. Rogers, A. P. Siebesma, E. Snodgrass, J. L. Stith, D. C. Thornton, S. Tucker, C. H. Twohy, and P. Zuidema (2007), Rain in shallow cumulus over the ocean - The RICO campaign, *Bull. Am. Meteorol. Soc.*, (December 2007).

Reid, J. S. (2002), Dust vertical distribution in the Caribbean during the Puerto Rico Dust Experiment, *Geophys. Res. Lett.*, *29*(7), 1151, doi:10.1029/2001GL014092.

Reutter, P., H. Su, J. Trentmann, M. Simmel, D. Rose, S. S. Gunthe, H. Wernli, M. O. Andreae, and U. Pöschl (2009), Aerosol- and updraft-limited regimes of cloud droplet formation: influence of particle number, size and hygroscopicity on the activation of cloud condensation nuclei (CCN), *Atmos. Chem. Phys.*, *9*(18), 7067–7080, doi: 10.5194/acp-9-7067-2009.

Roberts, G. C., and A. Nenes (2005), A Continuous-Flow Streamwise Thermal-Gradient CCN Chamber for Atmospheric Measurements, *Aerosol Sci. Technol.*, *39*(3), 206–221, doi:10.1080/027868290913988.

Rogers, R. R., and M. K. Yau (1989), *A short course in cloud physics*, 293 pp., Pergamon Press.

Rose, D., A. Nowak, P. Achtert, A. Wiedensohler, M. Hu, M. Shao, Y. Zhang, M. Andreae, and U. Pöschl (2010), Cloud condensation nuclei in polluted air and biomass burning smoke near the mega-city Guangzhou, China - Part 1: Size-resolved measurements and implications for the modeling of aerosol particle hygroscopicity and CCN activity, *Atmos. Chem. Phys.*, pp. 3365–3383.

Sassen, K. (2005), Meteorology: dusty ice clouds over Alaska., *Nature*, *434*(7032), 456, doi: 10.1038/434456a.

Schladitz, A., T. Müller, A. Nowak, K. Kandler, K. Lieke, A. Massling, and A. Wiedensohler (2011), In situ aerosol characterization at Cape Verde, *Tellus B*, *63*(4), 531–548, doi: 10.1111/j.1600-0889.2011.00569.x.

Seinfeld, J. H., and S. N. Pandis (2006), *Atmospheric Chemistry and Physics: From Air Pollution to Climate Change*, 2nd ed., 1232 pp., John Wiley and Sons, New York, New York.

Shaw, R. A., W. C. Reade, and L. R. Collins (1998), Preferential concentration of cloud droplets by turbulence: Effects on the early evolution of cumulus cloud droplet spectra, *J. Atmos. Sci.*, (1993), 1965–1976.

Siebert, H., K. Lehmann, and M. Wendisch (2006a), Observations of small-scale turbulence and energy dissipation rates in the cloudy boundary layer, *J. Atmos. Sci.*, (1962), 1451–1466.

Siebert, H., K. Lehmann, M. Wendisch, H. Franke, R. Maser, D. Schell, E. Wei Saw, and R. A. Shaw (2006b), Probing Finescale Dynamics and Microphysics of Clouds with Helicopter-Borne Measurements, *Bull. Am. Meteorol. Soc.*, *87*(12), 1727–1738, doi: 10.1175/BAMS-87-12-1727.

Siebert, H., M. Beals, J. Bethke, E. Bierwirth, T. Conrath, K. Dieckmann, F. Ditas, A. Ehrlich, D. Farrell, S. Hartmann, M. A. Izaguirre, J. Katzwinkel, L. Nuijens, G. Roberts, M. Schäfer, R. A. Shaw, T. Schmeissner, I. Serikov, B. Stevens, F. Stratmann, B. Wehner, M. Wendisch, F. Werner, and H. Wex (2013), The fine-scale structure of the trade wind cumuli over Barbados - an introduction to the CARRIBA project, *Atmos. Chem. Phys.*, *13*(19), 10061–10077, doi:10.5194/acp-13-10061-2013.

Simmel, M., and S. Wurzler (2006), Condensation and activation in sectional cloud microphysical models, *Atmos. Res.*, *80*(2-3), 218–236, doi:10.1016/j.atmosres.2005.08.002.

Smirnov, A., B. N. Holben, D. Savoie, J. M. Prospero, Y. J. Kaufman, D. Tanre, T. F. Eck, and I. Slutsker (2000), Relationship between column aerosol optical thickness and in situ ground based dust concentrations over Barbados, *Geophys. Res. Lett.*, *27*(11), 1643–1646, doi:10.1029/1999GL011336.

Snider, J. R., and J.-L. Brenguier (2000), Cloud condensation nuclei and cloud droplet measurements during ACE-2, *Tellus B*, *52*(2), 828–842, doi:10.1034/j.1600-0889.2000.00044.x.

Solomon, S., D. Qin, M. Manning, Z. Chen, M. Marquis, K. Averyt, M. Tignor, and H. E. Miller (2007), *Contribution of Working Group I to the Fourth Assessment Report of the Intergovernmental Panel on Climate Change*, 996 pp., Cambridge University Press, Cambridge, United Kingdom and New York, NY, USA.

Stevens, B., and G. Feingold (2009), Untangling aerosol effects on clouds and precipitation in a buffered system., *Nature*, *461*(7264), 607–13, doi:10.1038/nature08281.

Stohl, A., and D. J. Thomson (1999), A Density Correction for Lagrangian Particle Dispersion Models, *Boundary-Layer Meteorol.*, *90*(1), 155–167, doi:10.1023/A:1001741110696.

Stohl, A., M. Hittenberger, and G. Wotawa (1998), Validation of the lagrangian particle dispersion model FLEXPART against large-scale tracer experiment data, *Atmos. Environ.*, *32*(24), 4245–4264.

Stohl, A., C. Forster, A. Frank, P. Seibert, and G. Wotawa (2005), Technical note : The Lagrangian particle dispersion model FLEXPART v6.2, *Atmos. Chem. Phys.*, *2005*, 2461–2474, doi:10.5194/acp-5-2461-2005.

Tesche, M., A. Ansmann, D. Müller, D. Althausen, I. Mattis, B. Heese, V. Freudenthaler, M. Wiegner, M. Esselborn, G. Pisani, and P. Knippertz (2009), Vertical profiling of Saharan dust with Raman lidars and airborne HSRL in southern Morocco during SAMUM, *Tellus B*, *61*(1), 144–164, doi:10.1111/j.1600-0889.2008.00390.x.

Tiedtke, M. (1989), A Comprehensive Mass Flux Scheme for Cumulus Parameterization in Large-Scale Models, *Mon. Weather Rev.*, *117*(8), 1779–1800, doi:10.1175/1520-0493(1989)117⟨1779:ACMFSF⟩2.0.CO;2.

Twomey, S. (1963), Measurements of Natural Cloud Nuclei, *J. Rech. Atmos.*, *1:101-105*.

Twomey, S. (1977), The Influence of Pollution on the Shortwave Albedo of Clouds, *J. Atmos. Sci.*, *34*(7), 1149–1152, doi:10.1175/1520-0469(1977)034⟨1149:TIOPOT⟩2.0.CO;2.

VanReken, T. M. (2003), Toward aerosol/cloud condensation nuclei (CCN) closure during CRYSTAL-FACE, *J. Geophys. Res.*, *108*(D20), 4633, doi:10.1029/2003JD003582.

Wang, H., and G. M. McFarquhar (2008), Modeling aerosol effects on shallow cumulus convection under various meteorological conditions observed over the Indian Ocean and implications for development of mass-flux parameterizations for climate models, *J. Geophys. Res.*, *113*(D20), D20201, doi:10.1029/2008JD009914.

Ward, D. S., T. Eidhammer, W. R. Cotton, and S. M. Kreidenweis (2010), The role of the particle size distribution in assessing aerosol composition effects on simulated droplet activation, *Atmos. Chem. Phys.*, *10*(12), 5435–5447, doi:10.5194/acp-10-5435-2010.

Warner, J., and S. Twomey (1967), The production of cloud nuclei by cane fires and the effect on cloud droplet concentration., *J. Atmos. Sci.*, *24*, 704–706.

Wehner, B., and A. Wiedensohler (2003), Long term measurements of submicrometer urban aerosols: statistical analysis for correlations with meteorological conditions and trace gases, *Atmos. Chem. Phys.*, *3*(3), 867–879, doi:10.5194/acp-3-867-2003.

Werner, F., H. Siebert, P. Pilewskie, T. Schmeissner, R. A. Shaw, and M. Wendisch (2013), New airborne retrieval approach for trade wind cumulus properties under overlying cirrus, *J. Geophys. Res. Atmos.*, *118*(9), 3634–3649, doi:10.1002/jgrd.50334.

Wex, H., T. Hennig, I. Salma, R. Ocskay, A. Kiselev, S. Henning, A. Massling, A. Wiedensohler, and F. Stratmann (2007), Hygroscopic growth and measured and modeled critical super-saturations of an atmospheric HULIS sample, *Geophys. Res. Lett.*, *34*(2), L02818, doi:10.1029/2006GL028260.

Wiedensohler, A., W. Birmili, A. Nowak, A. Sonntag, K. Weinhold, M. Merkel, B. Wehner, T. Tuch, S. Pfeifer, M. Fiebig, A. M. Fjäraa, E. Asmi, K. Sellegri, R. Depuy, H. Venzac, P. Villani, P. Laj, P. Aalto, J. A. Ogren, E. Swietlicki, P. Williams, P. Roldin, P. Quincey, C. Hüglin, R. Fierz-Schmidhauser, M. Gysel, E. Weingartner, F. Riccobono, S. Santos, C. Grüning, K. Faloon, D. Beddows, R. Harrison, C. Monahan, S. G. Jennings, C. D. O'Dowd, A. Marinoni, H.-G. Horn, L. Keck, J. Jiang, J. Scheckman, P. H. McMurry, Z. Deng, C. S. Zhao, M. Moerman, B. Henzing, G. de Leeuw, G. Löschau, and S. Bastian (2012), Mobility particle size spectrometers: harmonization of technical standards and data structure to facilitate high quality long-term observations of atmospheric particle number size distributions, *Atmos. Meas. Tech.*, *5*(3), 657–685, doi:10.5194/amt-5-657-2012.

Willeke, K., and P. A. Baron (1993), *Aerosol Measurement: Principles, Techniques, and Applications*, 876 pp., Van Nostrand Reinhold Publishers, New York, NY.

Wood, R., C. R. Mechoso, C. S. Bretherton, R. A. Weller, B. Huebert, F. Straneo, B. Albrecht, H. Coe, G. Allen, G. Vaughan, P. Daum, C. Fairall, D. Chand, L. Gallardo Klenner, R. Garreaud, C. Grados, D. S. Covert, T. S. Bates, R. Krejci, L. M. Russell, S. de Szoeke, A. Brewer, S. E. Yuter, S. R. Springston, A. Chaigneau, T. Toniazzo, P. Minnis, R. Palikonda, S. J. Abel, W. O. J. Brown, S. Williams, J. Fochesatto, J. Brioude, and K. N. Bower (2011), The VAMOS Ocean-Cloud-Atmosphere-Land Study Regional Experiment (VOCALS-REx): goals, platforms, and field operations, *Atmos. Chem. Phys.*, *11*(2), 627–654, doi:10.5194/acp-11-627-2011.

List of Figures

List of Tables

Nomenclature

Greek Letters

α_C	water accomodation
α_T	thermal accomodation
γ	ratio of Aitken to total particle number concentration
η	fraction of activated particles
$\zeta(X_\mathrm{i})$	susceptibility of cloud droplet number concentration towards changes in X_i
η_air	viscosity of air
κ	hygroscopicity parameter
λ	wavelength
ρ_w	density of water
$\sigma_\mathrm{s/a}$	the surface tension of the solution air interface
σ_acc	standard deviation of accumulation mode
σ_Aitken	standard deviation of Aitken mode
θ	potential temperature
θ_l	liquid potential temperature

Roman Letters

A	$A = 8.69251 \,\mathrm{x}\, 10^{-6}\,\mathrm{K\,m^3\,J^{-1}}$
a	absolute humidity
a_K	$a_\mathrm{K} = 2\sigma/(\rho_\mathrm{L} R_\mathrm{v} T)$
$\mathrm{ACI_N}$	aerosol-cloud interaction metric
b_R	$b_\mathrm{R} = 3 i m_\mathrm{v} M/(4\pi\rho_\mathrm{L} m_\mathrm{s})$

$\mathrm{CCF}_{\mathrm{N,\,q_l^*}}(\mathrm{k})$	cross correlation function between N and q_l^*
C_c	slip correction factor
c_p	specific heat capacity of air ($c_\mathrm{p} = 1004\,\mathrm{J\,kg^{-1}\,K^{-1}}$)
D	diffusivity
d	horizontal extend
D^*	modified diffusion coefficient for water vapor in air (D^* given in $\mathrm{m^2\,s^{-1}}$)
D_d	droplet diameter
D_p	particle diameter
dd	wind direction
D_dry	volume equivalent dry diameter
$D_\mathrm{p,\,act}$	activation diameter
$D_\mathrm{p,\,acc}$	mean particle diameter of accumulation mode
$D_\mathrm{p,\,Aitken}$	mean particle diameter of Aitken mode
d_T	thermal jump length
d_v	vapor jump length
E	electric field intensity
e	elementary unit of charge
$e_\mathrm{s,\,w}(T)$	saturation water vapor pressure
f	frequency
K	conductivity
K^*	modified thermal conductivity of air (K^* given in $\mathrm{W\,m^{-1}\,K^{-1}}$)
L_v	latent heat of condensation ($L_\mathrm{v} = 2.5 \cdot 10^6\,\mathrm{J\,kg^{-1}}$)
m	droplet mass
M_w	molecular weight of water
N	total particle number concentration
N_act	number concentration of activated particles
N_Ait	number concentration of Aitken mode particles

N_{CCN}	CCN concentration
N_{d}	cloud droplet number concentration
$\overline{N}_{\mathrm{tot}}$	running median of the outside cloud number concentration
n	number of charges
p	air pressure
p_0	reference air pressure
q	specific humidity
q_{l}	liquid water content
q_{v}	specific humidity, water vapor mixing ratio
R	universal gas constant
r	particle radius
R_{v}	gas constant of water vapor ($R_{\mathrm{v}} = 461.5\,\mathrm{J\,kg^{-1}\,K^{-1}}$)
R_{dry}	gas constant of dry air ($R_{\mathrm{dry}} = 281\,\mathrm{J\,kg^{-1}\,K^{-1}}$)
rH	relative humidity
S	supersaturation
S_{crit}	critical supersaturation
s_{eq}	equilibrium supersaturation ratio at the particle/air interface
s_{∞}	saturation ratio of the surrounding air
T	temperature
t	simulation time
T_{d}	dewpoint temperature
T_{s}	sonic
u	wind component in x-direction
UU	horizontal wind speed
v	wind component in y-direction
V_{elec}	electric drift velocity
w	vertical wind velocity

z_{baro}	barometric height, altitude
Z_{p}	electrical mobility

Abbreviations

ACI	aerosol-cloud interaction metric
ACTOS	Airborne Cloud Turbulence Observation System
asl	above sea level
CARRIBA	Clouds, Aerosols, Radiation and tuRbulence in the trade wInd regime over BArbados
CCF	cross correlation function
CCN	Cloud Condensation Nuclei
CCNc	Cloud Condensation Nucleus Counter
CDNC	cloud droplet number concentration
CISL	Computational & Information Systems Laboratory
CL	cloud layer
CPC	Condensational Particle Counter
DMA	Differential Mobility Analyser
DMPS	Differential Mobility Particle Sizer
ITCZ	Intertropical Convergence Zone
ITCZ	Intertropical Convergence Zone
LT	local time
LWC	liquid water content
mCCNc	mini Cloud Condensation Nucleus counter
MPI-M	Max Planck Institute for Meteorology
NCAR	National Center for Atmospheric Research
NCEP FNL	National Centers for Environmental Prediction final analysis
NSD	number size distribution
OPC	Optical Particle Counter
PBL	planetary boundary layer

pdf	probability density function
PDI	phase Doppler interferometer
PICT	Phase Doppler Interferometer for Cloud Turbulence
PVM	Particle Volume Monitor
SAFIRE	Service des Avions Franais Instruments pour la Recherche en Environnement - French office of aircraft instrumented for environmental research
SCL	sub cloud layer
SMART-HELIOS	Spectral Modular Airborne Radiation measurement sysTem for HELIcopter-borne ObservationS
SMPS	Scanning Mobility Particle Sizer
stp	standard temperature and pressure
TAS	true air speed
TROPOS	Leibniz Institute for Tropospheric Research
UFT	Ultra Fast Thermometer
USA	Ultra Sonic Anemometer
UTC	coordinated universal time

Acknowledgments

At this point, I would like to thank all people, who helped me finishing this dissertation. First and most of all, I would like to thank Birgit Wehner and Holger Siebert, who gave me the opportunity to participate in 4 measurement campaigns with the unique measurement platform ACTOS at remarkable places such as Barbados. Birgit and Holger have always been patient supervisors and encouraged and enabled me to carry out more than 10 research flights on my own responsibility. I further thank Prof. Dr. Alfred Wiedensohler and Prof. Dr. Alfons Schwarzenböck for reviewing this dissertation.
Since this work was funded by the Deutsche Forschungsgemeinschaft (DFG), I would like to thank Holger Siebert, Birgit Wehner, Heike Wex and Manfred Wendisch for writing the successful proposal. I further thank all members of my expanded supervisors committee: Birgit Wehner, Martin Simmel, Albert Ansmann, Heike Wex and Alfred Wiedensohler for their scientific guidance and support during the compilation of this manuscript.
Martin Simmel introduced me into his cloud microphysical parcel model, and, therefore provided a basis to gain some very interesting insights in the complex field of cloud microphysics. Also Raymond Shaw, Tina Schmeißner and Frank Werner contributed to some very fruitful discussions on aerosol-cloud interactions.
I would like to thank Heike Wex and Thomas Müller for providing CCN data and the support with the processing of the OPC data, respectively. I thank Ilya Serikov for providing lidar data and I particularly thank Thomas Kanitz and Anja Schwarz for their help to interpret the lidar and FLEXPART data and their proof-reading of the corresponding chapter.
Measurement campaigns with ACTOS are always an exciting experience and bond people together. I thank all members of the ACTOS team which I have not mentioned yet and I thank particularly Thomas Conrath, Dieter Schell and Christoph Klaus for their great support at any time during all measurement campaigns. I would also like to thank Alwin Vollmer, Milos Kapetanovic and Jürgen Schütz for their outstanding performance and all the safe helicopter flights.
Every field campaign is connected with intense laboratory work. Many thanks to Maik Merkel and Anja Schmidt for their support during any laboratory work and additional thanks to the mechanical and electrical workshops at TROPOS for their fast and straightforward help.
I thank the Blaswerk Leipzig e.V. for the necessary distraction, and Manuel Duraô, who almost began to study meteorology, for showing me fascinating analogies between music and science.
Last but not least I would like to thank my family for their absolute support and keeping me grounded. I particularly thank Jeannine Katzwinkel for enlightening discussions, her patience and encouragement, and her love.